POLISH ACADEMY OF SCIENCES

Opto-Electronics Review

journal homepage: http://journals.pan.pl/opelre

2D material infrared and terahertz detectors: status and outlook

A. Rogalski, M. Kopytko*, P. Martyniuk

Institute of Applied Physics, Military University of Technology, 2 Kaliskiego St., 00-908 Warsaw, Poland

Article info

Article history:
Received 05 May 2020
Received in revised form 16 Jun. 2020
Accepted 08 Jul. 2020

Keywords:
2D material photodetectors, terahertz detectors, infrared detectors, graphene, BLIP performance, HgCdTe photodiodes

Abstract

Graphene applications in electronic and optoelectronic devices have been thoroughly and intensively studied since graphene discovery. Thanks to the exceptional electronic and optical properties of graphene and other two-dimensional (2D) materials, they can become promising candidates for infrared and terahertz photodetectors.

Quantity of the published papers devoted to 2D materials as sensors is huge. However, authors of these papers address them mainly to researches involved in investigations of 2D materials. In the present paper this topic is treated comprehensively with including both theoretical estimations and many experimental data.

At the beginning fundamental properties and performance of graphene-based, as well as alternative 2D materials have been shortly described. Next, the position of 2D material detectors is considered in confrontation with the present stage of infrared and terahertz detectors offered on global market. A new benchmark, so-called "Law 19", used for prediction of background limited HgCdTe photodiodes operated at near room temperature, is introduced. This law is next treated as the reference for alternative 2D material technologies. The performance comparison concerns the detector responsivity, detectivity and response time. Place of 2D material-based detectors in the near future in a wide infrared detector family is predicted in the final conclusions.

Contents

1. Introduction
2. Relevant properties of graphene and related 2D materials
   2.1. Relevant graphene properties
   2.2. Properties of 2D crystalline materials
      2.2.1. Transition metal dichalcogenides
      2.2.2. Black phosphorus
3. Graphene-based detectors
   3.1. Types of detectors
      3.1.1. Photoconductors
      3.1.2. Photogating effect
      3.1.3. Photovoltaic detectors
      3.1.4. Photo-thermoelectric detectors
      3.1.5. Bolometers
      3.1.6. Field effect transistor detectors
   3.2. Responsivity-enhanced graphene-based detectors
   3.3. Graphene-based thermal detectors
   3.4. Graphene-based terahertz detectors
   3.5. Graphene-based detector performance - the present status
4. Related 2D material detectors
   4.1. General overview
   4.2. Middle and long wavelength infrared detectors
      4.2.1. Black phosphorus photodetectors
      4.2.2. Noble transition metal dichalcogenide photodetectors
   4.3. Terahertz detectors
   4.4. 2D material detector performance - the present status
5. Conclusions

*Corresponding author: malgorzata.kopytko@wat.edu.pl

https://doi.org/10.24425/opelre.2020.134459
1896-3757/© 2020 Association of Polish Electrical Engineers (SEP) and Polish Academic of Sciences (PAS). Published by PAS.

1. Introduction

HgCdTe takes the dominant position in the infrared (IR) detector technology. This material has inspired the development of the four "generations" of detector devices considered for military and civilian applications which are briefly described in the caption of Fig. 1 [1]. IR detector technology combined with a fabrication of epitaxial heterostructure [by molecular beam epitaxy (MBE) and metalorganic chemical vapour deposition (MOCVD)] and photolithographic processes revolutionized the semiconductor industry, thus, enabling the design and fabrication of complex focal plane arrays (FPAs). Further their development will be connected with the implementation of the fourth generation staring systems of which the main features are: high resolution (with a very large number of pixels - above 10^8), multi-colour functionality, three dimensional readout integration circuits (3D ROIC), and other integration functions such as polarization/phase sensitivity, better radiation/pixel coupling or avalanche multiplication. The first three generations of imaging systems primarily rely on planar FPAs. Several methods to overcome this limitation including bonding detectors to flexible or curved monolithic imaging detectors have been proposed [2]. Evolution of the fourth generation is inspired by the most famous visual systems which are the biological eyes. Solution based on the Petzval-matched curvature allows the reduction of a field curvature aberration. In addition, it combines such advantages as simplified lens system, electronic eye systems and wide field-of-view [3,4]. The colloidal quantum dot (CQD) [5] and two-dimensional (2D) layered material [6] photodetectors fabricated on flexible substrates are promising materials to overcome technical challenges in the development of the fourth generation IR systems.

Before 2D materials become the final benchmark for standard electronic materials and devices, decades of research, development and, most importantly, billions of dollars of investment must be made. Then, the high quality of these materials will provide a promising alternative for the next-generation sensor platform. On the other side, the evolutionary path of Si technology, driven by Moore's Law of Scaling, seems to be narrowing and fast approaching the end, simply due to the fundamental limitations of Si at the atomic scale [7]. In fact, it is unlikely that the 2D technology will supplant Si; but instead may coexist with the Si technology [8]. However, this will require an increased research and investment for the research in the area of the 2D material growth at temperatures compatible with the Si-based technology. All mentioned aspects are still in the early stages of development.

Independently from the above shortcomings, it is interesting to estimate the place of 2D material detectors in the IR detector family. The first paper which has undertaken this issue was published in the last year [1]. Here, in the paper this topic is treated comprehensively including both theoretical estimations and many experimental data. As there are many comprehensive papers focusing on 2D material synthesis, this field will not be reviewed here.

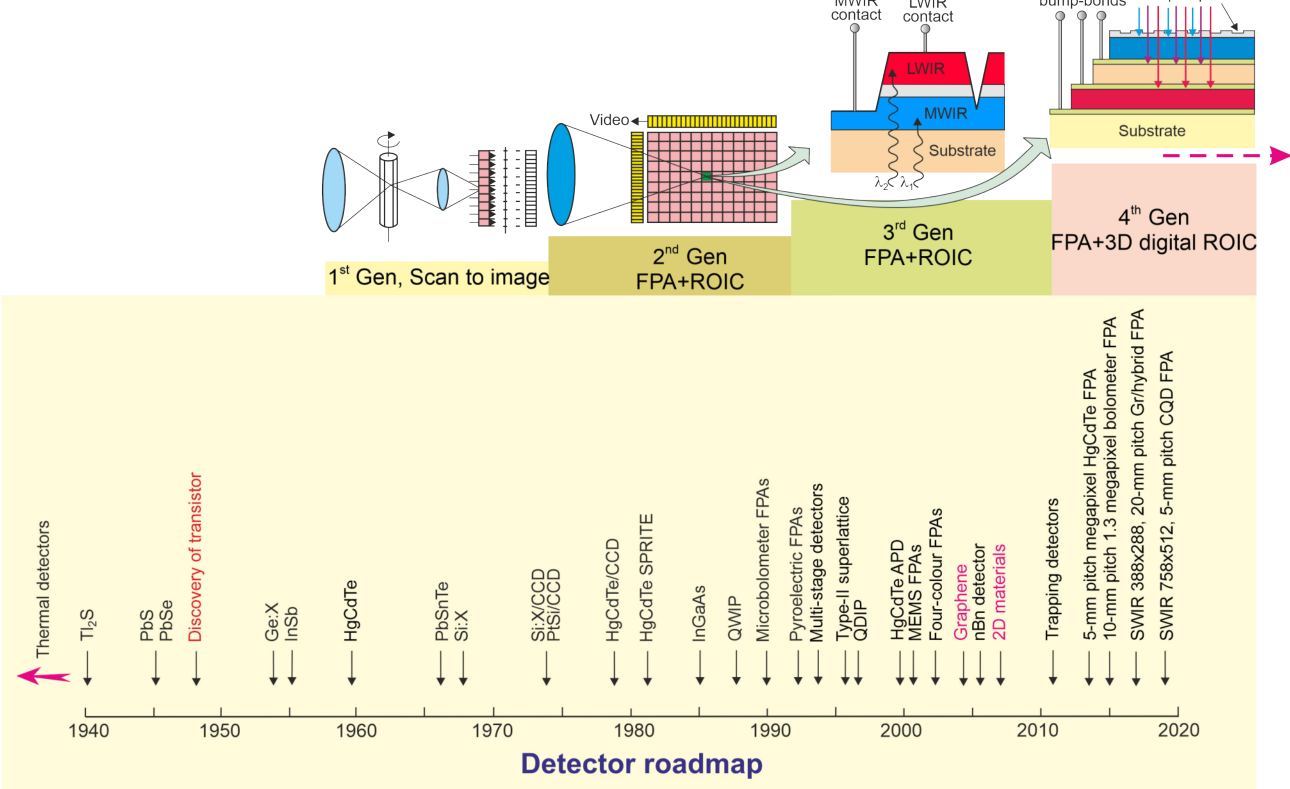

Fig. 1. Development of IR detectors and systems history. For principal military and civilian applications four generation systems can be considered: first generation (scanning systems), second generation (staring systems - electronically scanned), third generation (staring systems with a large number of pixels and two-colour functionality), and fourth generation (staring systems with a very large number of pixels, multi-colour functionality, 3D ROIC, and other on-chip functions; e.g., better radiation/pixel coupling, avalanche multiplication in pixels, polarization/phase sensitivity) [adapted after Ref. 1].

2. Relevant properties of graphene and related 2D materials

The discovery of graphene and other 2D materials has triggered interest in a development of the next generation of optoelectronic devices which creates a new platform for a variety of photonic applications [9,10], including fast photodetectors [11,12], transparent electrodes in displays and photovoltaic modules [13,14], optical modulators [15], plasmonic devices [16], and ultrafast lasers [17].

2D materials are atomically thin films originally derived from layered crystals such as graphite, hexagonal boron nitride (h-BN), family of transition metal dichalcogenides (TMDs), such as molybdenum disulfide (MoS_2), tungsten disulfide (WS_2) and molybdenum diselenide ($MoSe_2$), molybdenum ditelluride ($MoTe_2$), and others, and black phosphorus (bP) [18]. Among the extraordinary physical and chemical properties of these materials, the most important are:

- quantum constraint towards the 2D plane which is beneficial for light absorption,
- weak stack of atomic planes on each other by van der Waals (vdW) forces leaves no dangling bonds which makes it easy to construct vertical heterostructures and integrate 2D materials with silicon chips,
- atomically thin dimensions enable the production of nanodevices deprived of the parasitic capacitance.

2D materials are based on many compounds in the periodic table which have properties allowing to cover a wide range of the electromagnetic spectrum, from ultraviolet (UV), through visible, infrared, up to terahertz (THz) range. As shown in Fig. 2 [18,19], having a wide energy gap h-BN is used only as a topologically smooth insulator, TMD and bP are applicable in mid/ small-bandgap optoelectronics while graphene is a zero bandgap material. The significant 2D materials used for fabricating opto-electronic devices and a few of their electronic properties are listed in Table 1.

2.1. Relevant graphene properties

Graphene has been extensively and comprehensively studied since 2004 due to its unique and exceptional electronic and optical properties [20-22]. The linear dispersion relation between energy and the wave vector in a graphene band structure, which is accompanied by the electron transport at a Fermi speed only 100 times lower than the speed of light, is the most intriguing electronic property of this material. Another interesting feature for graphene, especially in terms of its use in optoelectronic devices, is its high thermal conductivity

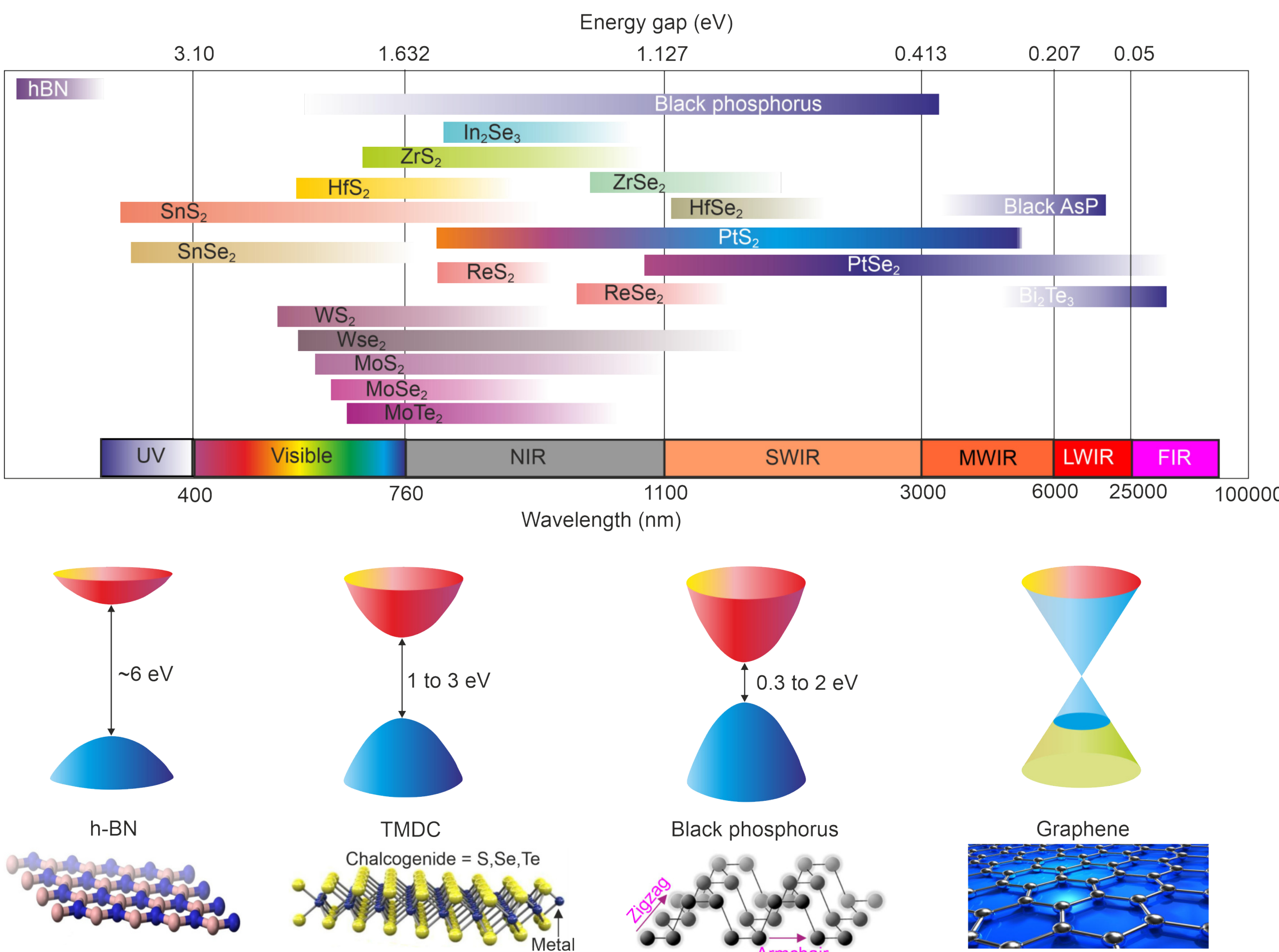

Fig. 2. Bandgap of different layered semiconductors and electromagnetic spectrum. The exact bandgap value depends on the number of layers, strain level and chemical doping. FIR: far infrared; LWIR: long wavelength infrared; MWIR: mid wavelength infrared; SWIR: short wavelength infrared; NIR: near infrared; UV: ultraviolet. The atomic structures of hexagonal born nitride (h-BN), TMDs, black phosphorus (bP), and graphene are shown in the bottom of the panel, left to right. The crystalline directions (*x* and *y*) of anisotropic bP are indicated [adapted after Refs. 18 and 19].

Table 1
Room temperature properties of selected 2D materials [after Ref. 9]

2D material	Band gap (eV)	Effective mass (m_o)	Device mobility (cm^2/Vs)	Saturation velocity (m/s)	Young's mod. (GPa)	Thermal conductivity (W/mK)	CTE* (10^6 K^{-1})
Graphene	0 (D)	< 0.01	10^3–5×10^4	$(1\text{-}5)\times10^5$	1000	600–5000	−8
1L MoS_2	1.8 (D)	~0.5	10–130	4×10^4	270	40	NA
Bulk MoS_2	1.2 (I)		30–500	3×10^4	240	50(‖), 4(⊥)	1.9(‖)
1L WSe_2	1.7 (D)	0.31	140–250	4×10^4	195	NA	NA
Bulk WSe_2	1.2 (I)		500	NA	75–100	9.7(‖), 2(⊥)	11(‖)
h-BN	5.9 (D)		NA	NA	220–880	250–360(‖), 2 (⊥)	−2.7
Phosphorene	0.3–2 (D)	0.17	50–1000	NA	35–164	10–35(‖)	NA

All listed values should be considered estimates. In some cases, experimental or theoretical values are not available (NA).
D, I; direct and indirect energy gap
The ‖ symbol signifies the in-plane direction; ⊥ signifies the out of plane direction.
*CTE, coefficient of thermal expansion

(approx. 10 × copper and 2 × diamond) and high conductivity (approx. 100 × copper). Graphene is also characterized by a high tensile strength (130 GPa, compared to 400 MPa for A36 structural steel).

Hybridized sp^2 carbon atoms [Fig. 3(a)] are arranged in a honeycomb form in a graphene structure with a lattice constant of 1.42 Å. It is obvious that carbon atoms have a total of 6 electrons; 2 in the inner shell and 4 in the outer shell (available for chemical bonding). In graphene, each atom is connected to 3 other carbon atoms on a 2D plane, leaving 1 free electron in the third dimension, which contributes to electrical conductivity. Basically, the electronic properties of graphene are determined by the bonding and anti-bonding of π-orbitals which overlap and enhance the carbon to carbon bonds. These π-electrons are located above and below the graphene sheet and exhibit high mobility.

As shown in Fig. 3(b), graphene is a nearly zero bandgap semiconductor. At the Brillouin zone corners (Dirac points) the valence and conduction bands almost contact with each other. Density of states at Dirac points is almost zero, therefore, the conductivity is reasonably low. By substitutional doping (with electrons or holes) [Fig. 4(b)], the position of the Fermi level (E_F) can be changed and, thus, the electrical properties of graphene can be modified to create a material with a potentially better conductivity at room temperature than copper. However, doping the graphene layer moves the E_F either up or down, reducing the mobility of electrons and holes. The graphene gap band structure can also be modified by addition of two layers [Fig. 4(c)] and bilayer doping [Fig. 4(d)]. In addition, the band gap can be opened by patterning the graphene into the shape of a nanoribbon or by applying a perpendicular electric field to a two-layer graphene. Taking all this into account, the energy gap of graphene can vary from 0 eV to 0.2 eV. The thickness of graphene limitation causes a high resistance and chemical inertness which makes the use of pure conduction less feasible.

The high graphene carrier mobility and saturation velocity show the potential for high speed photonic devices [23]. Theoretically, graphene exhibits a room temperature electron mobility of 250000 cm^2/Vs. Nevertheless, the local environment and material processing strongly influence the transport mechanisms (see Fig. 5). Vacuum suspended graphene fabricated by exfoliation exhibits extremely high carrier mobilities, above 200000 cm^2/Vs at

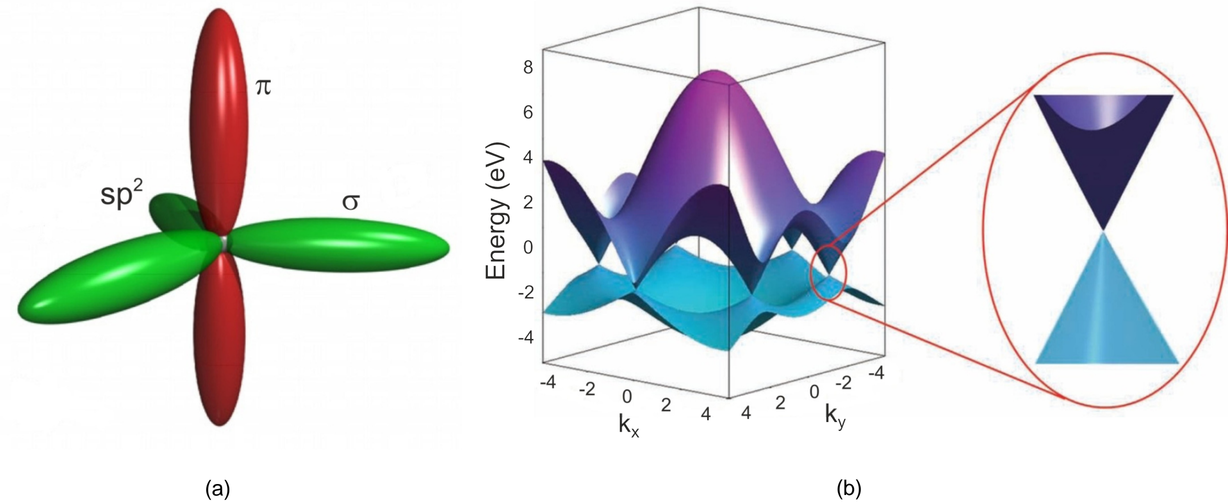

Fig. 3. Schematic of electron σ- and π-orbitals of one carbon atom in graphene: (a) band structure of graphene in the honeycomb lattice (b), the enlarged picture shows the energy bands close to one of the Dirac points [adapted after Ref. 18].

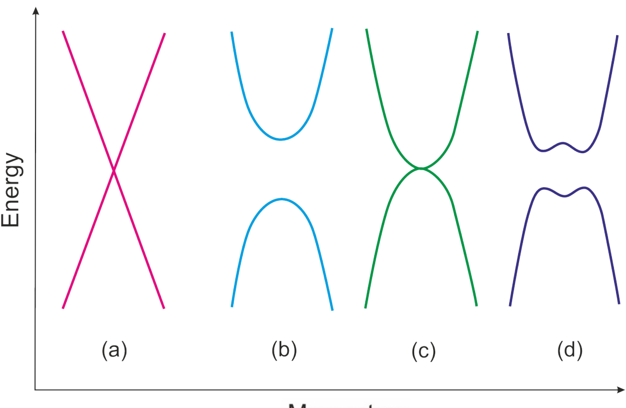

Fig. 4. Modification of a graphene bandgap structure: the Dirac Fermi cone (a), substitutional doping (b), bilayer graphene (c), and doped bilayers (d) [adapted after Ref. 18].

room temperature. Unfortunately, due to the fact that these films have a very small area (about 100 μm^2), this makes it expensive for industrial applications. Graphene placed on a substrate is characterized by a reduced mobility due to both charged impurity and remote interfacial phonon scattering effects. The interfacial phonon scattering also limits the mobility of graphene suspended on SiO_2 to 40000 cm^2/Vs [24]. Moreover, the exposure to atmospheric conditions and processing contaminants (resist residue, water, and metallic impurities) which act as scattering sources reduce the graphene mobility.

What is more, graphene shows the potential for a ballistic carrier transport with a long mean free path > 2 μm at room temperature. Carriers are rather to propagate via diffraction similarly to the light in a waveguide, than by diffusion in comparison to conventional semiconductors.

Compared to metals which are characterized by a large number of free charge carriers, graphene should be considered as a semimetal with an easily achievable concentration of carriers, to its 2D nature, from 10^{12} to 10^{13} cm^{-2} (carriers can be induced by chemical doping or electric gating). This enables graphene electrical tunability which is not possible with conventional metals.

In addition, graphene optical properties are interesting [25] where graphene optical conductivity is defined as: $\pi\beta$, where β is equal to $(1/4\pi\varepsilon_0)(q^2/\hbar c)$, q is the electron charge, $\hbar$ is the reduced Planck constant, c is the light velocity.
The absorption spectrum of graphene covers an ultra-broadband range from the visible to THz spectral range [10]. There are two photo-excitation modes: interband transition and intraband transition. A typical absorption spectrum of a doped graphene [26] is presented in Fig. 6. For the visible and near infrared (NIR) light, electrons can be excited from the valence band to the conduction band through an interband transition with a linear absorption of 2.3% per one 0.33 nm monolayer. This gives the highest specific interaction strength among known materials. The absorption per atom of material is 10–1000 × higher than for semiconductors like silicon or GaAs. At a typical absorption depth of a 10 μm, 2.3% light can be absorbed in a 200 nm silicon layer.

In the low frequency THz region, the photon energy is below $2E_F$ and the interband transition is forbidden while the intraband transition dominates. The optical absorption in graphene is mainly a result of the free-carrier response

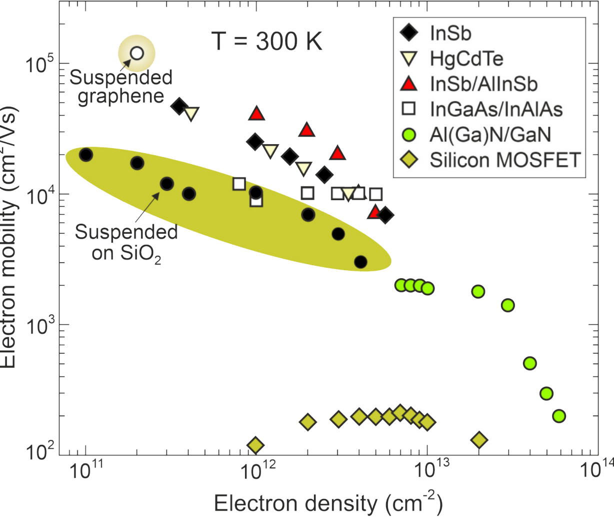

Fig. 5. Electron mobility in graphene at room temperature in comparison with other material systems.

(Drude response). The minimal optical absorption is observed in the mid-wave infrared (MWIR) region. A transition from a universal 2.3% absorption occurs close to $2E_F$. The residual absorption in a MWIR region is generally attributed to the disorder in imparting the momentum for the optical transition.

2.2. *Properties of 2D crystalline materials*

The gapless nature of graphene causes a high dark current which significantly reduces the sensitivity of photodetection and limits the further development of graphene-based photodetectors. A new insight for the production of photodetectors has resulted in the discovery of new 2D materials with direct energy gaps tunable from the visible spectral range to IR. 2D material technology is being developed in various research laboratories around the world, despite the fact that the manufacture and repeatability of devices still remain

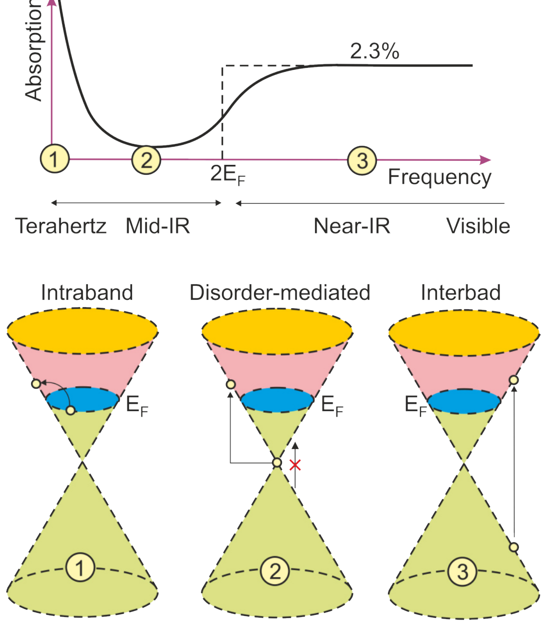

Fig. 6. Characteristic absorption spectrum of doped graphene [adapted after Ref. 26].

a challenge. Researchers interest includes materials such as silicene, germanene, stanene, and phosphorene, TMDs, bP, and recently discovered all inorganic perovskites.

2D materials have their roots in layered vdW solids. Atomic layers are formed in such a way that in-plane atoms are led together by ionic or tight covalent bonds along 2D directions. Each atomic layer is bonded with each other by weak vdW interactions along out-of-plane direction. Such design causes that many of 2D materials could be mechanically exfoliated from bulk single crystals. What is more, due to week physical bonds between each layer, combining different 2D materials together is also possible with the possibility of a free form of heterostructures.

Nicolosi *et al.* [27] summarized different types of layered materials which can be grouped into diverse families (see Fig. 2) that can be covering a broad range of electrical and optical properties:

- atomically thin hexagonal boron nitride (h-BN, similar to hexagonal sheets of graphene),
- transition metal dichalcogenides (TMDs),
- black phosphorus (bP), metal halides (e.g., PbI_2, $MgBr_2$), metal oxides (such as MnO_2 and MnO_3), double hydroxides, III-Vs (such as InSe and GaS), V-VIs (such as Bi_2Te_3 and Sb_2Se_3, and
- halide perovskites.

In this section, is presented a short description of physical properties of 2D materials offering promising potential for use in the next generation infrared and terahertz detectors. A comparison between the bandgaps of 2D materials is shown in Fig. 7, along with those of conventional bulk semiconductors.

2.2.1. Transition metal dichalcogenides

Layered TMDs are atomically thin materials with the chemical formula of MX_2, in which M is the transition metal atom (e.g., Hf, Nb, Mo, Re, Ni, Pd) and X is the chalcogen atom (e.g., S, Se, or Te) [28]. One layer of M atoms is sandwiched by two layers of X atoms (see bottom drownings of Fig. 2). 2D TMDs exist in three polytypes (trigonal - 1T, hexagonal - 2H, and rhombohedral - 3R) which are characterized by different electronic properties, spanning from metallic to semiconducting or even superconducting [29]. The trigonal phase has only been reported in a monolayer shape with a trigonal unit cell, while the 2H and 3R phases have two and three layers with hexagonal and rhombohedral unit cells, respectively.

Unlike graphene, where the electronic properties are based on s and p hybridization, the electronic properties of TMDs depend on the d electron count, i.e., filling of the d orbitals of transition metals and their coordination environment. The number of d electrons in a transition metal varies between 0 and 6 for group 4 to group 10, respectively. The completely filled d orbitals, as in the case of 2H-MoS_2 (group 6) and 1T-PtS_2 (group 10), give rise to a semiconducting nature, while partially filled, as in the case of 2H-$NbSe_2$ (group 5) and 1T-ReS_2 (group 7), exhibit metallic conductivity.

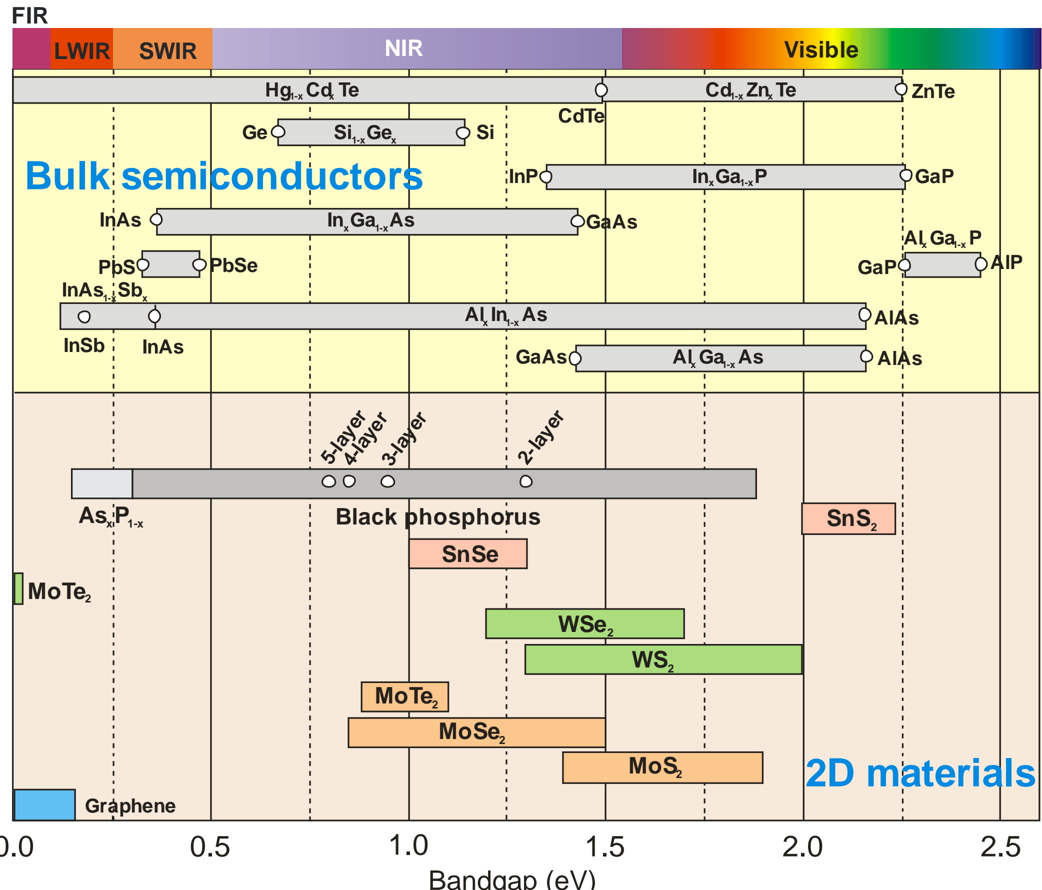

Fig. 7. Spectral range that can be covered by 2D materials and conventional semiconductors with different energy gap values. In 2D materials, the band gap can be tuned over that range by changing the number of layers, straining or alloying. In conventional semiconductors, the band gap can be continuously tuned by changing the alloy composition (e.g., $In_{1-x}Ga_xAs$ or $Hg_{1-x}Cd_xTe$).

Chalcogen atom in turn determines lattice parameters and stability of the material. M-X bonds are covalent; the M atom provides four electrons to fill the bonding states, while the lone-pair of electrons of the X atoms terminate the layers surfaces. The lack of dangling bonds reduces chemical instability and protects the surface against reaction with environmental conditions. Therefore, the more stable the TMDs will be, the more stable the lone-pair of X atoms are. That is why a MoS_2 monolayer is more stable than a $MoTe_2$ monolayer (see Fig. 8) [30]. Stability of materials is an important factor in practical applications affecting reliability and lifetime of a device.

Electro-optical properties of TMDs depend on the number of layers and are significantly different from their bulk crystals properties. The bulk materials based on the same elements as TMDs are indirect semiconductors with a bandgap typically of ~1 eV. When the material becomes thinner from the bulk to the monolayer, the band structure changes from a small indirect to a wide direct one. In consequence, TMDs can detect light at different wavelengths by tuning the bandgap by varying the number of layers due to quantum confinement effects and surface effects [10,12,31-35]. Moreover, optical and electronic properties of these materials can be strongly affected by large strains [36,37].

TMDs carrier mobility increases with the number of layers, in generally, however, their mobility is low (typically less than 250 cm^2/Vs) and this disadvantage is hard to overcome. Similar to graphene, TMDs carrier mobilities are limited by ripples, phonon scattering, impurity scattering and interface scattering [38]. The room-temperature carrier mobility of typical group 6 TMDs with the comparison of different layers of noble TMDs ($PtSe_2$, PtS_2, and $PdSe_2$) and bP on back-gated SiO_2 substrates [39] are summerised in Fig. 9. The charge-carrier density depends on the doping levels and recombination centres, and the typical value is of 10^{12} cm^{-2} [40].

Optical absorption of TMDs in visible to NIR regions is dominated by carrier direct transitions between the valence and conduction band states around K and K' points of the 2D hexagonal Brillouin zone [41] with a contribution of strong excitonic effects. This explains a relatively high

Graphene family	Graphene	Hexagonal boron nitride (h-BN)	Fluorographene	Graphene oxide	
2D layered chalcogenides	Transition metal dichalcogenides (TMDs)				III-VI layered semiconductors
	Semiconducting dichalcogenides		Metallic dichalcogenides		GaS, GaSe Ga_2Se_3, Bi_2Se_3, etc
	MoS_2, WS_2, $MoSe_2$, WSe_2 PtS_2, $PtSe_2$ etc	$MoTe_2$, WTe_2, etc	NbS_2, VSe_2, HfS_2, $HfSe_2$, etc		
2D monoelemental structures	Black phosphorus (bP)	Silicene	Arsenene	Antimonene	Bismuthene
Others	CrI_3	MXenes	Metal oxides	Layered double hydroxides (LDHs)	Perovskites and Niobates

Stable in air	Less stable in air	Unstable in air	Not fully explored

Fig. 8. Summary of stabilities of 2D layered materials (after Ref. 30).

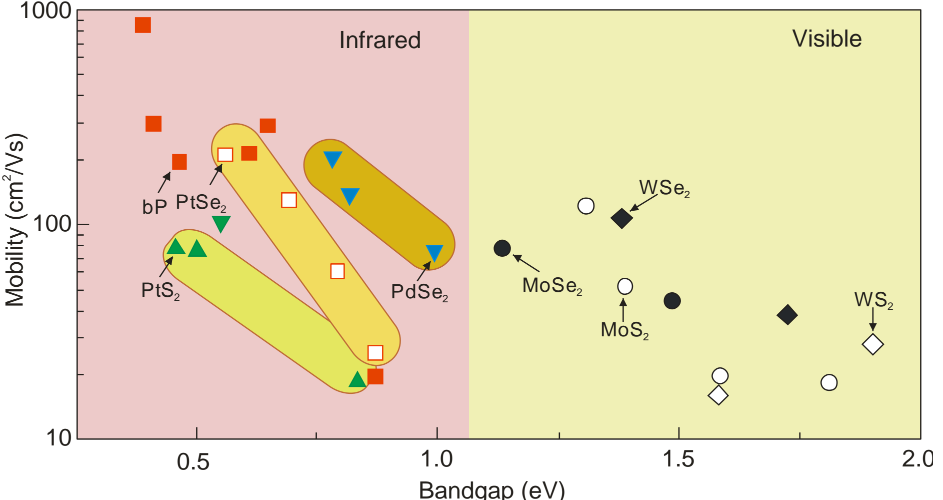

Fig. 9. Layer-dependent room temperature mobility of group-6 TMDs, bP, and typical noble TMDs on back-gated SiO_2 substrate [after Ref. 39].

absorption coefficient of TMDs, on the order of 10^4−10^6 cm^{-1}. As a consequence, more than 95% of the sunlight is absorbed for TMD films with a sub-micro-meter thickness. Compared to graphene, TMDs, like MoS_2, WS_2, and $MoSe_2$ exhibit even higher absorption in the visible and NIR range and cover a very broad portion of the spectrum from IR to UV (see Figs. 2 and 7). Due to the existence of defect or edge states inside the bandgap and a relatively high ratio of the edge-to-surface area, the absorption spectra can be extended to the MWIR region.

For long wavelength infrared (LWIR) detector applications the layered semiconductors with narrow bandgaps and high mobilities are required. Among the TMDs, group-10 noble TMDs provide such opportunity (see Table 2 [42]) which have been re-introduced as new 2D materials displaying widely tuneable bandgap, moderate carrier mobility, anisotropy, and ultrahigh air stability [39]. It has been theoretically predicted that at room temperature the carrier mobility of group X transition-metal dichalcogenides PtX_2 (X = Se, S) is over 1000 cm^2/Vs, and the bandgaps of their bilayers and bulks could be very small between 0-0.25 eV [43,44].

Unlike the most common TMDs with less d-electrons, the orbitals of noble TMDs are nearly fully occupied, and the corresponding p_z orbital of interlayer chalcogen atoms are highly hybridized, leading to strong layer-dependent properties and interlayer interactions [39]. The noble metal atoms hold rich d-electrons and tend to form a d^2sp^3 hybridization, where less d orbitals are involved, leading to the generation of the thermodynamically favoured 1T-phase.

The band structure of MX_2 (M = Ni, Pt, Pd; X = S, Se) is dramatically changed with the layer number shift. Monolayers MS_2 (M = Ni, Pt, Pd) are semiconductors with indirect bandgaps of 0.51, 1.11, and 1.75 eV for NiS_2, PdS_2, and PtS_2, respectively [45]. Furthermore, the bilayer NiS_2 and PdS_2 become metallic as predicted by the first-principles calculation theory. The layer-dependent bandgaps of PtS_2 are verified by the experimental results in Fig. 10(a). Similar to PtS_2, a monolayer $PtSe_2$ is also an indirect bandgap semiconductor. First-principles calculation shows that the bandgap of $PtSe_2$ becomes narrow in a bilayer and turns to zero in a tri-layer which basically implies metallic character [46]. Optical absorption measurements presented in Fig. 10(b) confirm that $PdSe_2$ exhibits a gradual transition from a semiconductor (monolayer) to semimetal (bulk) which is consistent with a theoretical simulation based on the density functional theory. Specifically, when the layer number reaches 50 layers, the bandgap is close to 0.

Despite recent progress, the technology of 2D noble TMDs is still in its infancy, and there are still many challenges for researchers looking for new 2D materials in this wide-open field.

2.2.2. *Black phosphorus*

Discovery of bP, the most stable allotrope of phosphorus, can be dated back a century ago. It was first synthesized from red phosphorus under high temperature and pressure [48]. Studies of bP as a bulk material did not receive much attention from the semiconductor research community up to 2014. At the beginning of 2014, a few research teams reintroduced bP from the perspective of a layered thin film material [49,50].

Table2
Semiconductors among the TMDs with bandgaps below 1 eV [after Ref. 42]

	Mo	W	Ti	Zr	Hf	V	Nb	Ta	Tc	Re	Ni	Pd	Pt
S													
Se													
Te													

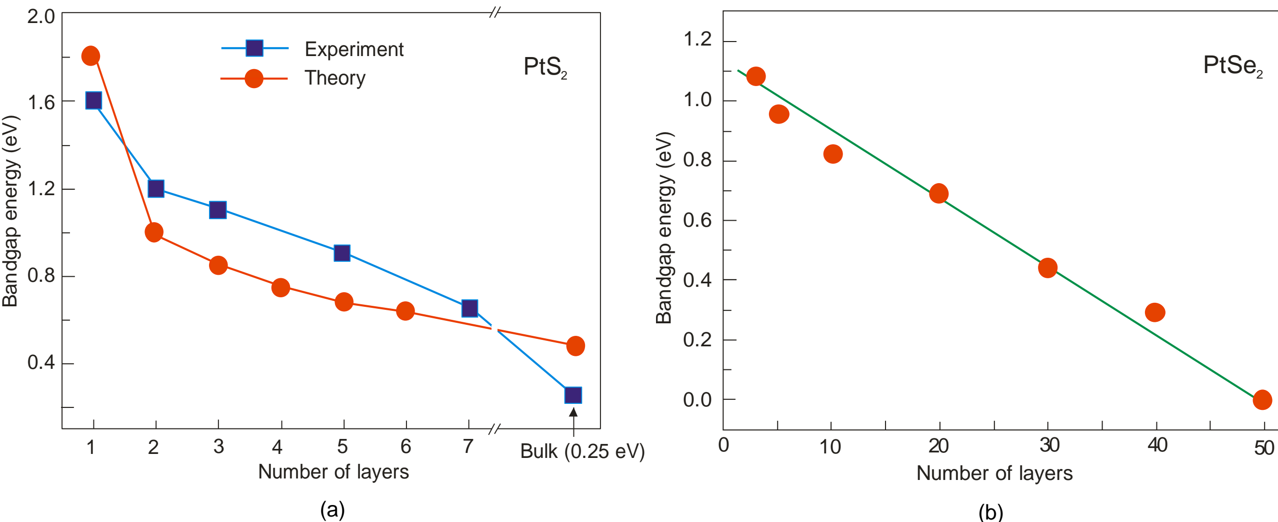

Fig. 10. Layer dependent bandgaps of noble TMDs: (a) PtS_2 [after Ref. 46] and $PtSe_2$ [after Ref. 47].

Bulk bP has an orthorhombic structure with a D_{2h}^{18} space group symmetry. In the atomic layer, each phosphorous atom connects to three neighbouring atoms, leading to two special directions: armchair and zigzag directions along the *x* and *y* axis, respectively [33] (see bottom of Fig. 2). The arrangement of phosphorous atoms is strongly anisotropic what leads to the anisotropic energy band dispersion, further bringing the anisotropic optoelectronic properties. This further causes the anisotropic optoelectronic properties of bP. The effective mass of carriers of bP along the zigzag direction is about 10 times larger than the one along the armchair direction [51] which induces a strong in-plane anisotropy in its electronic, optical, and phonon properties. The strong anisotropic properties can be used to invent new electronic and optoelectronic device applications, such as plasmonic devices with intrinsic anisotropy in their resonance properties and high-efficiency thermoelectric using the orthogonality in the heat and electron transport directions [50].

The strong in-plane anisotropy results in a high hole mobility of 1000 cm^2/Vs along the light effective mass direction and of about 500 cm^2/Vs along the heavy effective mass direction. bP at the same time exhibits a considerable conductivity in samples with thickness from 2 to 5 µm.

Another important feature of bP is its thickness-dependent bandgap which comes from a relatively strong interlayer interaction of buckled bP atomic sheets. The bandgap of bP varies with the number of layers what has been demonstrated both in theory [52] and in experiment [53] as shown in Fig. 11. Obviously, the bandgap of bP increases monotonically as the layer thickness decreases. It should be marked, that bP always keeps its direct-bandgap nature while changing its thickness. It is important to note that the bandgap of bP covers the range of 0.3-1.2 eV.

Beside thickness, the bandgap of bP can also be modulated by other strategies, including applying strain, electric field, and composition alloying. Liu *et al.* [54] have demonstrated fully a composition tunability of black phosphorus-arsenic As_xP_{1-x} (b-AsP) alloys covering a long wavelength region down to around 0.15 eV (corresponding to a wavelength of 8.27 µm, LWIR regime) - see Fig. 12. So, the bandgap of bP (and its compounds) itself covers an extremely wide range of energy of ~0.15-2 eV corresponding to ~ 8-0.6 µm, which has not been achieved in any other 2D layered materials. Thus, b-AsP bridges the gap between graphene (nearly zero bandgap semiconductor) and TMDs (wide bandgap semiconductors).

Also, the transport properties of bP lie between that of graphene and most TMDs previously studied, what is shown in Fig. 13. There are demonstrated carrier mobilities *vs*. current on/off ratio reported for field effect transistors based on typical 2D materials. Here, it should be explained that the on/off ratio is the figure of merit for having high performance and low leakage power for the complementary metal-oxide-semiconductor (CMOS) transistors. Since the channel currents when the transistor is in the conduction mode (I_{on}) should be maximal and the channel currents when the transistor is switched off (I_{off}) should be minimal, the I_{on}/I_{off} should be the highest as possible. Typically, on/off ratio is of around 10^5-10^6.

Despite the possible variations of the mobility at different 2D material classes, they fall into three zones. Graphene with a very high mobility is characterized by the on-off transistor ratio often less than 10, due to its zero bandgap (high dark current). TMDs materials are a predisposition for ultra-low power nanoelectronics. Black phosphorus falls into the region on the plot of mobility/on-off ratio not easy covered by graphene or TMDs. This region, where the mobility is in the range of few hundred cm^2/Vs and at the same time the on/off ratio is roughly of around 10^4, is attractive for gigahertz thin film electronics.

In the context of nanodevices, one of the most important issues is the stability of 2D materials in ambient conditions (see Fig. 8) which significantly limits their practical applications. With the rising research interest in bP, the study on this material chemical stability is the most intensive, owing it to its large reactivity and environmental instability in ambient conditions [55,56]. Exfoliated flakes of bP are highly hydroscopic and tend to uptake moisture from air. The long-term contact with water condensed on the surface degrades the bP. Many researchers have been focused on the methods to improve their air-stability using materials and chemicals like Al_2O_3, TiO_2, HfO_2, titanium sulfonate ligand (TiL4); and coating materials, such as graphene, MoS_2, or h-BN [30].

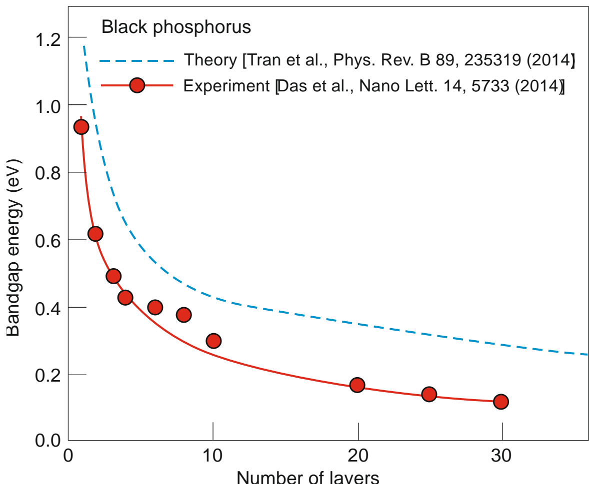

Fig. 11. Thickness dependent band gap of bP, both in theory and in experiment.

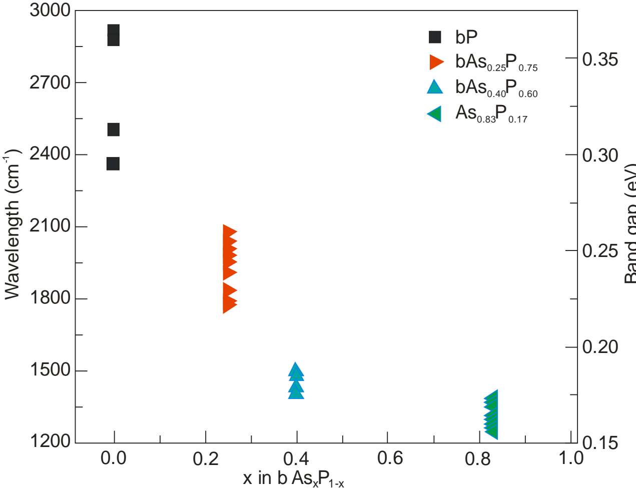

Fig. 12. Bandgaps of b-As_xP_{1-x} with various compositions [after Ref. 54].

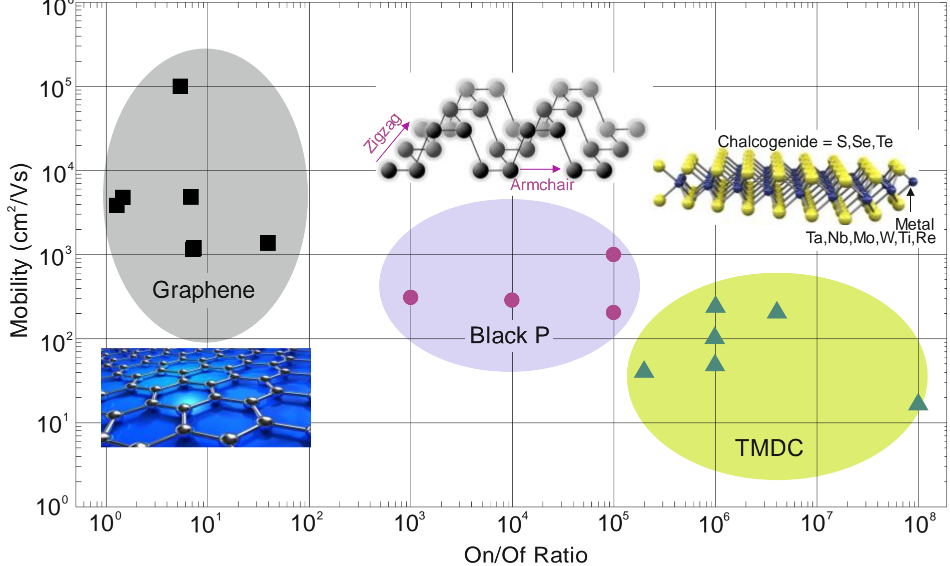

Fig. 13. Carrier mobility *vs.* current on/off ratio reported for typical 2D materials electronics [after Ref. 50].

3. Graphene-based detectors

In this chapter are presented an overview of emerging graphene-based detectors performance and their comparison with traditionally and commercially available ones in different applications in high operating temperature conditions. Generally, 2D material detectors can be divided into two categories: either photon or thermal detectors. One is related to the excitation of free carriers as a result of an optical transition, including photoconductive effect and photovoltaic effect. The other is attributed to the thermal effect including, e.g., bolometric effect and photothermo-electric (PTE) effect.

3.1. Types of detectors

3.1.1. Photoconductors

Schematic operations of two most popular photodetectors are shown in Fig. 14. The photoconductive (PC) detector is essentially a radiation-sensitive resistor with two metal contacts. A photon of energy greater than the bandgap energy is absorbed to produce electron-hole (e-h) pairs, thereby changing material electrical conductivity. The generated e-h pairs are separated by the external electric field, generating a photocurrent [18].

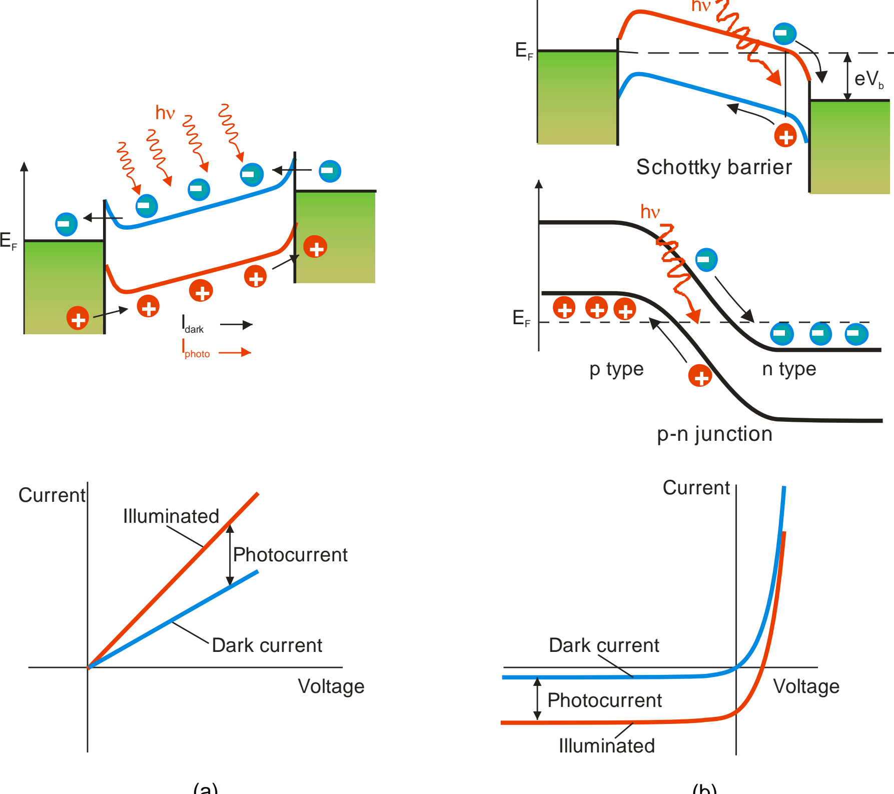

Fig. 14. Schematic of the photoconductive (a) and photovoltaic (b) effects.

Assuming that the signal photon flux density $\Phi_s(\lambda)$ is incident on the detector area $A = wl$ (w - width, l - length),the basic expression describing photoconductivity in semiconductors under equilibrium excitation (i.e., steady state) is as follows [57]:

$$I_{ph} = q\eta A\Phi_s g, \quad (1)$$

where q is the electron charge, I_{ph} is the short circuit photocurrent at zero frequency; that is, the increase in current above the dark current accompanying irradiation. The quantum efficiency, η, can be defined as a number of electron-hole pairs generated per incident photon, and describes how well the detector is coupled to the impinging radiation. The second parameter, the photoconductive gain, g, is determined by the properties of the detector (i.e., by which detection effect is used and the material and configuration of the detector) and can be defined as a number of carriers passing contacts per one generated pair. The value of g describes how well the generated charge carriers are used to generate a photodetector current response.

In general, photoconductivity is a two-carrier phenomenon and the total photocurrent of electrons and holes is as follows [57]:

$$I_{ph} = \frac{qwt(\Delta n\mu_e + \Delta p\mu_e)V_b}{l}, \quad (2)$$

where μ_e is the electron mobility, μ_h is the hole mobility; V_b is the bias voltage, and:

$$n = n_0 + \Delta n; \quad p = p_0 + \Delta p, \quad (3)$$

n_0 and p_0 are the average thermal equilibrium carrier densities, and Δn and Δp are the excess carrier concentrations.

Taking the conductivity to be dominated by electrons (in all known high sensitivity photoconductors this is found to be the case) and assuming a uniform and complete absorption of the light in the detector, it can be shown as the following equation [58]:

$$g = \frac{\tau}{l^2/\mu_e V_b}. \quad (4)$$

So, the photoconductive gain can be defined as:

$$g = \frac{\tau}{t_t}, \quad (5)$$

where t_t is the transit time of electrons between ohmic contacts. This means that the photoconductive gain is given by a ratio of the free carrier lifetime, τ, to the transit time, t_t, between the sample electrodes. Depending upon whether the drift length, $L_d = v_d\tau$, is less than or greater than the distance between electrodes, l, the photoelectrical gain can be less than or greater than unity. The value of $L_d > l$ means that a one charge carrier swept out by one electrode is replaced immediately by an equivalent charge carrier injected by the opposite electrode. In this way, a charge carrier will circulate until it recombines.

Taking into account Eqs. (1) and (4), the photocurrent:

$$I_{ph} = \frac{q\eta A\Phi_s\tau\mu_e V_b}{l^2} \quad (6)$$

is linearly dependent on photon flux density (i.e., excitation power), photogenerated carrier lifetime, electron mobility, and applied bias.

The current responsivity of the photodetector is equal to:

$$R_i = \frac{\lambda\eta}{hc} qg, \quad (7)$$

where λ is the wavelength, h is the Planck constant, and c is the velocity of light.

3.1.2. Photogating effect

The particular example of the photoconductive effect is a photogating. The photogating effect can be realized in two ways by [18]:

- generation of e-h pairs, when one type of carriers is trapped by the localized states (nano-particles and defects), and
- generation of e-h pairs in trap-states and one type of carriers is transferred to 2D materials, whereas the other resides at the same place to modulate the layered materials.

In both cases, due to a long carrier lifetime, the sensitivity enhancement is at the cost of a photoresponse speed.

The photogating effect is explained in Fig. 15. A large photoconductive gain can be obtained if one carrier type (holes or electrons) is trapped in a localized state and the other carrier can circulate through an external circuit many times before the first one recombines. Trapped carrier acts as a local gate, effectively modulating the resistance of active materials. Trap states with long carrier lifetimes (states where carriers can reside for a long time) are usually associated with defects or the surface of the semiconducting material. So, this effect is particularly important for materials where a major role in electrical properties play factors such as a large surface area and a

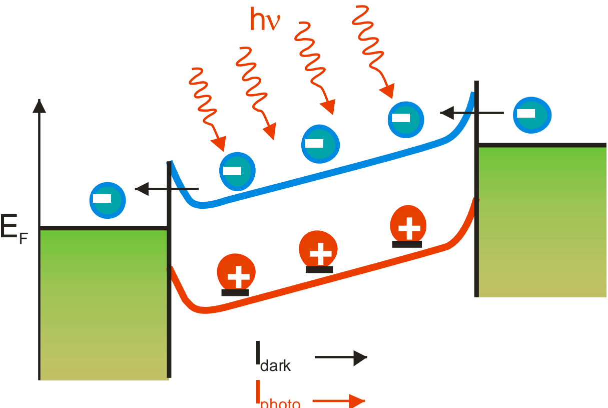

Fig. 15. Band alignment under illumination with a photon of energy higher than the bandgap generating e-h pairs. Holes are trapped at the band edge and act as a local gate. In consequence, the field-effect induces more electrons in the channel, generating a photocurrent which adds to the dark current. If the electron lifetime exceeds time it takes for an electron to transit the device, then the long-time of the trapped holes ensures electrons can circulate through an external circuit many times, resulting in gain.

reduced screening, that is for nanostructured materials, like CQD, nanowires, and 2D semiconductors.

In the case of the photodiode, the photoelectric effect is usually equal to 1, due to a separation of minority carriers by the depletion region electrical field. However, in a hybrid combination of 2D material photodetectors, photosensitization and carrier transport take place in separately optimized regions: one for efficient light absorption, and the second - to provide fast charge reticulation. In this way, ultra-high gain up to 10^8 electrons per photon and exceptional responsivities for short wavelength infrared photodetectors have been demonstrated [59, 60].

A simple architecture of a hybrid phototransistor, very popular in a design of 2D material photodetectors with the fast transfer channel for charge carriers, is shown in Fig. 16. Since, e.g., graphene in these devices is not responsible for light absorption but only for charge sensing, the absorber choice determines the spectral response. The graphene large ambipolar mobility (~10^3 - 10^5 cm^2/Vs) acts as a built-in photogain (i.e., amplifier) mechanism enhancing the detector response.

2D materials with thickness down to atomic layer are more susceptible to local electric fields than conventional bulk materials and the photogating effect can strongly modulate the channel conductivity by the external gate voltage, V_G. Improving the optical gain is particularly important since the quantum efficiency is limited because of the weak absorption in 2D materials. This effect is especially seen in a longer wavelength of IR spectral region, where the light absorption is week. In the case of a hybrid detector shown in Fig. 16(a), holes are injected into the transporting channel, whereas electrons remain in the photoactive layer. The injected charges can reticulate even several thousand times before recombination, giving contribution in gain under illumination. The photocarrier lifetime is enhanced through both bandgap structure and defect engineering, and at the same time, trapping mechanisms limit the response time of a photodetector even to several seconds. There is a trade-off between sensitivity enhancement and photoresponse speed.

Photocurrent change by the photogating effect can be written as [61,62]:

$$I_{ph} = g_m \Delta V_G, \tag{8}$$

where g_m is the transconductance and ΔV_G is the equivalent photoinduced voltage. Figure 16(d) indicates a shift of the $I_{DS}(V_G)$ trace after the light illumination. Generally, both positive and negative photoconductance behaviours are observed in hybrid 2D structures and the working points A and B, related to g_m and ΔV_G, perform opposite directions.

3.1.3. Photovoltaic detectors

Photovoltaic (PV) photocurrent generation is based on the light absorption by a p-n junction made from a semiconducting material. Incident photons with the energy greater than the semiconductor energy bandgap create e-h pairs. The electric field inside the semiconductor, associated with the presence of a p-n junction or a Schottky barrier, separates carriers of different types [top of Fig. 14(b)]. Electrons and holes generated at a distance from the junction shorter than the diffusion length diffusely reach contacts. The generated photocurrent shifts current-voltage characteristics as is shown in the bottom of Fig. 14(b).

Many diodes designed from traditional semiconductors especially as photodiodes are based on a P-i-N junction rather than a p-n junction. Photodiodes are usually operated at zero bias (photovoltaic mode) or under reverse bias (photoconductive mode). The photodiode absolute response is usually smaller than a photodetector working with photoconducting or photogaiting mechanisms, since there is no internal gain. Under a reverse-bias operation, the junction capacity is reduced increasing the response speed. Strong reverse bias can initiate an impact ionization multiplication of carriers or avalanching (avalanche photodiode). The large internal gain results in a detection of an extremely low signal power.

Electrical and optical properties of graphene p-n junctions differ from traditional semiconductor p-n junctions in terms of physical mechanisms involved in a conversion of light into an electrical current. This translates into response speed and device sensitivity.

Graphene is a material in which a p-n junction can easily be obtained because of states limited density. Fermi

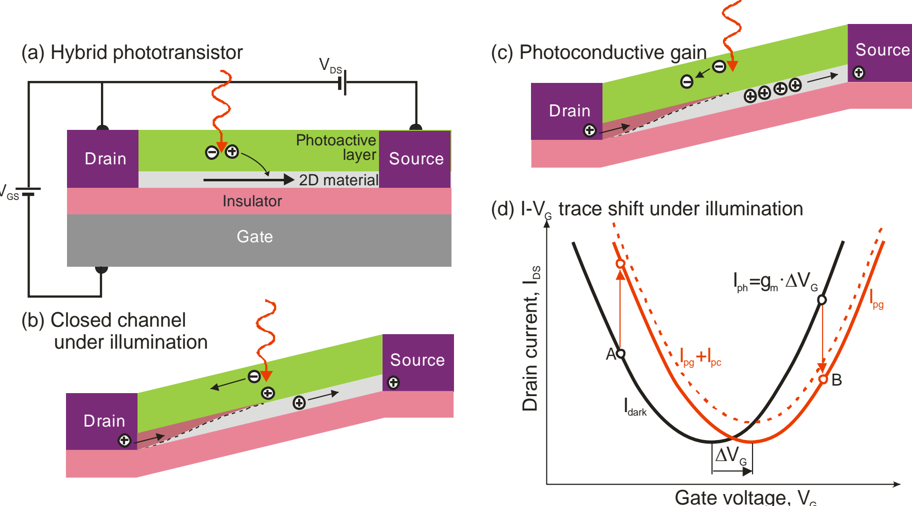

Fig. 16. Photogating effect in 2D material photodetectors: (a) operation of hybrid phototransistor, (b) closed channel under illumination, (c) photoconductive gain, and (d) I-V_G trace under illumination.

level can be tuned by an easy formation of the graphene p-type or n-type doping, as presented in Fig. 17. The built-in electric field can be also introduced by exploiting the work-function difference between graphene and contacts. To obtain a p-type doping, metals with a work function higher than that of intrinsic graphene (4.45 eV) should be used, whereas the graphene channel can be adjusted to p- or n- state by the gate. Electron-electron scattering in graphene can lead to the conversion of one high e-h pair energy into multiple e-h pairs of lower energy potentially enhancing photodetection efficiency [10].

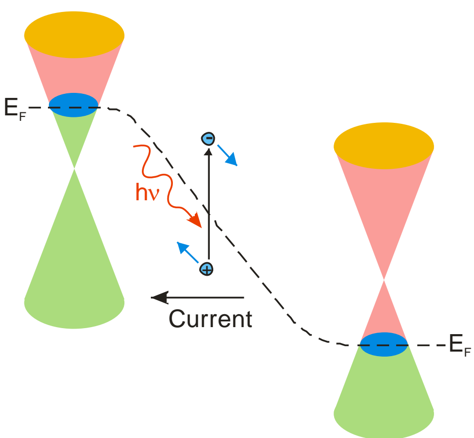

Fig. 17. Schematic of a photo-induced extraction of electron-hole pairs and its separation at a graphene p-n junction.

Photocurrent generation can be also obtained in a graphene phototransistor architecture (Fig. 18) which basically has the same three-terminal configuration as field-effect transistors (FETs). In the operational mode of FETs, the amount of current flowing (the drain current, I_d) in the accumulated channel is controlled by the gate voltage (V_g) magnitude at a given source to the drain bias (V_{ds}). In graphene phototransistors, the channel conductance can be additionally controlled by the light absorption. At zero voltage between the source and drain, a minimal photocurrent is collected when the light spot is focused on the middle of a graphene channel, since there is no built-in electric field in the middle of the channel. When light is incident on the metal graphene interface area, what is attributed to the conventional PV effect, a significant photocurrent is observed. The built-in electric field separates e-h pairs creating a photocurrent in the external circuit. The electric field can be further adjusted by applying a source-drain bias influencing the photocurrent. However, this approach is usually avoided since graphene is a semimetal generating a large dark current.

3.1.4. Photo-thermoelectric detectors

Novel approach employs the photo-thermoelectric (PTE) effect to create an electric field due to a thermal diffusion of electrons to metal contacts. This effect is based on the Seebeck effect where heating is achieved by absorbing light on a thermoelectric material [see Fig. 19(a)]. The light induced temperature gradient can be obtained by a non-uniform light illumination or by a strong difference of the absorption in distinct parts of the device under a global illumination [31].

The internal voltage responsible for a current flow is directly proportional to the temperature gradient difference:

$$\Delta V = \alpha_S \Delta T, \tag{9}$$

where α_S is the Seebeck coefficient commonly expressed in μV/K. The Seebeck coefficient is usually expressed in terms of the conductivity, σ, of the material through the following relation [63]:

$$\alpha_S = \frac{\pi^2 k_B^2 T}{3q}\frac{1}{\sigma}\frac{\partial \sigma}{\partial E}, \tag{10}$$

where k_B is the Boltzmann constant, and the derivative of the electrical conductivity σ with regard to the energy E has to be evaluated at the Fermi energy [$E = E_F = \hbar v_F k_F$] with $\hbar$ the reduced Planck constant, v_F the Fermi velocity (in graphene of about 10^6 m/s), and k_F the Fermi wavevector. In the semiconductor, the sign of the Seebeck coefficient is determined by the majority of charge polarity.

The coefficient α_S is the effective or relative Seebeck coefficient of the device composed of two dissimilar conductors "*a*" and "*b*" by electrically joining one set of their ends. Consequently, a thermovoltage is equal to:

$$\Delta V = (\alpha_a - \alpha_b)\Delta T\ , \tag{11}$$

where α_a and α_b are the absolute Seebeck coefficients of the material *a* and *b*. In the example shown in Fig. 19(a) with two junctions between contact metal and semiconductor, the voltage difference across them is as follows:

$$\Delta V_{PTE} = (\alpha_{Ssemiconductor} - \alpha_{Smetal})\Delta T \approx \approx \alpha_{Ssemiconductor}\Delta T \tag{12}$$

(a)

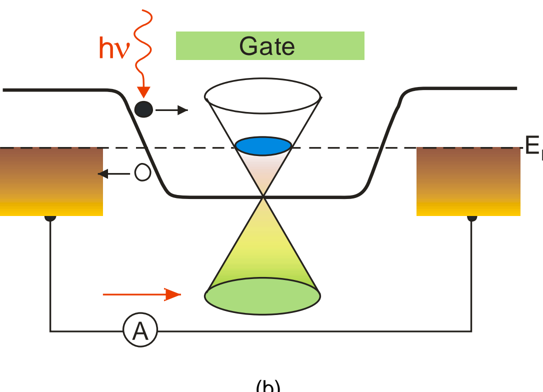

(b)

Fig. 18. Graphene phototransistor: structure of a transistor (a) and a schematic view of photocurrent generation (b).

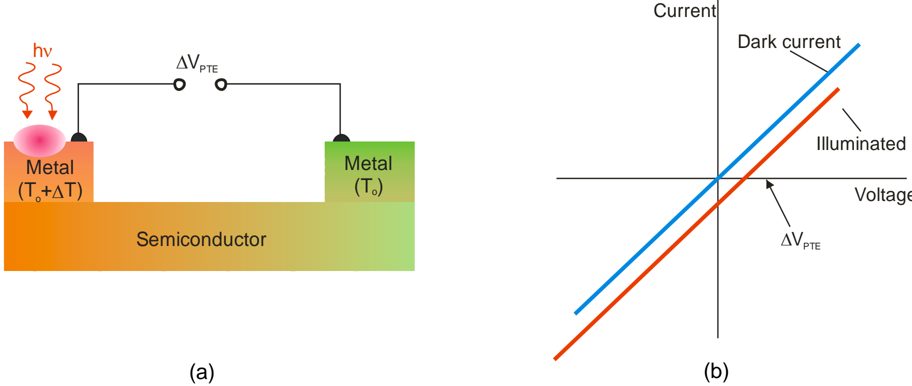

Fig. 19. Photo-thermoelectric effect: in a semiconductor channel (a) and current-voltage characteristics (b).

In the last equation, the term α_{Smetal} is neglected because the Seebeck coefficients of pure metals are in the order 1 µV/K, much smaller than typical values for semiconductors.

The magnitude of ΔV_{PTE} is small and typically ranges from tens of µV to tens of mV (see Fig. 20) [64]. In order to drive current through the device, ohmic contacts to the semiconductors are required. The weak thermal gradient can be achieved in the case of a uniform semiconductor illumination when no current flows in the device since no external bias is applied. It should be noticed that both relative and absolute Seebeck coefficients are temperature dependent and the proportionality between generated potential difference and temperature gradient is valid only within the limit of a small temperature difference.

Typical current-voltage characteristics of a device with a photoresponse dominated by the photo-thermoelectric effect are shown in Fig. 19(b). Linear dependence of *I-V* curve indicates that the Schottky barriers are small (ohmic contacts). PTE effect generates a current at zero bias without changing the resistance.

Differences between PTE effect and bolometric effect should be indicated here. The bolometric one cannot cause any current in the device. Since in this case a homogeneous change in temperature affects the resistivity of a material, only the amount of current will be changed under the influence of external bias and lighting. In the case of a bolometer, the photocurrent sign is associated with a change in the material conductivity with temperature. In a PTE detector, the photocurrent sign is associated with a difference of the Seebeck coefficients between the junction components.

PTE effect also plays an important role in the photocurrent generation in a graphene p-n junction [10,26]. For example, in graphene the optical phonon energy is large (~ 200 meV). Therefore, hot carriers produced by the induced light can remain at a temperature higher than the lattice temperature for many picoseconds (carrier heat capacity is much smaller than lattice heat capacity). This enhances the PTE effect due to a larger temperature gradient in the channel. Thermal equilibrium can only be obtained due to a slower scattering mechanism between charge carriers (although charge carriers a substantially speeded-up due to disorder-assisted collisions) and acoustic phonons (nanosecond range) [18]. The PTE effect on a photocurrent enhancement is shown in Fig. 21. When a light spot illuminates the p-n graphene, the incident radiation modulates the carrier temperature distribution. Due to the temperature gradient, hot carriers (electrons and holes) generated by photons diffuse in respective directions

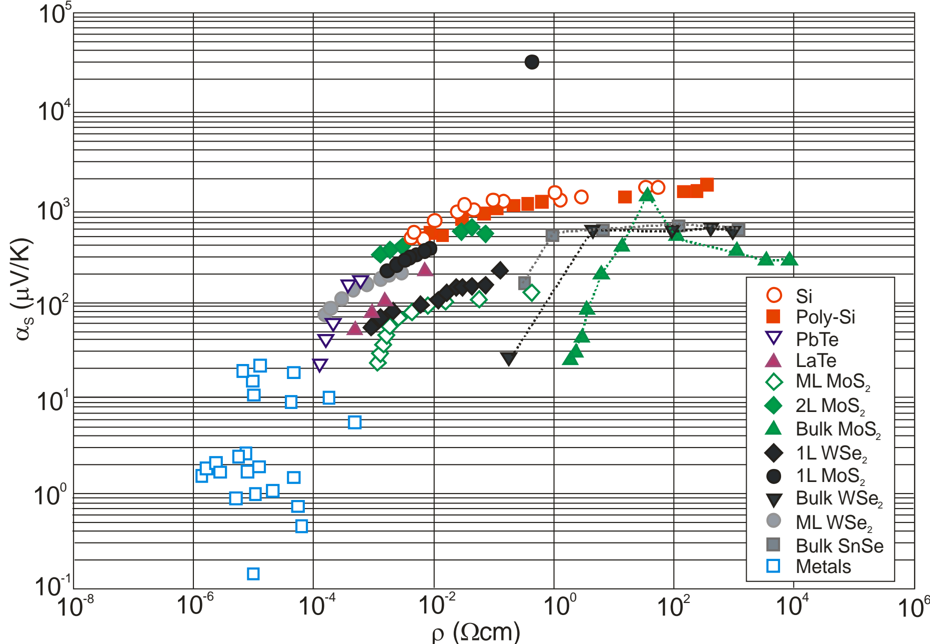

Fig. 20. The Seebeck coefficients as a function of resistivity for various materials [after Ref. 64].

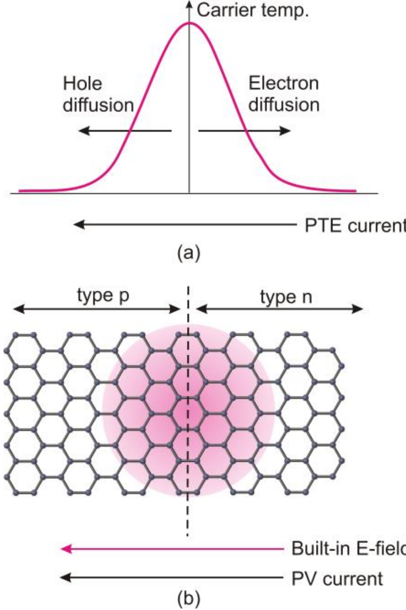

Fig. 21. Photocurrent generation in a graphene p-n junction: profile of carrier concentrations due to light intensity distribution (a), built-in electric field of p-n junction, as well as PTE effect leading to a photovoltaic current flow from n-type to p-type region (b) (adapted after Ref. 26).

leading to a photocurrent flow. The photocurrent direction caused by the PTE effect is the same as that caused by the PV effect, which enhances the photocurrent generation. However, this makes it extremely difficult to experimentally determine the relative contribution of these two effects.

3.1.5. Bolometers

Bolometer key parameters are thermal resistance and heat capacity. The low frequency voltage responsivity, R_v, of the thermal detector ($\omega << 1/\tau_{th}$, where τ_{th} is the thermal response time) is proportional to the thermal resistance, R_{th}, and does not depend on the heat capacitance. At the opposite side, for high frequencies ($\omega >> 1/\tau_{th}$), the voltage responsivity is not dependent on R_{th} and is inversely proportional to the heat capacitance [58]. The thermal conductance (thermal resistance) from the detector to the outside world should be small (high). The smallest possible thermal conductance would occur when the detector is completely isolated from the environment under vacuum with only radiative heat exchange between it and its heat-sink enclosure [1].

It was discovered that graphene assumes low volume for a given area and low density of states resulting in a low heat capacity exhibiting a fast device response. The electrons cooling by acoustic phonons is unproductive (owing to the small Fermi surface) and cooling by optical phonons requires high temperature ($k_BT > 200$ meV) leading to the fact that thermal resistance is relatively high giving rise to bolometric sensitivity [60,65].

Graphene is characterized by over a 100-fold anisotropy of heat flow between in-plane and out-of-plane directions [12]. High in-plane thermal conductivity is due to a covalent sp^2 bonding between carbon atoms, whereas out-of-plane heat flow is limited by a weak vdW coupling. The in-plane thermal conductivity of graphene at room temperature is among the highest of any known material, about 2000-4000 W/mK for freely suspended sampled - see Fig. 22 [66]. The heat flow perpendicular to the graphene sheet is limited with adjacent substrates, e.g., SiO_2. It is interesting, that the thermal resistance between graphene and its environment dominates that between individual graphene sheets. This isolation of graphene was quickly followed by many other materials such as: MoS_2, bP, hBN.

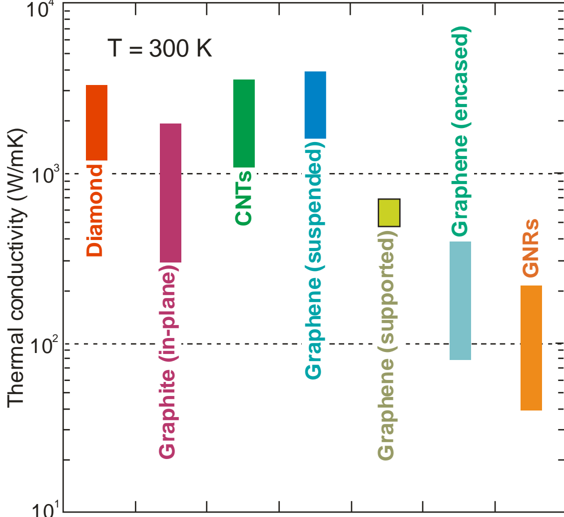

Fig. 22. Room-temperature ranges of thermal conductivity for diamond, graphite, carbon nanotubes (CNTs), graphene, and graphene nanoribbons (GNRs) [after Ref. 66].

There are some technical challenges in a fabrication of 2D material bolometers. In graphene with a weak electron-phonon scattering, resistance is weakly temperature dependent [66]. In consequence, it is challenging to measure the electron temperature change due to incoming radiation power. In addition, to achieve the small electron-phonon thermal conductance, the strong thermal isolation is required what is difficult to obtain. In the case of THz detectors, a low impedance is required to match the antenna to an external readout circuit which is also challenging.

2D materials are naturally great candidates for nanoelectromechanical systems (NEMS) applications. Graphene can sustain large elastic deformations due to it extreme flexibility and could have a positive effect on the device dynamic range.

3.1.6. Field effect transistor detectors

Nonlinear properties of plasma wave excitations (electron density waves) in nanoscale FET channels enable their response at frequencies appreciably higher than the device cut-off frequency which is due to the electron ballistic transport. In the operation ballistic regime, the momentum relaxation time is longer that the electron transit time. FETs can be used both for resonant (tuned to a certain wavelength) and non-resonant (broadband) THz detection and can be directly tuneable by changing the gate voltage [67].

The graphene FET can be also used for a detection of THz radiation what was first proposed by Dyakonov and Shur in 1993 based on a formal analogy between the equations of the electron transport in a gated 2D transistor channel and those describing the shallow water behaviour or acoustic waves in music instruments indicating that hydrodynamic like effect should exist also in the carrier

dynamics in the channel [68]. It must be stressed that instability of that flow in a form of plasma waves was predicted under certain boundary conditions.

The physical mechanism supporting the development of stable oscillations lies in the reflection of plasma waves at the borders of a transistor with a subsequent amplification of the wave amplitude. Plasma excitations in FETs with a sufficiently high electron mobility can be used for emission, as well as detection of THz radiation [69,70].

The plasma waves in FET is characterized by the linear dispersion law [68], and in the gated region:

$$\omega_p = sk = k\left[\frac{q(V_g - V_{th})}{m^*}\right]^{1/2}, \qquad (13)$$

where s is the plasma wave velocity in channel, V_g is the gate voltage, V_{th} is the threshold voltage, k is the wave vector, q is the electron charge, and m^* is the electron effective mass.

The plasma wave velocity in a gated region is typically noticeably larger compared with the electron drift velocity. A short FET channel with the length L_g acts as a resonant cavity for these waves with the eigen frequencies $\omega_n = \omega_o(1+2n)$ $(n = 1, 2, 3,\ldots)$. The fundamental plasma frequency is the following [67]:

$$\omega_o = \frac{\pi}{2L_g}\left[\frac{q(V_g - V_{th})}{m^*}\right]^{1/2}. \qquad (14)$$

When $\omega_o\tau << 1$, where τ is the momentum relaxation time, the detector response is a smooth function of ω and V_g (broadband detector). When $\omega_o\tau >> 1$, FET can operate as a resonant detector with a tuneable by the gate voltage response frequency and this device can operate in the THz range. The detection character (resonant or non-resonant) depends on the quality factor of the transistor resonating cavity.

Assuming $m^* \approx 0.1m_o$ (m_o is the free electron mass), $L_g \approx 100$ nm, and $V_g - V_{th} \approx 1$ V, the frequency of plasma waves is estimated as $\nu_o = \omega_o/2\pi \approx 3$ THz. The minimum gate length can approach ≈ 30 nm, and, thus, ν_o can reach 12-14 THz for FETs with GaAs channels.

Summarizing the above discussion, the non-linear properties of the FET transistor cause the rectification of AC current induced by an incident radiation to the photoresponse which appears as a DC voltage between the source and the drain which is proportional to the radiation intensity (PV effect). In the resonant regime, the plasma waves are dimly damped (when a plasma wave launched at the source can reach the drain in a time shorter than the momentum relaxation time) and the detection mechanism exploits an interference of plasma waves in the cavity, resulting in a resonantly enhanced response [18]. The resonant oscillation of plasma waves in FET gated region is schematically shown in Fig. 23. THz radiation is coupled to the FET transistor by contact pads and connecting wires, even if there is no additional antenna in the system. By adding the appropriate antenna or a cavity coupling, asensitivity improvement can be reached. Broadband detection occurs when plasma waves are overdamped (meaning when plasma waves launched at the source decay before reaching the drain) [18].

Similar to the graphene p-n junction, the PTE effect also shows contribution to the generation of photovoltage in the graphene FET transistor. Two competitive independent detection effects: the plasmonic detection due to the nonlinearity of electron transport and the PTE effect due to the presence of both carrier density junctions, a as well as an induced temperature gradient across the FET channel are presented and schematically explained in Fig. 24. The red region indicates the locally heated area at the interface of ungated and gated sections with the thermopower S_{ug} and S_g, respectively. Even though strongly counterbalanced by the thermoelectric response, the plasma wave detection is a dominant mechanism [18].

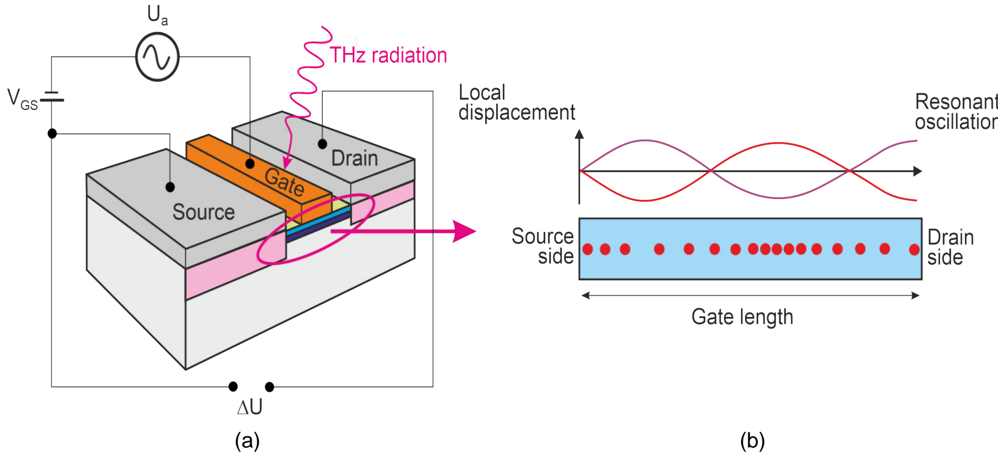

Fig. 23. THz CMOS detector (a) and plasma oscillations in a transistor (b).

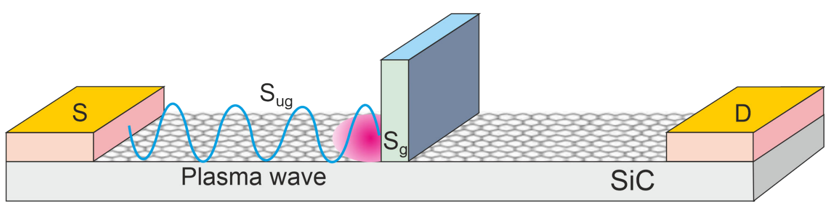

Fig. 24. The detection mechanism in a graphene FET THz

3.2. *Responsivity-enhanced graphene-based detectors*

Due to the unique electronic and optical properties of 2D materials, many impressive achievements of detectors made on its basis, such as ultrafast photoresponse, high responsivity and ultrabroad detecting band have been reported. As previously mentioned, most of the best graphene photodetectors are built based on p-n junctions or Schottky barriers (to separate photogenerated carriers), and FET transistors. The two major challenges determine a development of high responsivity graphene photodetectors. The first is a low optical absorption in a thin active region (~ 100 - 200 nm), while the second is a short carrier lifetime. It means that a trade-off between a high responsivity and an ultrafast response time must be met, particularly in a broadband operation.

Responsivity improvement in grapheme detectors can be reached by increasing the photocarrier lifetime through both band structure and defect engineering, where carrier trapping mechanisms and patterned graphene nanostructures have been employed to introduce bandgap and mid-gap defect states while the response time is limited by a long carrier trapping time due to introduced defect states [10,31,32,60-62,71-75].

The enhanced responsivity can also be obtained in a hybrid photoconductor - a graphene photoconductor with an additional light absorption region. The built-in electric field at the interface of graphene and light absorption region can efficiently separate the photoinduced carriers generated at the active layer and, then, inject them (electrons/holes) into the graphene. The photo-response provided by graphene is reinforced in this way. Several kinds of novel responsivity-enhanced photodetector structures consisting of graphene and additional light absorption mediums (e.g., QDs, fluorographene, nanowires, and bulk semiconductors) are presented in Table 3 [1].

Table 3
Responsivity-enhanced graphene-based detectors [after Ref. 1].

	Advantages	Disadvantages	References
Hybrid graphene quantum dots (GQD) detector V_{DS}, V_{GS}, Au, Quantum dots, Graphene, SiO_2, Si substrate	Increased absorption and introduction of large carrier multiplication factors	Bandwidth and response time are limited by a narrow spectral bandwidth and long carrier trapping times of quantum dots	59, 76–80
Graphene-fluorographene detector V_{DS}, V_{GS}, Au/Cr, Fluorographene, Graphene, SiO_2, Si substrate	Three orders of magnitude enhanced responsivity compared to pristine graphene detectors. Broadband photoresponse from the ultra-violet to the mid-infrared wavelengths	Fluorographene partially decomposes over time. The slow response time is given by trap states in the fluorographene.	81
Two graphene layers separated by a thin tunnel barrier Graphene layers, Substrate, Barrier layer	Broadband responsivity via separation of photogenerated electrons and holes through quantum tunnelling and minimization of their recombination	Response times limited by long carrier trapping times in the tunnelling barriers	82, 83
Waveguide integrated graphene detector Graphene, Au, Si rib wavegaide, SiO_2	Ultrafast responsivity by increasing the interaction length of light within graphene and processing corresponding to standard photonic integrated circuits	Spectral bandwidth restricted by the bandwidth limitations of waveguides	84–87
Microcavities, plasmonic structures, and optical antenna integrated with graphene Antenna, Au, Pd, Graphene, SiN, SiO_2, Si burried wavegaide	High responsivities by increasing the interaction length of light within graphene	Bandwidth is limited by the resonant nature of the structures	26, 88–101

An example of the broadband absorption of a graphene quantum dot (GQD) detector reported by Zhang *et al.* is presented in Fig. 25 [43]. The response was shown from the visible (~532 nm), NIR (~1.47 µm), and MWIR (~10 µm) ranges with a photoresponse of 1.25, 0.2 and 0.4 A/W, respectively. The single layer graphene detector high responsivity [see Fig. 25(b)] is partially attributed to the internal gain.

Differences between a pure graphene photoconductor and a hybrid photoconductor are schematically shown in Fig. 26. Distinction between ultrafast and ultra-sensitive graphene photodetectors is also shown [18]. In early solutions of a metal-graphene-metal photodetector, the photocurrent was generated by a local lighting of one of the metal/graphene interfaces. Further solutions resulted from the mirror symmetry of the built-in potential profile in the

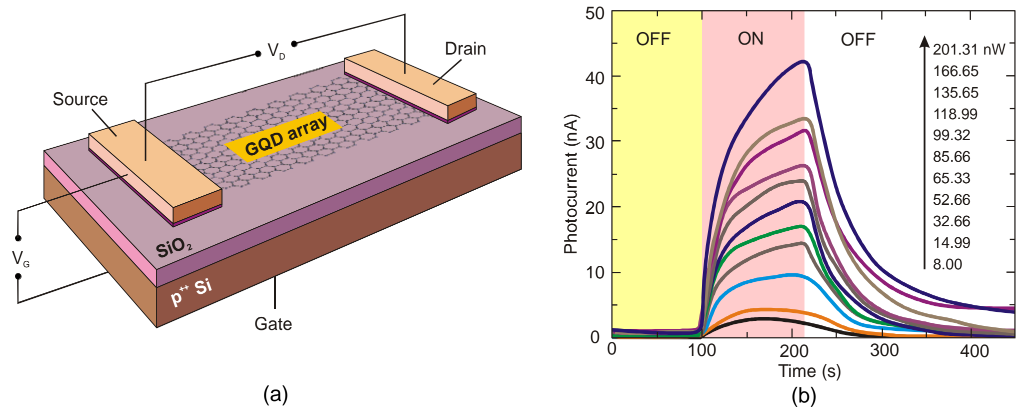

Fig. 25. Broadband GQD photodetector: device design (a) and slow response to light at 1.47 µm (b) [adapted after Ref. 75].

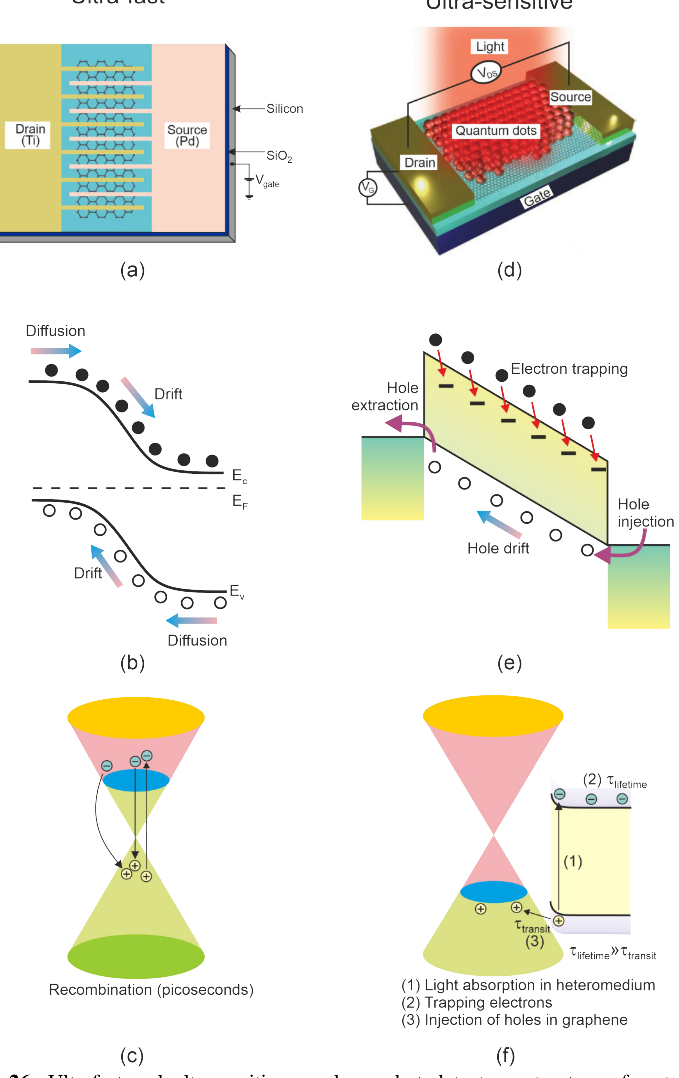

Fig. 26. Ultrafast and ultrasensitive graphene photodetectors: structure of metal-graphene-metal photodetector (a), band profile (b), recombination mechanism (c), hybrid GQD photodetector [after Ref. 59] (d), trapping process (e), and process dynamics at the interface of graphene/ quantum dots (f).

channel. By using an asymmetrical metallization scheme with metal fingers used to enlarge a light detection region [Fig. 26(a)], distribution of the electric field leading to the general photocurrent was obtained [Fig. 26(b)]. This design allows to operate at high data rates due to a graphene high carrier mobility and a short carrier lifetime [see Fig. 26(c)].

However, in the case of a hybrid photodetector [see Fig. 26(d)] its main feature is the ultrahigh gain resulting from a high carrier mobility of the graphene sheet and a charge recirculation due to carriers trapped in quantum dots [Fig. 26(e)], or another additional light absorbing region. Photoexcited holes in the quantum dots are transferred to the graphene layer and drifted by the bias V_{ds} to the drain, with the typical transit time, $\tau_{transit}$ being inversely proportional to the carrier mobility while electrons remain trapped (with the typical lifetime, $\tau_{lifetme}$) in the quantum dots. Multiple circulation of holes in the graphene channel following a single e-h photogeneration leads to the strong photoconductive gain, $g = \tau_{lifetme}/\tau_{transit}$ (see section 3.1.2), indicating the importance of long lifetime and high carrier mobility [18]. Konstantatos *et al*. has demonstrated the gain of 10^8 electrons per absorbed photon and the responsivity of ~10^7 A/W in short wavelength (SWIR) hybrid phototransistors [59].

Hybrid photodetectors offer high responsivity improvements. For example, Figure 27 shows the gain as a function of excitation intensity, for a hybrid single layer graphene/ZnO QDs detector. Experimental results (points) were compared to the theory (solid line) on the basis of which this structure may show a photoconductive gain as high as of 10^7. However, the majority of hybrid devices have a limited linear dynamic range due to the charge relaxation time which quickly saturates the available states for photoexcitation leading to a drop in responsivity with incident optical power [1].

The light-matter interaction in 2D materials to improve the photodetectors performance can be also reached by introducing optical structures (e.g., plasmonic nanostructures, photonic crystals, optical cavities, waveguides) on the device top. Two key factors are important: the size and shape matching of the metal pattern

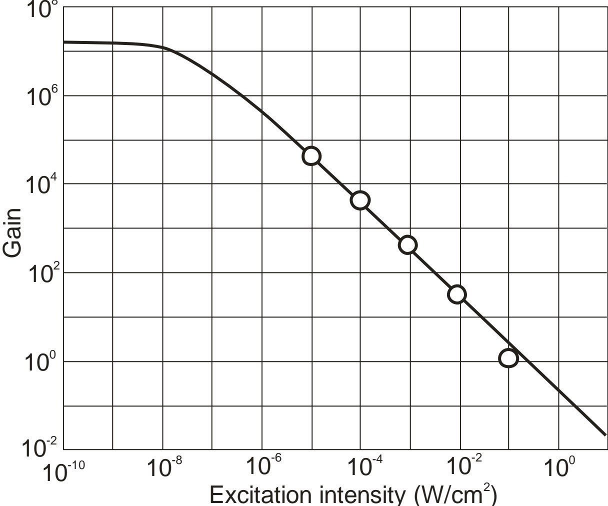

Fig. 27. Gain as a function of excitation intensity for the hybrid graphene/ZnO quantum dots detector. The circles are experimental data, and the solid curve is the theoretical plot with best fitting [after Ref. 78].

to generate plasmons and the plasmons coupling to the detector. The generation of plasmons depends significantly on the metallic pattern. Dimensions of metal grating should be like the width of a metal strip permitting plasmon fields to enter the detector below the grating. Usually, a thin dielectric layer is placed over detector and a metal grid is placed on the top of a dielectric layer. As the plasmons are travelling parallel to the surface, a large optical path can be reached for absorption without any requirement of having a thick active layer [18].

Improvement of the generation rate of photogenerated carriers and maintaining the adequate carrier lifetime is the most favorable approach to achieve a high responsivity with the fast photoresponse in graphene. That approach has been demonstrated for SWIR graphene photodetectors [102] - see Fig. 28. Under illumination, the light with a wavelength matching plasmonic resonance is trapped by Au-nanoparticles and is absorbed by graphene. A vertical built-in field is employed in the graphene channel for trapping photoinduced electrons and leaving holes in graphene resulting in a prolonged photoinduced carrier lifetime.

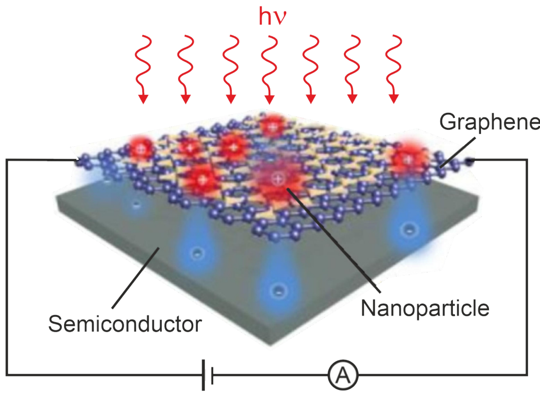

Fig. 28. The concept of SWIR graphene photodetector (adapted after Ref. 102).

Detector responsivity is enhanced by plasmonic Au nanoparticles and is the highest reported among the SWIR based on graphene – 83 A/W at 1.55 µm while response time is limited approx. to the level of 600 ns due to both traps in the surface of a hybrid structure and traps in nanoparticles. Despite that, the SWIR graphene detector is characterized by the fastest response time in the hybrid graphene photodetector/transistor [18].

The unique electrical and optical characteristics of gold patched graphene nanostripe photodetectors have been demonstrated by Cakmakyapan *et al*. [103]. Commercially available chemical vapour deposition (CVD) grown graphene was first transferred to a high resistivity silicon wafer covered with a 130-nm thick thermally grown SiO_2 layer. Next, gold patches, graphene nanostripes, Ti/Au contacts and gate pads were patterned by different combinations of optical lithography and plasma etching. The V_g applied to the Si substrate controls the E_F of the graphene nanostripes. The gold patches have a width of 100 nm, periodicity of 200 nm, height of 50 nm, length of 1 µm, and a tip-to-tip gap size of 50 nm, respectively (see Fig. 29).

Photodetector has an ultrabroad spectral response from the visible to the IR region with high responsivity levels

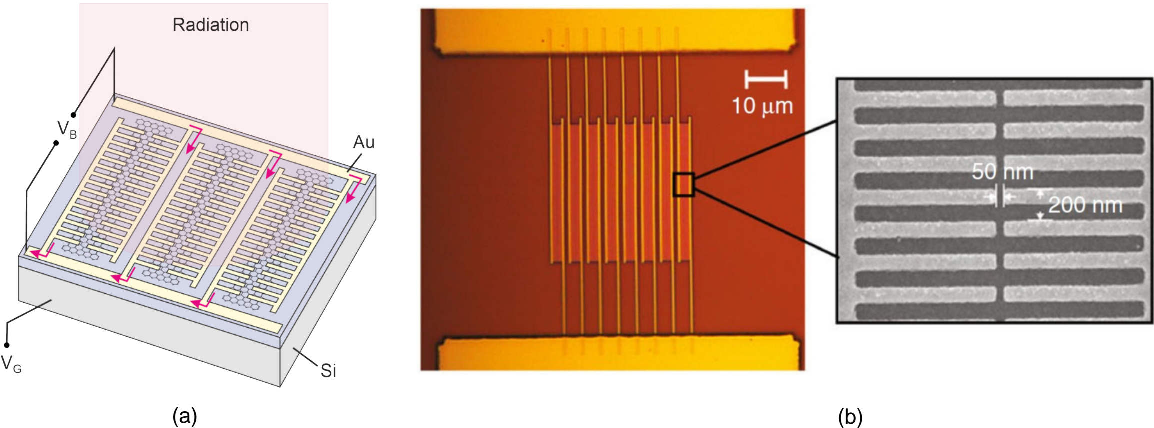

Fig. 29. Photoconductive nanostructures based on gold patched graphene nanostripes: photodetector principle of operation (a)

ranging from 0.6 A/W at a wavelength of 800 nm to 11.65 A/W at 20 µm, as presented in Fig. 30. That wide photodetection bandwidth and high responsivity are enabled employing the gold patched graphene nanostripes. As expected, higher photoconductive gains are reached at lower wavelengths, where excitation to higher energy levels contributes to the generation of subsequent e-h pairs by the energy transfer during relaxation (see the insert of Fig. 30).

Photodetector also shows a frequency response exceeding 50 GHz, what is more than seven orders of magnitude faster compared to the higher responsivity hybrid GQD [59,78] and tunnelling barriers [82]. Figure 31 compares response (time and frequency) high performance graphene-based photodetectors operating at room temperature and reported in the literature .

Another way to enhance the optoelectronic properties of graphene is its modification by a noncovalent and covalent functionalization. Due to a robust chemistry, graphene itself is a chemistry inert material. The so far established chemistries lead to graphene derivatives with a low degree of functionalization (typically 1-3%) [76]. Fluorographene (FGr) is prepared by a fluorination of graphene and a mechanical or chemical exfoliation of a graphite fluoride. The band gap of FGr can be tuned from ultraviolet to near-infrared by controlling a degree of fluorination. In Ref. 81 a Gr/FGr photodetector is demonstrated with a spectral range spanning from 255 nm to 4.3 µm. This broadband response arises from the quantum confinement of graphene regions by fluorine adatoms. Rehybridization of carbon with fluorine results in a mixture of sp^2 and sp^3 nanodomains, inducing a series of discrete states for trapping of photoexcited charge carriers. Despite the high photoresponsivity of a Gr/FGr photodetector over a broadband range, its operation speed is slow – of about 200 ms. It is suggested that the reason for it is the long-trapped carrier lifetime in both the sp^2 and the sp^3 domains.

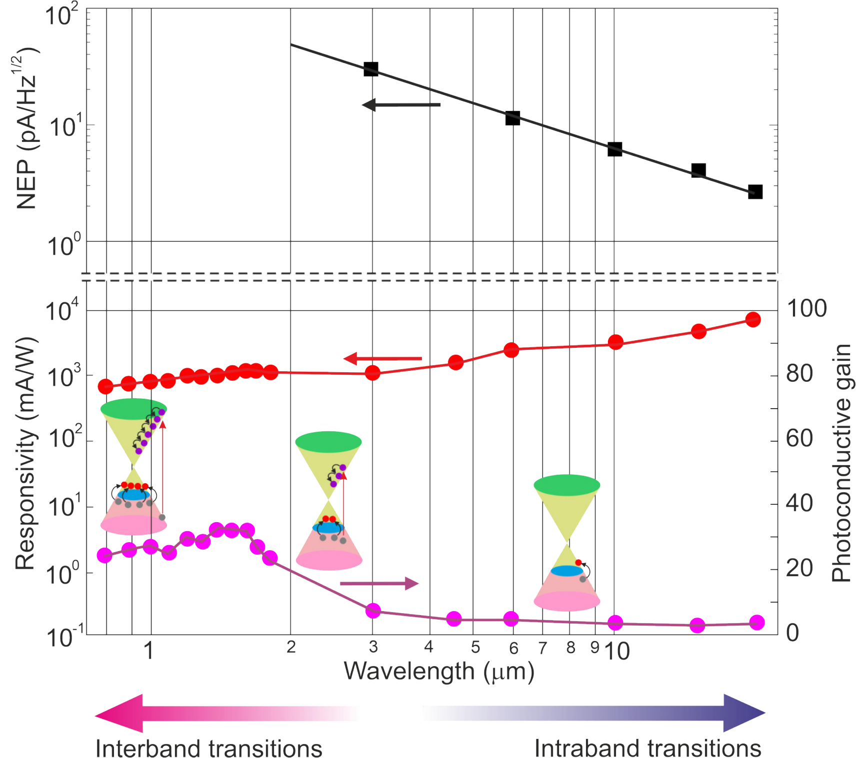

Fig. 30. Responsivity, photoconductive gain and *NEP* (optical chopping above 1 kHz) of the photodetector at optical power of 2.5 µW, gate voltage of 22 V, and bias of 20 mV [adapted after Ref. 103].

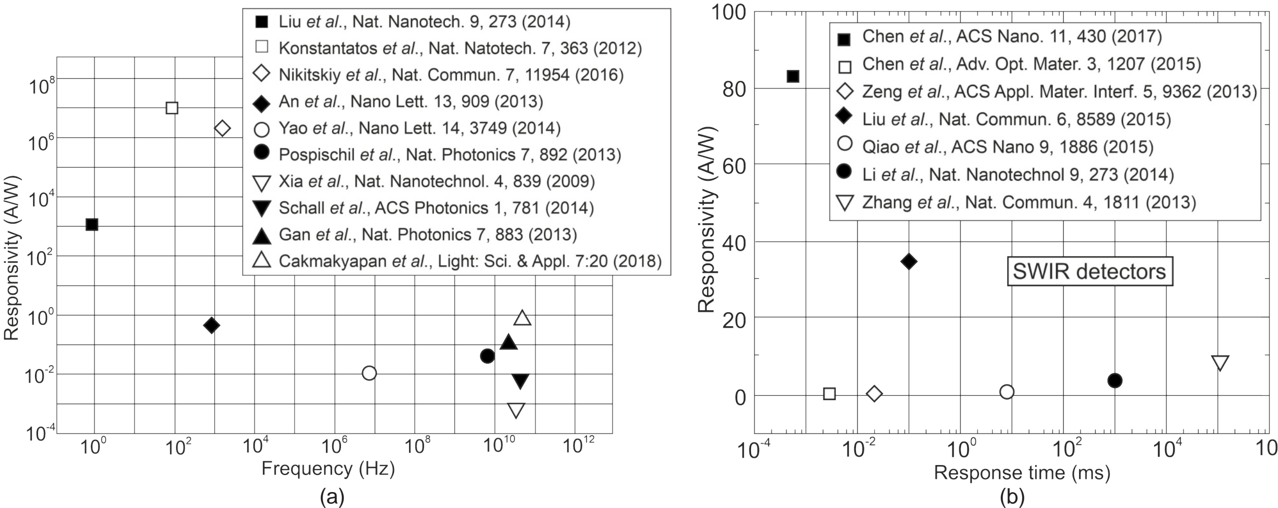

Fig. 31 comparison of the responsivity and response time and frequency for the room temperature graphene photodetectors reported in the literature, mainly in Ref. 102 (a) and Ref. 103 (b).

3.3. *Graphene-based thermal detectors*

Thermal detectors are classified according to the operating schemes as thermopiles, bolometers, and pyroelectric detectors.

The basic structure of a thermoelectric graphene photodetector design is shown in Fig. 32 [64]. This device, made of a sheet of graphene with dual split-backgates, develops a photovoltage across electrodes M1-M2 as a function of the voltage applied to the backgates. The device shows photoresponse even at 10.6 μm, what indicates that absorption is not limited due to the Pauli blocking in graphene, but the most of the light absorption is done in the substrate underneath, while graphene devices are using the thermoelectric effect to convert temperature rise in the substrate to a voltage difference as is described by Eq. (11): $\Delta V = (\alpha_p - \alpha_n)\Delta T$, where $(\alpha_p - \alpha_n)$ is the difference of the Seebeck coefficient between the p- and n-region of graphene, and ΔT is the temperature difference between the graphene p-n junction and the metal contacts.

Hsu *et al.* have demonstrated a graphene-based thermal imaging system by integrating graphene based photo-thermo-electric detectors with micromachined silicon nitride membranes [104]. As is shown in Fig. 32, multiple graphene photodetectors are combined into the thermopile composed of an infrared absorber that is suspended from the substrate, a series of thermal arms that connect the absorber and the surrounding, with interleaved p- and n-type graphene channels on top. Incident of IR radiation causes heating of the absorber (dielectric multilayer thin film) which can, then, be probed electrically by graphene p-n junctions due to the thermoelectric effect. Thanks to the use of an optimized IR absorption layer made of a $SiO_2/Si_3N_4/SiO_2$ combination deposited using plasma enhanced chemical vapour deposition (PECVD), the absorption in the 8-12 μm spectral range has achieved > 40%. The fabrication of a free-standing absorber membrane was made after undercutting the silicon underneath with XeF_2 isotropic etching.

Figure 33 shows multiple graphene photodetectors combined into the thermopiles composed of an infrared absorber that is suspended from the substrate, a series of thermal arms connecting the absorber and the surrounding, with interleaved p- and n- type graphene channels on top.

It can be shown that if the thermopile detectivity is limited by the Johnson noise, then D^{*2}/τ (where τ is the response time) is independent of the lateral geometry [64]:

$$\frac{D^{*2}}{\tau} = \frac{\alpha_{abs}}{t} \cdot \frac{\Delta\alpha_S^2}{\rho_{2D}} \cdot \frac{1}{k_{th}c_v} \cdot \frac{1}{16kT}. \quad (15)$$

Here the first term (α_{abs}/t) is the absorbance per thickness, t, indicating the capability of IR absorption of the absorber; the second term $\Delta\alpha_S^2/\rho_{2D}$ with 2D resistivity of graphene is determined by the electrical and thermo-

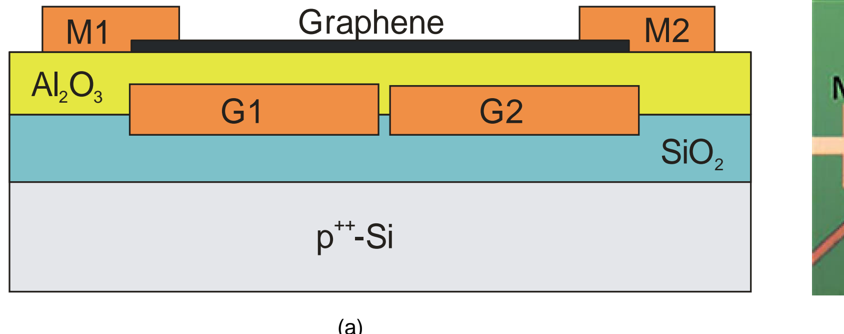

(a)

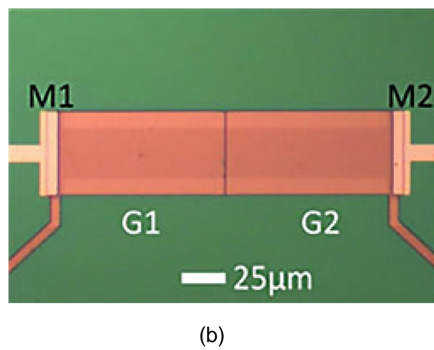

(b)

Fig. 32. Schematic graphene split-gate thermopile with supported substrate (a) and its microscopic image (b). M1 and M2 are metal contacts to graphene, and G1 and G2 are split gates that electrostatically dope the graphene channel to form a p-n junction (after Ref. 64).

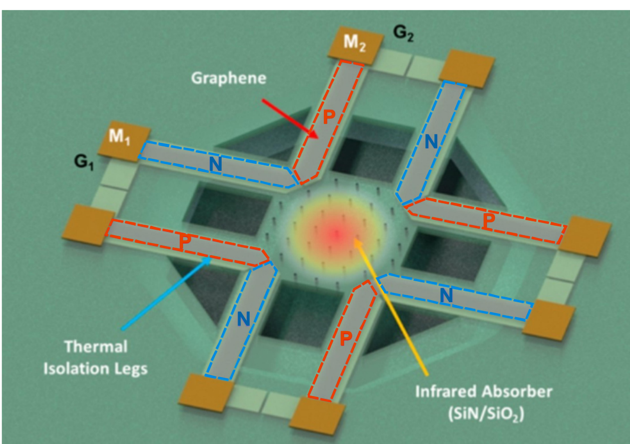

Fig. 33. Graphene thermopile with a suspended IR absorber: the red and blue regions indicate the p-type and n-type region of graphene, and the square in the centre is the dielectric absorber. The whole structure is suspended on the substrate to reduce the thermal conductance in the vertical direction [after Ref. 64].

electrical properties of the sensing material, also called as the thermoelectric figure of merit (FOM) for thermopile IR detectors; the third term $1/\kappa_{th}c_v$ is the thermal transport factor and indicates the quality of thermal isolation, with κ_{th} denoting the thermal conductivity of the absorber, and c_v is the specific heat capacity.

The Seebeck coefficient *vs*. resistivity for different 2D and 3D bulk materials is shown in Fig. 20. In order to benchmark graphene-based thermoelectric detectors with respect to the other material systems, the FOMs are plotted as a function of resistivity in Fig. 34. As is shown, the FOM for today's standard CVD graphene on SiO_2, with the average mobility of 2000 cm^2/Vs can already outperform the performance of any thermopiles made with metals and most of thermoelectric materials. It is predicted that the use of a higher quality properly passivated graphene could make the FOM two orders of magnitude higher than that of all the other material systems [64]. We can also see that the FOM of 2D TMDs is higher than in their 3D counterparts, which indicates their great potential for thermal detection and other thermoelectric applications.

Figure 35 compares the detectivity and the response time of graphene thermopiles with different types of state-of-the-art thermal detector technologies, including bolometers (VO*x*, etc.), thermopiles (poly-Si, Al, thermoelectric materials, etc.), and pyroelectric devices (PZT and other piezoelectric materials). For more advanced thermal detector technologies, the detectivity magnitude at room temperature is in the order of ~10^8-10^9 cmHz$^{1/2}$/W. As is shown, the performance of the current graphene thermopile technology is considerably inferior in comparison with the state-of-the-art thermal detectors and is below 10^6 cmHz$^{1/2}$/W. However, the theoretically predicted performance is even better than today's state-of-the-art technologies. For example, a 10 nm thick absorber with a good mechanical stability and 50% absorption achieved through nano-photonic structures, would make graphene thermopiles better than any existing bolometers.

The bolometer key parameters are the thermal resistance and the heat capacity. It was presented that graphene assumes low volume for a given area and low density of states resulting in low heat capacity exhibiting a fast device response.

Two types of graphene-based bolometers are shown in Fig. 36. Yan *et al*. has considered graphene as a hot electron bolometer [105] shown in Fig. 36(a). Due to a weak electron-phonon interaction, they used a bilayer graphene exhibiting tuneable bandgap. Implementation of perpendicular electric field gives rise to an electron temperature dependent resistance at low temperature, making the device suitable for thermometry. The extrapolated noise equivalent power (*NEP*) value for a 1 μm^2 sample at 100 mK is approx. 5×10^{-21} W/Hz$^{1/2}$ similarly to the TES (transition edge sensor) state of the art bolometer. The graphene-based detector structure with a temperature coefficient of resistance (TCR) above 4%/K is shown in Fig. 36(b), where the pyroelectric response of a $LiNbO_3$ crystal is transduced with a high gain (up to 200)

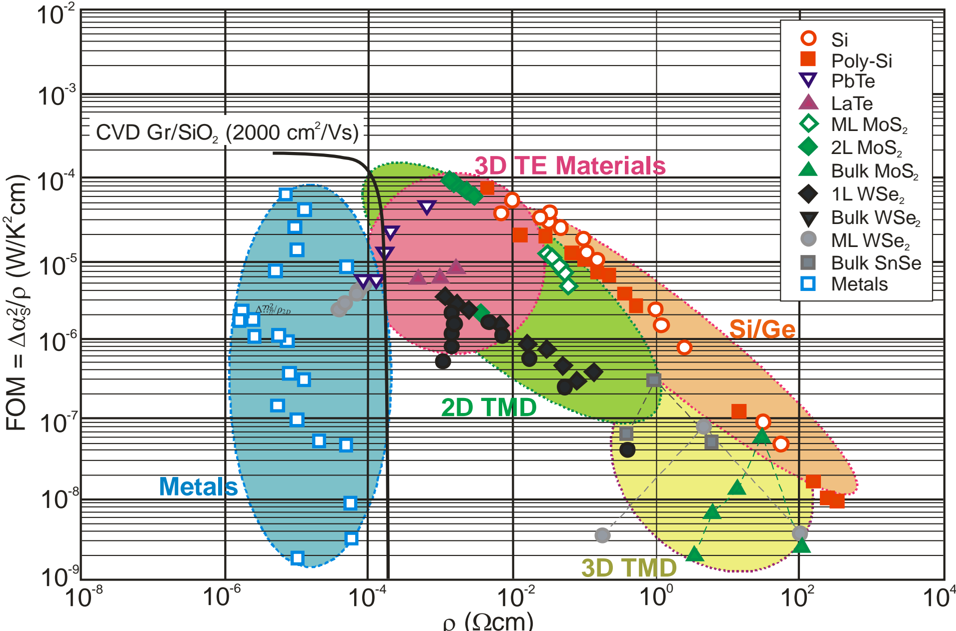

Fig. 34. The thermoelectric figure of merit as a function of resistivity for various materials [after Ref. 64].

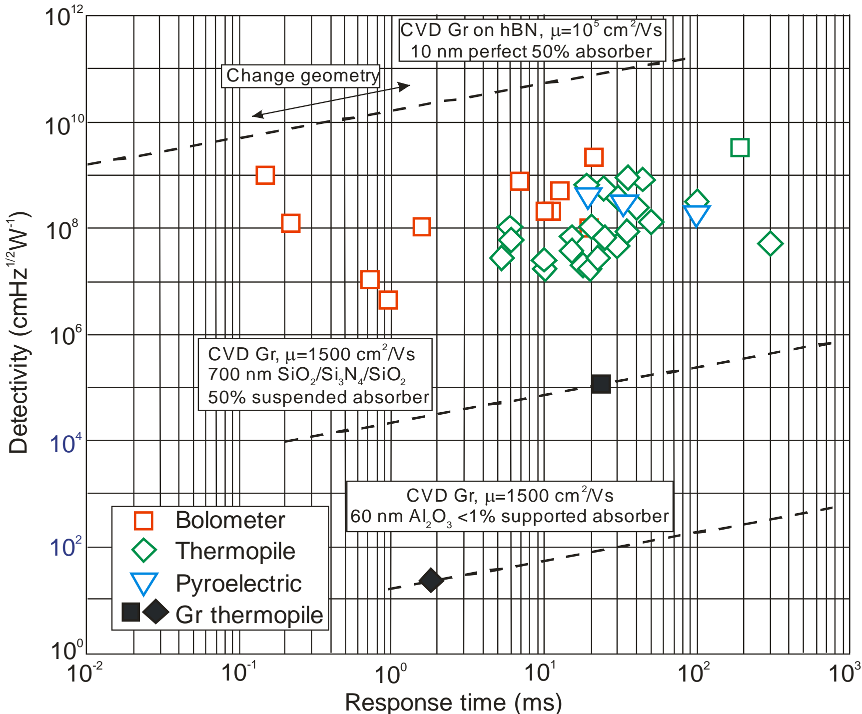

Fig. 35. Detectivity *vs.* response time for different technology nodes of graphene thermopiles in comparison with mainstream uncooled thermal IR detectors [after Ref. 64].

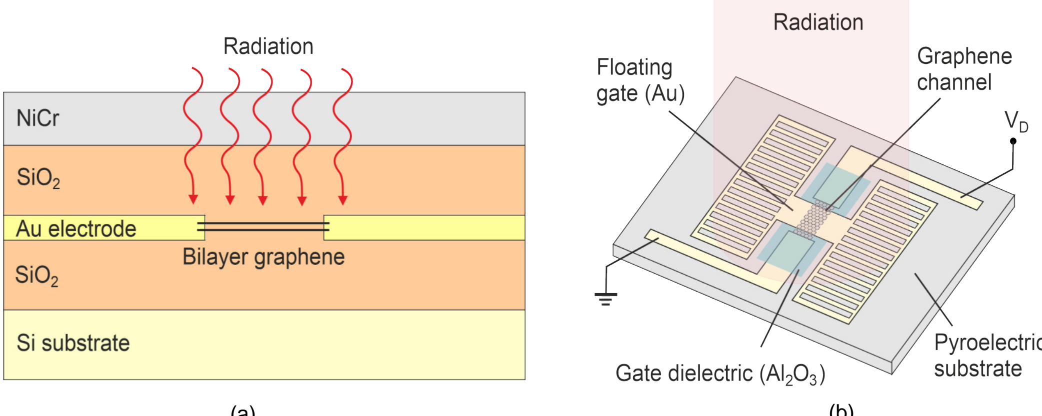

Fig. 36. The graphene bolometers: side view of the bilayer graphene hot electron bolometer (a) (semitransparent NiCr top gate covers the graphene device and SiO_2 surrounds the graphene) and pyroelectric bolometer (b) (conductance of graphene channel is modulated by the pyroelectric substrate and by a floating gate) [after Ref. 18].

into modulation for graphene [106]. That effect is reached by fabrication of a floating metallic structure concentrating the pyroelectric charge on the top gate capacitor of the graphene channel.

The main difficulty in a development of high sensitivity graphene bolometers is the weak variation of electrical resistance *vs.* temperature. Recently published papers by El Fatimy *et al.* [107] have shown that graphene QDs on SiC exhibit extremely high variation of resistance *vs.* temperature due to a quantum confinement, higher than 430 MΩ/K at 2.5 K leading to the responsivities of 1×10^{10} V/W for the THz region. In hot electron bolometers with QDs in epitaxial graphene, the bandgap is induced via quantum confinement (without the need of gates) using a simple single layer structure. *NEP* for 0.15 THz *vs.* temperature from 2.5 K to 80 K calculated for a 30-nm and 150-nm QDs are presented in Fig. 37. *NEP* is approximately one order of magnitude lower than the best commercial cooled bolometer and much faster in a response time (a few nanoseconds, compared to milliseconds for commercial bolometers). These QD bolometers operate in the very broad spectral range from THz to ultraviolet radiation with a responsivity being independent *vs.* wavelength - see Fig. 37(b). Similarly, as for hybrid photodetectors (see Fig. 27), drop of responsivity *vs.* absorber power is also observed for graphene bolometers [see Fig. 37(b)].

Due to such unique properties as the lowest mass per unit area, extreme thermal stability and incomparable with other materials spectral absorbance, graphene rises interest as an active area for the bolometer. However, graphene has failed to challenge the state-of-the-art at room temperature due to its weakly temperature-dependent electrical resistivity. Moreover, a sensitive bolometer is often slow. This is due to the inverse proportionality of both the speed and the sensitivity to the thermal resistance. Thus, the

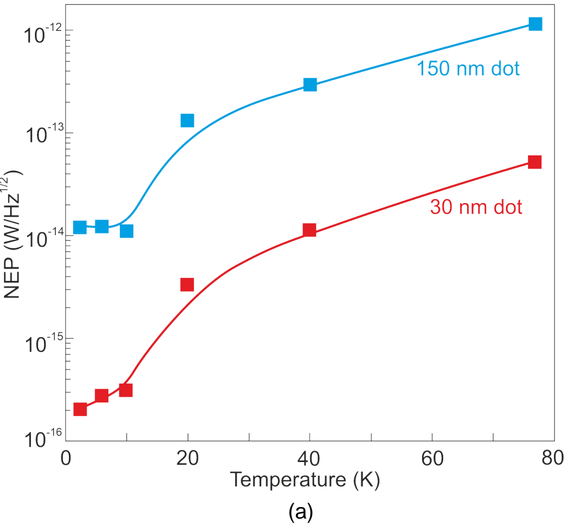

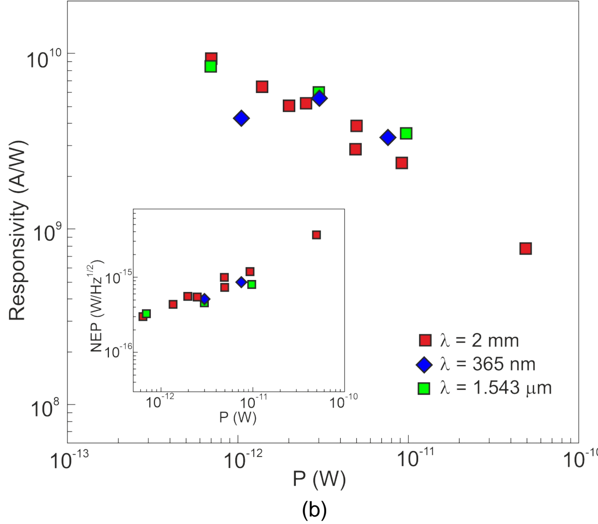

Fig. 37. Quantum dot bolometers: *NEP vs.* temperature at 0.15 THz for 30 nm and 150 nm quantum dots (a) (adapted after Ref. 107) and responsivity *vs.* absorbed power at different wavelength. Inset: *NEP vs.* absorbed power at selected wavelengths (b) (adapted after Ref. 108).

change of the thermal resistance between the bolometer and its environment is most commonly used to modify the speed and sensitivity.

In a departure from the conventional bolometer, a graphene nanoelectromechanical system has been proposed to detect light via resonant sensing. In the design proposed by Blaikie *et al*. [109], absorbed light heats and thermally tensions a suspended graphene resonator, thereby shifting its resonant frequency. Figure 38 illustrates a schematic design of the graphene resonator comprising the suspended graphene membrane. The graphene nanomechanical bolometer (GNB) is made by transferring graphene onto a Si/SiO_2 support substrate with patterned holes, resulting in circular drumhead resonators. Some drumheads are patterned into trampoline geometries using a focused ion beam technique. The most sensitive device has a 6-μm diameter trampoline with 200 nm wide tethers. To driver motion of the graphene resonators, the AC. voltage between the graphene and the backgate was applied.

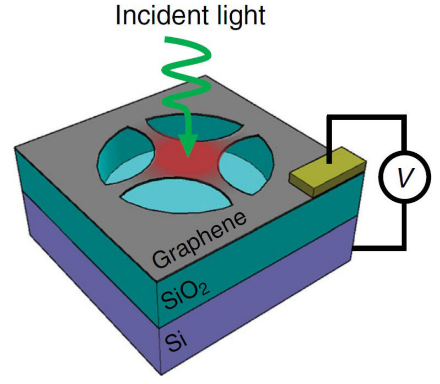

Fig. 38. Design of nanomechanical graphene resonator [after Ref. 109].

Upon absorbing light, the membrane temperature increases and the resulting thermomechanical stress shifts the resonance frequency by an amount [109] of:

$$\Delta f_0 = \frac{\alpha Y f_0}{2\sigma_0(1-\nu)}\Delta T \, , \tag{16}$$

where α is the thermal expansion coefficient, ν is the Poisson ratio, σ_0 is the initial in-plane stress, Y is the two-dimensional elastic modulus, f_0 is the initial frequency, and ΔT is the temperature change. For typical graphene nanomechanical resonators, a $\Delta T \sim 100$ mK will shift the frequency by a full linewidth, a sizable amount that is readily measured.

Figure 39 shows the frequency responsivity to the absorbed light by a time recording of f_0 when the GNB is exposed to a sinusoidally modulated light and the absorber

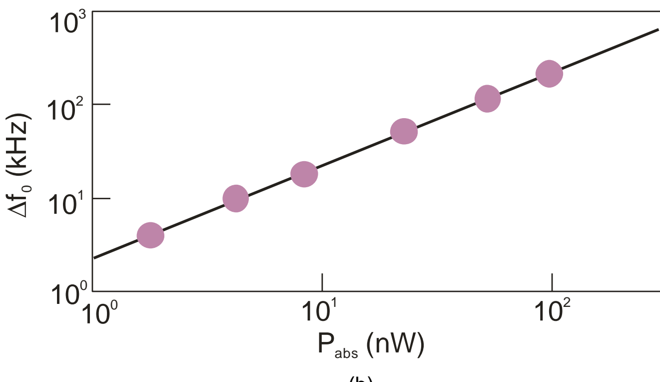

Fig. 39. Frequency responsivity to the absorbed light of a graphene resonator: (a) mechanical resonance frequency *vs.* time for an 8-μm diameter trampoline with 500-nm wide tethers. The device is subject to 190 nW of incident radiation modulated at 40 Hz; (b) measured resonance shift *vs.* absorbed power, the absorbed power of 4.4 nW causes a frequency shift of $\Delta f_0 = 8.5$ kHz [after Ref. 109].

power of 4.4 nW. A best-fit line to this data yields a 2.3-kHz/nW resonance shift per incident power.

The GNB device has achieved a sensitivity of 2 $pW/Hz^{1/2}$ and a bandwidth up to 1 MHz, thus demonstrating the previously unattainable sensitivity at room temperature, and greatly outperforming the speed of state-of-the-art room-temperature bolometers [109].

3.4. Graphene-based terahertz detectors

Various detection mechanisms are involved in terahertz 2D material detectors including bolometric effect, PTE effect, plasma wave rectification in FET, and so on. The performance of representative detectors [110] is summarized in Table 4. Detectivity is estimated from equation $(A\Delta f)^{1/2}/NEP$, where NEP values are obtained from the references.

THz response can be attributed the PTE effect as a result of the asymmetric thermal distribution. Cai *et al.* reported a sensitive graphene PTE THz detector with asymmetric electrodes [113]. On account of dissimilar metal contacts, the Fermi energy and Seebeck coefficient are asymmetric across the device channel which leads to a photovoltage under incident radiation. In addition, the gate voltage may tune the Fermi energy of graphene, thus influencing the photoresponse. The detector response time is mainly determined by the thermal time constant of graphene which is of about 100 ps.

Also, Tong *et al.* have demonstrated a half-edge contacted graphene PTE detector with asymmetric electrodes - see Fig. 40 [114]. Its sensitivity was enhanced by a double-patch antenna and an on-chip silicon lens reaching a maximum responsivity of 4.9 V/W and a typical D^* of ~ 2.2 × 10^6 Jones.

Different modifications of a detector design have been proposed to improve sensitivity. One of them is a resonant structure consisting of two graphene sheets separated by

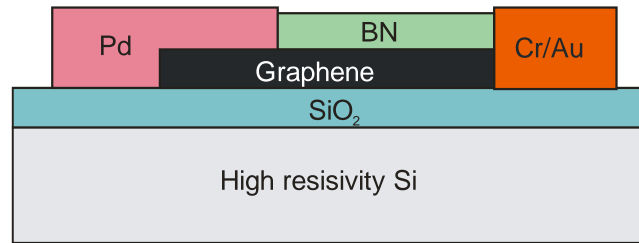

Fig. 40. Schematic side view of the THz PTE detector design.

Table 4
Terahertz detectors based on 2D materials [after Ref. 110].

Mechanism	Material	Frequency	Responsivity	*NEP*	Detectivity	Response time	*T*	Ref.
Bolometer	bP	~ 0.3 THz	7.8 V/W	4 $nW/Hz^{1/2}$	~ 1.2×10^7 Jones	< 1 ms	300 K	111
Bolometer	Graphene	0.3-1.6 THz	-	5.6 $pW/Hz^{1/2}$	~ 3.3×10^9 Jones	< 100 µs	3 K	112
Bolometer	Graphene	0.15 THz	5×10^{10} V/W	0.2 $fW/Hz^{1/2}$	~ 2.2×10^{12} Jones	< 2.5 ns	300 K	107
PTE	Graphene	2.52 THz	> 10 V/W	1.1 $nW/Hz^{1/2}$	~ 1.9×10^5 Jones	< 110 ps	300 K	113
PTE	Graphene	2 THz	> 4.9 V/W	1.7 $nW/Hz^{1/2}$	~ 2.2×10^6 Jones	< 50 ms	300 K	114
PTE	bP	~ 0.3 THz	> 0.15 V/W	40 $nW/Hz^{1/2}$	~ 1.2×10^6 Jones	< 2 ms	300 K	115
PTE	bP	~ 0.3 THz	> 1.1 V/W	45 $nW/Hz^{1/2}$	~ 1.0×10^6 Jones	< 2 ms	300 K	111
FET	Graphene	~ 0.3 THz	> 0.15 V/W	30 $nW/Hz^{1/2}$	~ 1.5×10^6 Jones	< 1 ms	300 K	116
FET	Graphene	~ 0.6 THz	> 14 V/W	515 $pW/Hz^{1/2}$	~ 4.9×10^7 Jones	< 30 µs	300 K	117
FET	Graphene	~ 0.3 THz	> 1.2 V/W	2 $nW/Hz^{1/2}$	~ 2.3×10^7 Jones	< 2.5 ms	300 K	118
FET	Graphene	~ 0.3 THz	> 30 V/W	163 $pW/Hz^{1/2}$	~ 3.0×10^8 Jones	< 5 µs	300 K	119
FET	bP	~ 0.3 THz	> 5 V/W	10 $nW/Hz^{1/2}$	~ 4.8×10^6 Jones	< 10 ms	300 K	111
FET	Graphene	230-375 GHz	> 0.25 V/W	10 $nW/Hz^{1/2}$	~ 5.8×10^5 Jones	< 1.2 ms	300 K	120
FET	Graphene	0.13 GHz	> 20 V/W	0.6 $nW/Hz^{1/2}$	~ 1.9×10^8 Jones	-	300 K	121
FET	bP	0.15 THz	> 300 V/W	1 $nW/Hz^{1/2}$	~ 1.7×10^6 Jones	< 4 µs	300 K	122
FET	Graphene	0.15 THz	> 400 V/W	0.5 $nW/Hz^{1/2}$	~ 3.5×10^8 Jones	< 20 µs	300 K	123

a dielectric layer to tune the absorbed wavelength as presented in Table 3. The responsivity of that detector exhibits the peaks when frequency of inducing THz radiation reaches resonant plasma frequencies being tuned by the bias [82]. In order to observe the detector resonant response, the frequency of electron collisions with impurities and acoustic phonons must be sufficiently low. Double-graphene layered (DGL) heterostructures deploying inter-graphene layer intra-band transitions show that such structures can be exploited for efficient and tunable THz/IR lasers and photodetectors [124].

DGL heterostructure consists of a narrow potential barrier like BN and WS_2 sandwiched by two layers of graphene [Fig. 41(a)]. The voltage ($V_{top\text{-}bottom}$) applied between the source and drain combined with the gate voltage V_g modulates the Fermi levels and forms a P-i-N structure [Fig. 41(b)]. The system is in resonance when the energies of Dirac points of two layers of graphene are exactly the same [110]. The resonant tunnelling between two layers of graphene, with conservation of energy and momentum, results in a negative differential conductance. A photocurrent is generated due to the band-offset (Δ) between two Dirac points ($\hbar\omega$), and the transverse-magnetic (TM) polarized photons with energy of $\hbar\omega \sim \Delta$ can mediate the electron photon assisted resonant tunnelling in two layers of graphene. Yadav *et al*. reported the first experimental observation of the double graphene layered heterostructure THz detector [124].

At room temperature, the length of a plasma wave propagation is smaller than the length of the FET channel. Thus, room temperature FET THz detectors usually operate in a resistive self-missing regime. The plasma waves excited by THz radiation could be overdamped and, thus, the detectors did not operate in the resonant regime as was demonstrated by Vicarelli *et al.* [116]. The first THz FET detector based on the monolayer and bilayer graphene was exfoliated on Si/SiO_2. In order to satisfy the boundary condition, the logarithmic antenna ends were gate and source, respectively, while the drain was a metal line leading to a small pad [110]. The plasma wave FET with a top gate antenna coupled configuration are shown in Fig. 42(a). These detectors demonstrated a $NEP \sim 10^{-9}$ $W/Hz^{1/2}$ in the range of 0.29-0.38 THz. It was reported that during the measurements of a target at room temperature, the bilayer graphene based FET at gate voltage, $V_g = 3$ V was mounted on an x-y translation stage having a spatial resolution of 0.5 μm [116]. THz image consists of 200 × 550 scanned points collected by the object raster

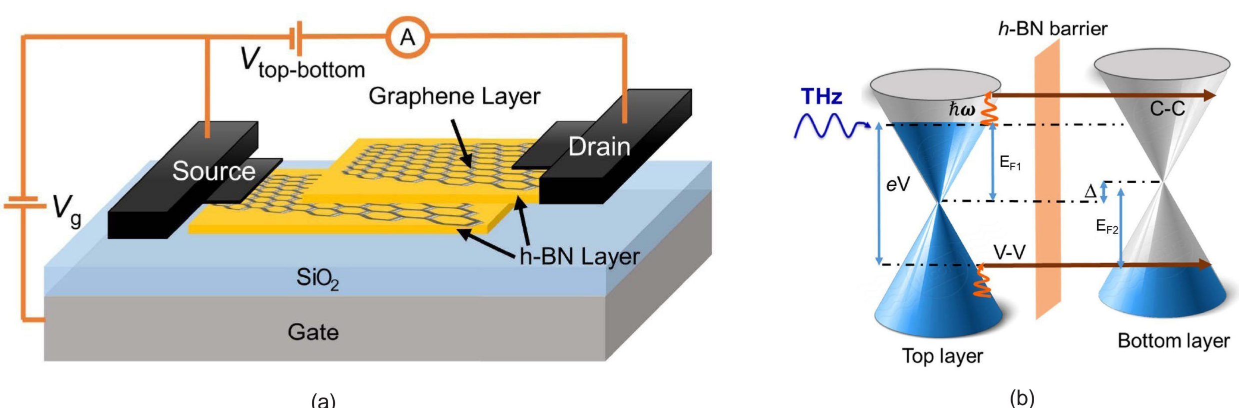

Fig. 41. Double-graphene layered (DGL) heterostructure: (a) schematic of the fabricated DGL device, (b) band diagrams of the DGL detector structures with photo-absorption-assisted inter-GL transitions. Wavy arrows indicate the inter-GL radiative V−V and C−C transitions. The inter-GL transitions work for the TM-mode THz photon radiations in the structure [after Ref. 124].

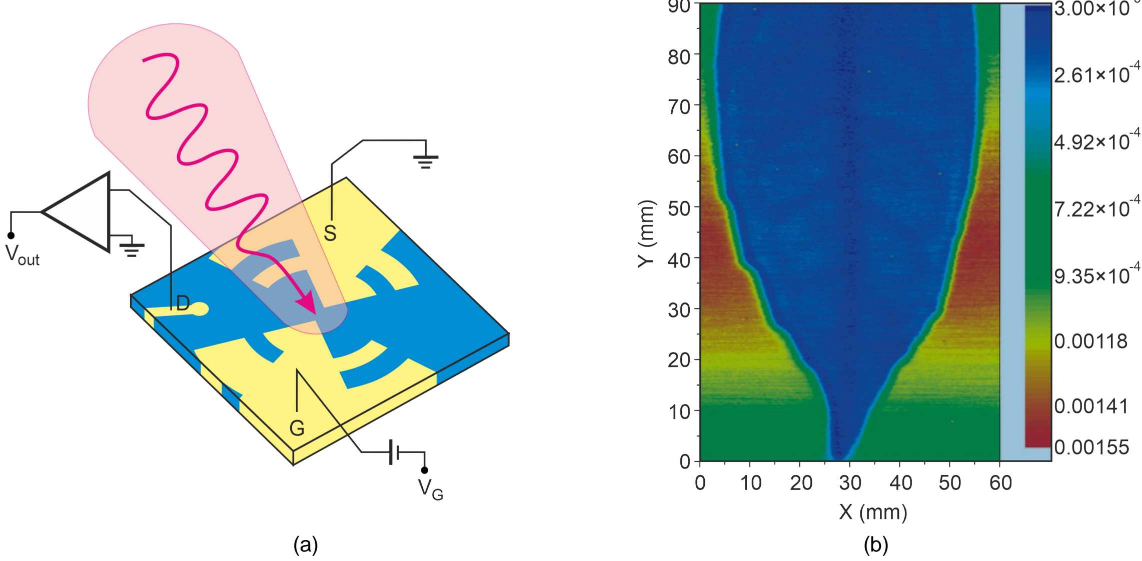

Fig. 42. Plasma wave FET THz detector: THz detection configuration in a FET embedding the optical image of the central area of a bilayer graphene-based FET (a) and 0.3 GHz transmission mode image of a leaf (b) [adapted after Ref. 116].

scanning in the beam focus, with an integration time of 20 ms/point [see Fig. 42(b)]. Further study carried out by Spirito *et al.* [118] revealed influence of the gate configuration in a bilayer graphene FET detector. The device exhibited better performance by employing wide-gate geometries or buried gate configurations [Fig. 43(b)], where a responsivity of 1.2 V/W was achieved.

More recently, improvements in THz detection have been described by Liu *et al.* [123,125]. Detector was built from a split-finger gated graphene-based FET coupled with a logarithmic antenna. Its *NEP* value determined by the Johnson-Nyquist noise was less than 0.1 nW/Hz$^{1/2}$ at both 0.04 and 0.14 THz. The achieved performances are competitive with those of commercially available detectors, in terms of both sensitivity and *NEP*.

In comparison with plasmonic THz detectors fabricated by exfoliated graphene [118] or CVD deposited on Si/SiO_2 substrates [116], the epitaxial graphene grown on SiC is much more promising [125]. The bilayer graphene (deposited on a SiC substrate) FET channel photoresponsivity and *NEP* were estimated in the level of 0.25 V/W and 80 nW/Hz$^{1/2}$, respectively.

3.5. Graphene-based detector performance - the present status

Since its discovery, graphene has been extensively studied for a potential service as a photodetector in a wide range of electromagnetic spectrum, where the majority of research has been devoted to visible and NIR photon detectors [31,32,60,72,110]. Photodetectors performance is mainly dependent on the inherent characteristics of the photodetector active layers, such as absorption coefficient, e-h pair lifetime and charge mobility. The high dark current of conventional graphene materials arising from the gapless nature of graphene significantly reduces the photodetector sensitivity and restricts further development of graphene-based photodetectors [18]. Performance of graphene-based infrared photodetectors is gathered in Table 5 [32,76].

Spectral responsivity of graphene photodetectors operating in the visible and NIR spectral ranges is compared with a commercially available silicon and InGaAs photodiodes in Fig. 44. The experimental results are taken with Ref. 126 and many other papers. The highest current responsivity, above 10^7 A/W, has been achieved for hybrid GQD photodetectors with enhancement trapped charge lifetimes. As is shown, graphene high mobility together with the enhanced-trapped charge lifetimes in the quantum dots produced a photodetector responsivity, up to seven orders of magnitude higher in comparison with standard bulk photodiodes, where $g \approx 1$. Higher responsivity of a Si avalanche photodiode (APD), up to 100 A/W, is caused by an avalanche process. The high responsivity allows for fabrication of devices suitable for measuring low level signals. However, due to the long lifetime of the traps, the demonstrated frequency response of 2D material photodetectors is very slow (< 10 Hz), what considerably limits real detector functions.

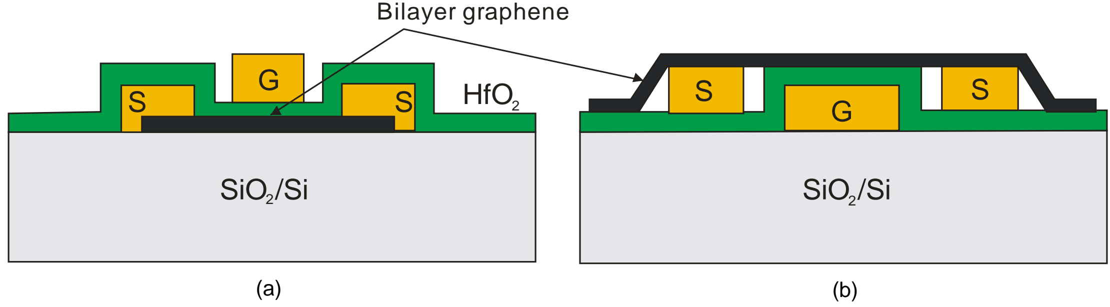

Fig. 43. Schematic bilayer graphene FET with top (a) and buried (b) gates [after Ref. 118].

Table 5
Infrared photoresponsivity of graphene-based materials [after Ref. 18].

Materials	Wavelength	Responsivity (A/W)	Bias (V)	Gain (%)	Time	Detectivity (Jones)
Graphene	1 mm (0.3 THz)	0.07-0.15 V/W	0			
Graphene	30-220 μm	(5-10)×10^{-9}	0.1		10 ps, 50 ps	
Graphene	1550 nm	0.5×10^{-3}			0.26 s,	3.3×10^{13}
Graphene/Si waveguide	2750 nm	0.13	1.5			
$PbSe/TiO_2$/Graphene	350-1700 nm	0.506-0.13	-1		50 ns, 83 ns	3×10^{13}
Graphene/PbS	350-1700 nm	5×10^7	5	10^8	10-20 ms	7×10^{13}
Graphene/Ti_2O_3	3-13 μm	~ 100				

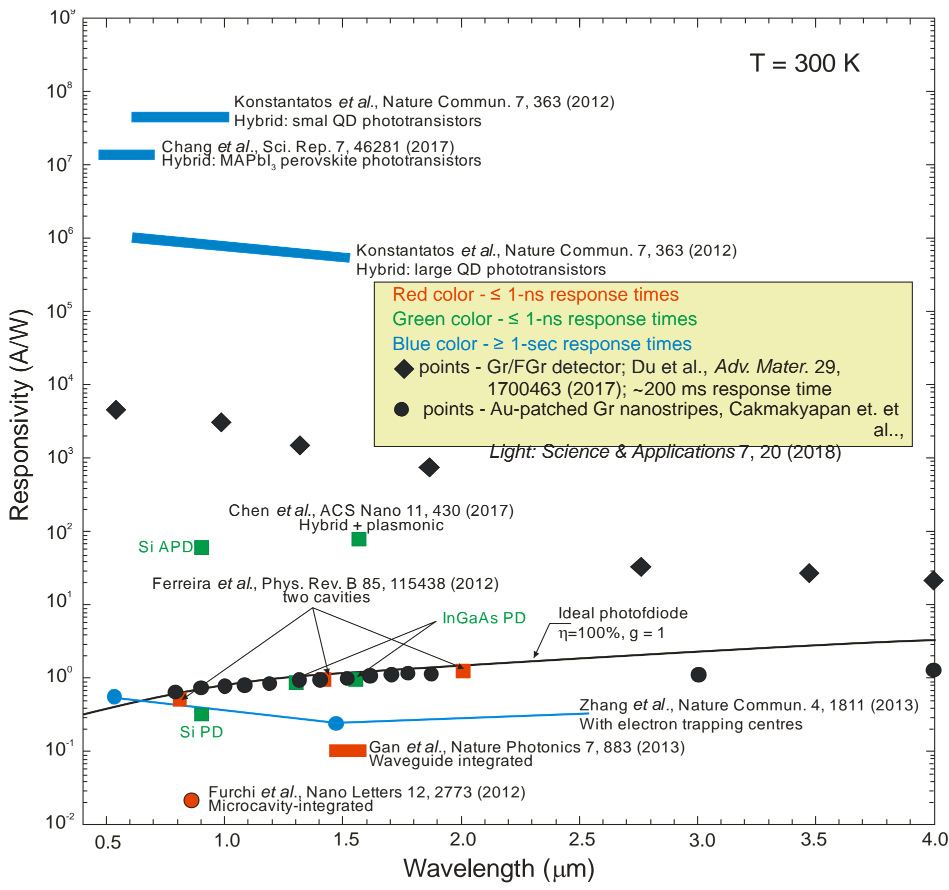

Fig. 44. Spectral responsivity of graphene photodetectors compared with commercial ones. Black line shows 100% quantum efficiency. Red and green colours denote ≤ 1 ns response times, while the blue colour denotes ≥ 1 s response times. The graphene photodetectors are labelled with their reference as well as a brief description of the photodetector style. The commercial photodiodes are shown in green [after Ref. 18].

It is interesting to underline the unique electrical and optical characteristics of gold patched graphene nanostripe photodetectors demonstrated by Cakmakyapan *et al.* [103]. Photodetector has an ultrabroad spectral response from the visible to the IR region with high responsivity levels ranging from 0.6 A/W at a wavelength of 800 nm to 11.65 A/W at 20 μm and operation speed exceeding 50 GHz. As is shown in Fig. 44, its current responsivity (black circles) coincides well with a curve (black line) theoretically predicted for an ideal photodiode in the NIR spectral range.

Similar to graphene-based photodetectors, ultrahigh responsivity and ultrashort time response cannot be obtained in practice in 2D related material photodetectors at the same time. 2D layered materials show potential in a photodetection covering UV, visible and IR ranges (see Fig. 45) [19]. Generally, however, most of them cover the

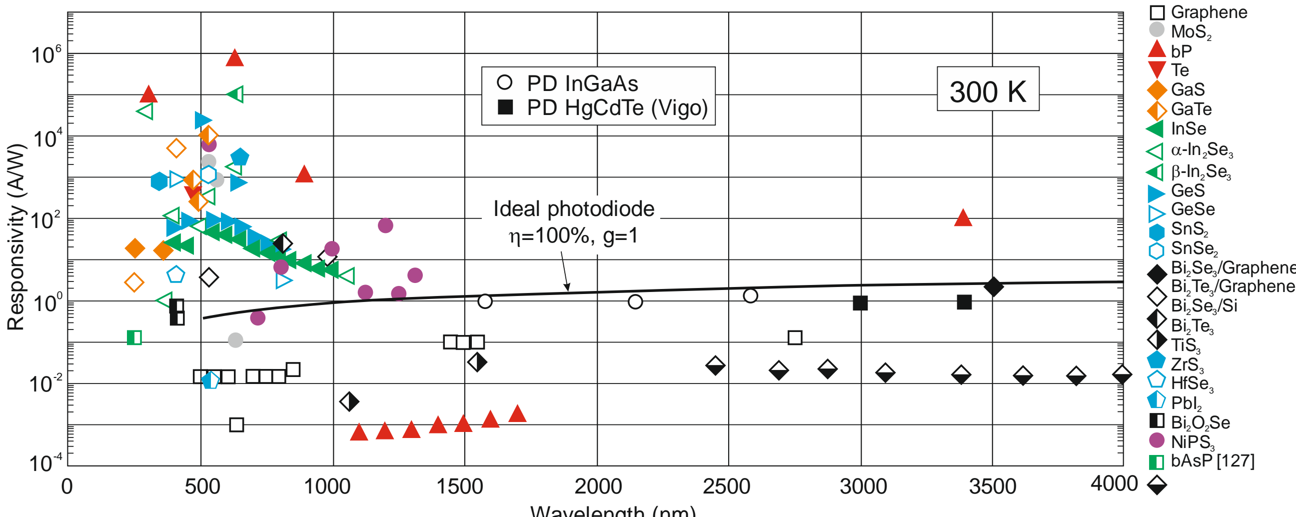

Fig. 45. Summary of spectral responsivities to the layered 2D material photodetectors at room temperature [after Refs. 33 and 127]. Black line shows spectral responsivity for an ideal photodiode with a 100% quantum efficiency and $g = 1$. For comparative goals, the responsivities of commercially available photodetectors (InGaAs and HgCdTe photodiodes) are marked.

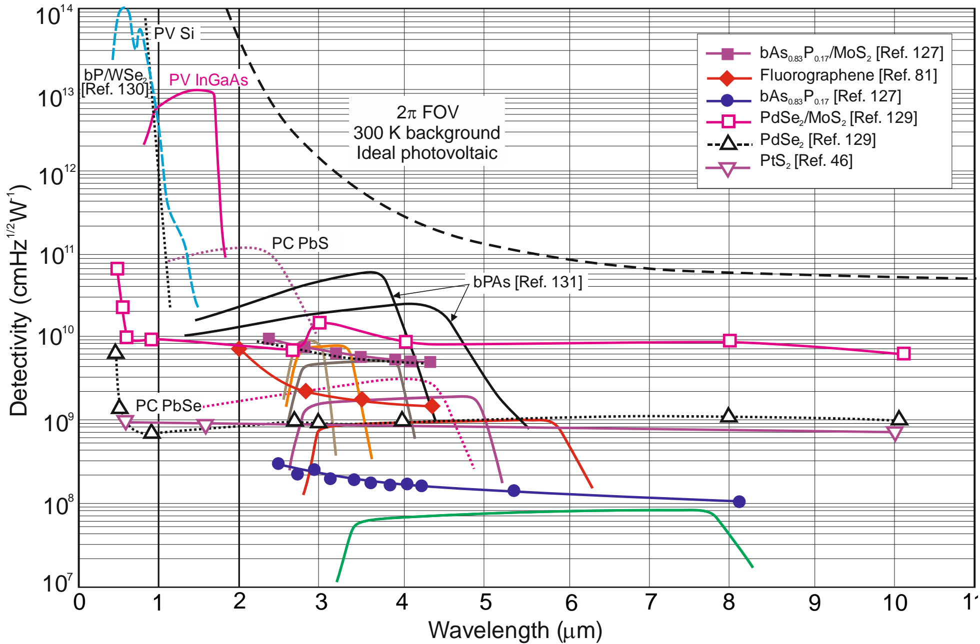

Fig. 46. Room-temperature spectral detectivity curves of the commercially available photodetectors [PV Si and InGaAs, PC PbS and PbSe, HgCdTe photodiodes (solid lines - Ref. 128)]. Also the experimental data for different types of 2D material photodetectors are included from literature as marked [46,81,127,129-131]. PC - photoconductor, PV - photodiode.

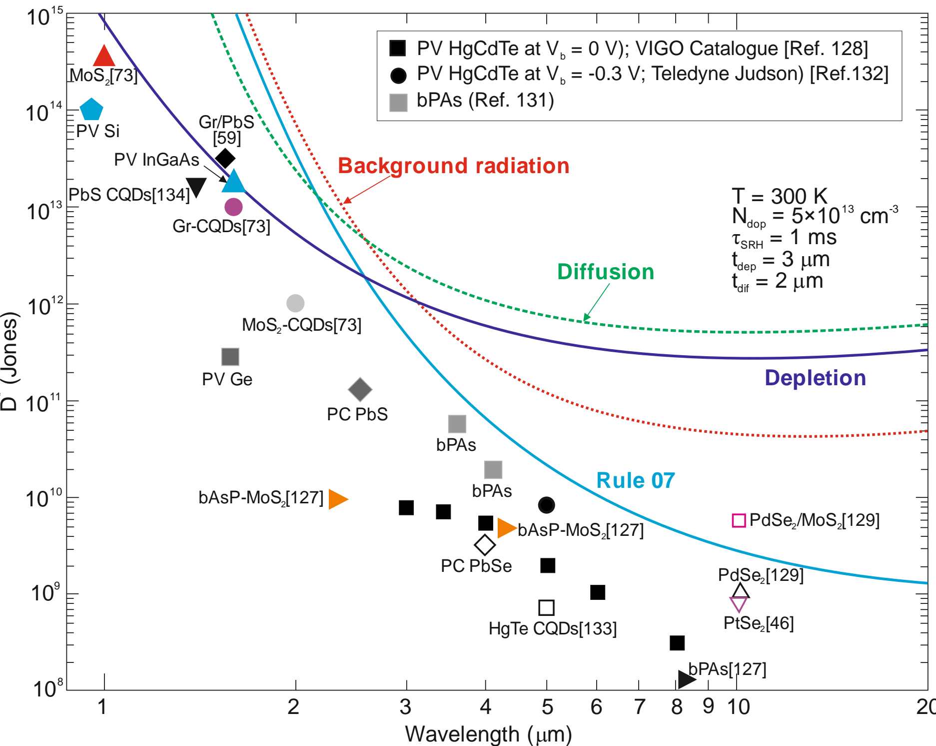

Fig. 47. Dependence of detectivity on a wavelength for the commercially available room-temperature operating infrared photodetectors (PV Si and Ge, PV InGaAs, PC PbS and PbSe, PV HgCdTe). There are also included experimental data for a different type of 2D material and colloidal quantum dot (CQD) photodetectors taken from literature as marked [46,59,73,127-129,131-134]. The theoretical curves are calculated for P-i-N HOT HgCdTe photodiodes assuming the value of τ_{SRH} = 1 ms, the absorber doping level of 5 × 10^{13} cm^{-3} and the thickness of active region t = 5 μm. PC - photoconductor, PV - photodiode.

visible and NIR spectral range, and only graphene-based, b-AsP alloys bismuthene (like Bi_2Te_3 and Bi_2Se_3), as well as noble transition metal dichalcogenides play the main role in the infrared region. In addition, as Figure 45 shows, the performance of graphene-based infrared photodetectors is inferior in comparison with alternative 2D material photodetectors.

At present, HgCdTe is the most widely used variable gap semiconductor for IR photodetectors, including uncooled operation, and stands reference for alternative technologies. Literature data for longer wavelength infrared graphene-based photodetectors, with a cut-off wavelength above 3 μm, are limited. Figures 46 and 47 compare their detectivities with commercially available

HgCdTe photodiodes operating at room temperature [128,132]. The upper detectivity of a Gr/FGr photodetector in the SWIR range is close to HgCdTe photodiodes. This figure also shows experimental data for bAsP photodetectors and noble transition metal dichalcogenides entering the second atmospheric transmission window.

As is shown, the detectivity values for selected 2D material photodetectors are closed to data presented for commercial detectors (PV Si and Ge, PV InGaAs, PC PbS and PbSe, PV HgCdTe), and in the case of black phosphorus and noble TMD detectors are even higher. The enhanced sensitivity of 2D material photodetectors is introduced by a bandgap engineering and photogating effect. However, the layered-material photodetectors are characterized by a limited linear dynamic range of operation and slow response time.

Figure 47 also compares the experimental detectivity values published in literature for different types of a single element 2D material photodetectors operated at room temperature with theoretically predicted curves for P-i-N high-operating temperature (HOT) HgCdTe photodiodes.

At present stage of the HgCdTe technology, the Rule 07 metric (specified in 2007 [135]) is not a proper approach for prediction of the HgCdTe detector and system performance and as a reference benchmark for alternative technologies. The Rule 07 coincides well with a theoretically predicted curve for an Auger-suppressed p-on-n photodiode with a doping concentration in the active region equal to $N_d = 10^{15}$ cm^{-3}. For a sufficiently long Shockley-Read-Hall (SRH) carrier lifetime in a HgCdTe ternary alloy, what is experimentally supported at doping level below 5×10^{13} cm^{-3}, the internal P-i-N HgCdTe photodiode current is suppressed and its performance is limited by the background radiation [136]. In *Extended Abstracts* of *The 2019 U.S. Workshop on the Physics and Chemistry of II-VI Materials* [137] it is proposed to replace Rule 07 with Law 19. The Law 19 corresponds exactly to the background limited curve for room temperature. The internal photodiode current can be several orders of magnitude below Rule 07 in dependence on a specific cut-off wavelength and operating temperature. In this context the alternative technologies should be considered and evaluated. Figure 47 shows that the potential properties of HOT HgCdTe photodiodes operated in a longer wavelength infrared range (above 3 µm) guarantee achieving more than order of magnitude higher detectivity (above 10^{10} Jones) in comparison with the value predicted by Rule 07. The above estimations provide a further encouragement for achieving low-cost and high performance MWIR and LWIR HgCdTe FPAs operated in HOT conditions.

Particular attention in a development of THz imaging systems is devoted to the fabrication of sensors with a large potential for a real-time imaging while maintaining a high dynamic range and room temperature operation. CMOS process technology is especially attractive due to their low price for industrial, surveillance, scientific, and medical applications. With that in mind, much of a recent development is directed towards three types of FPAs [18]:

- Schottky barrier diodes (SBDs) compatible with the CMOS process,
- FETs relying on plasmonic rectification effect, and adaptation of IR bolometers to the THz frequency range.

Comparing these two detector types, FETs provide some benefits in the THz frequency range, such as inherent scalability, and a combination of fast response and high frequency operation. In the case of SBDs, their efficiency is strongly influenced by parasitic capacities, which usually causes a dramatic decrease in sensitivity above 1 THz.

SBDs respond to the THz electric field and usually generate an output current or voltage through a quadratic term in their current-voltage characteristics. In general, the *NEP* of SBD and FET detectors is better than that of Golay cells and pyroelectric detectors around 300 GHz. Both the pyroelectric and the bolometer FPAs with detector response times in the millisecond range are not suitable for a heterodyne operation. FET detectors are clearly capable of a heterodyne detection with improved sensitivity. Diffraction aspects predicts FPAs for higher frequencies (0.5 THz and above) and in conjunction with large *f/#* optics [18].

Due to a high carrier mobility, graphene is a very promising material for development of high-performance room temperature detectors covering the full THz range (0.1-10 THz). At present stage of technology, the most effective graphene THz detectors employ the plasma rectification effect in FETs, where plasma wave in the channel is excited by an incoming THz wave modulating the potential difference between gate and source/drain and being rectified via non-linear coupling and transfer characteristics in FET [18]. Next, two figures compare *NEP* values of graphene-based FET room temperature detectors with existing THz photon detectors (Fig. 48) and thermal detectors (Fig. 49) dominating on the market [18]. The experimental data are gathered from the world-wide literature.

Most experimental data gathered in literature is given for single graphene detectors operating above a wavelength of 100 µm (frequency range below 3 THz). Generally, the performance of graphene FET detectors is lower in comparison with CMOS-based and plasma detectors fabricated using silicon, SiGe, and InGaAs-based materials. However, in comparison with VO_x and amorphous silicon microbolometers, the performance of graphene detectors is close to the trend line estimated for microbolometers in a THz spectral region (see Fig. 49). The best quality VO_x bolometer arrays are characterized by *NEP* value of about 1 pW/Hz$^{1/2}$ in the LWIR range (≈ 10 µm). It should be marked here however, that microbolometer data are addressed to monolithic arrays. In this case an important issue for FPA is pixel uniformity. It appears, that the fabrication of monolithically integrated THz detector arrays encounters many technological problems that the device-to-device performance variations and even the percentage of non-functional detectors per chip tend to be unacceptably high [18]. Adaptation of IR microbolometers to the THz frequency range after the successful demonstration of active THz imaging [138] entailed that in the period of 2010-2011, three different companies/organizations announced cameras optimized for the THz frequency range: NEC (Japan) [139], INO

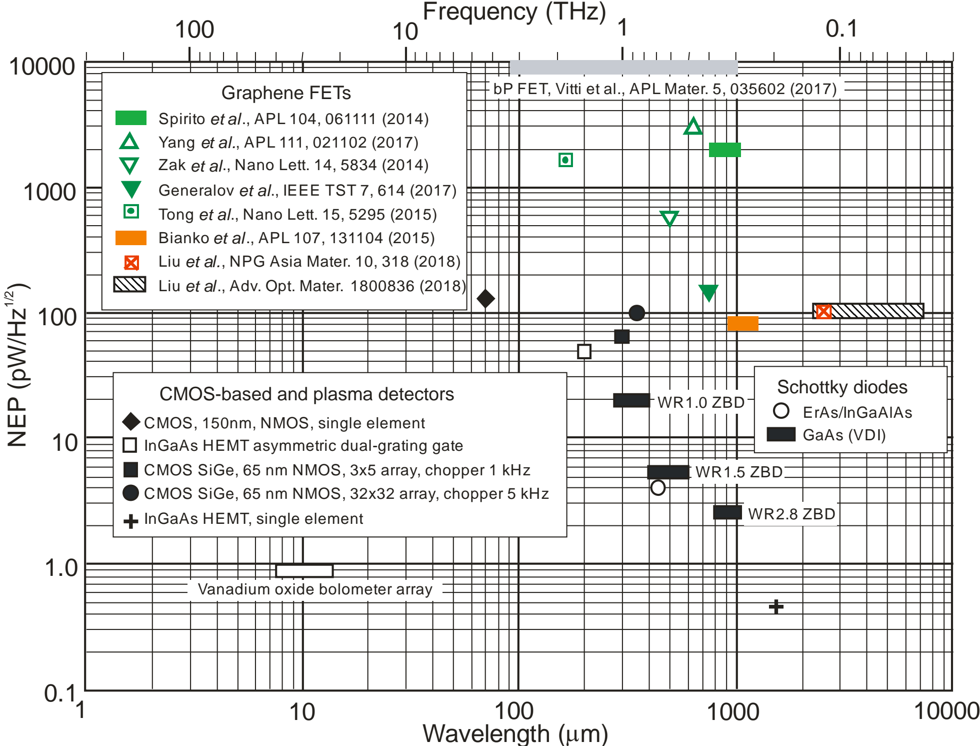

Fig. 48. *NEP* spectral dependence for graphene FET detectors and different photon THz (CMOS-based, Schottky diodes) [after Ref. 18].

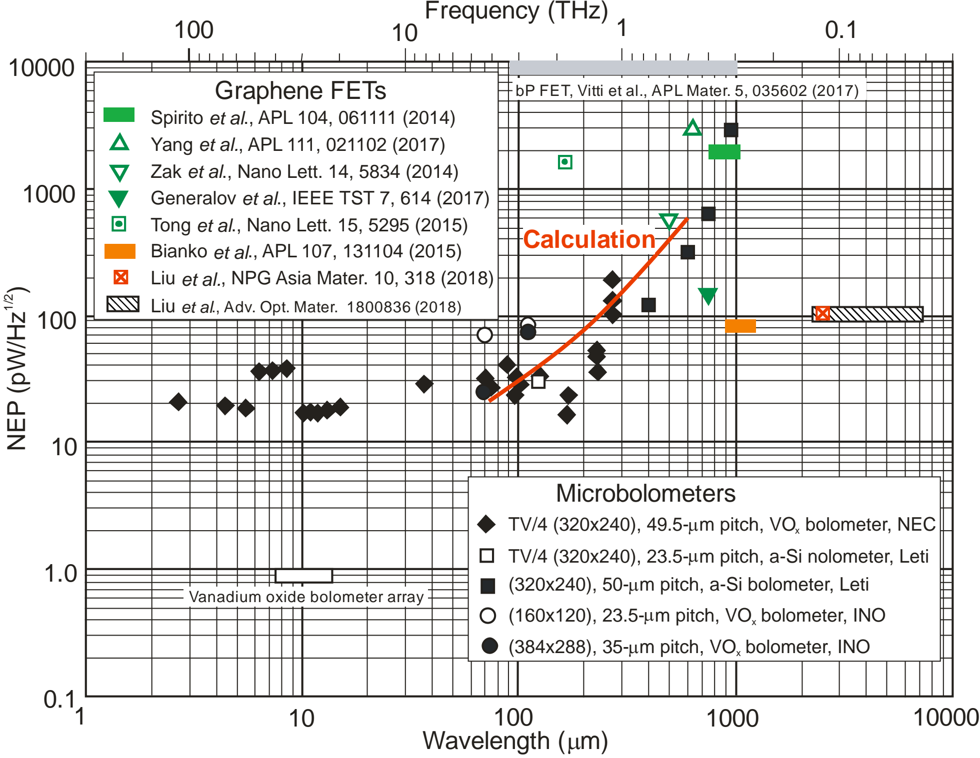

Fig. 49. NEP spectral dependence for graphene FET detectors and microbolometer THz FPAs [after Ref. 18].

(Canada) [140] and Leti (France) [141]. Figure 49 summarizes the *NEP* values for bolometer FPAs fabricated by three vendors. The FPAs optimized for 2-5 THz exhibit impressive *NEP* values below 100 pW/Hz$^{1/2}$. It can be seen, that the wavelength dependence of *NEP* is quite flat below 200 µm. Further improvement of performance is possible by increasing number of pixels, modification of antenna design while preserving pixel pitch, ROIC, and technological stack.

For FPAs the relevant figure of merit for determining the ultimate performance is not the detectivity, D^*, but the noise equivalent difference temperature (*NEDT*) and the modulation transfer function (*MTF*) [58]. *NEDT*, as well as *MTF* are the primary performance metrics to thermal

imaging systems: thermal sensitivity and spatial resolution. Thermal sensitivity is concerned with the minimum temperature difference that can be discerned above the noise level. *MTF* concerns the spatial resolution and answers to the question – how small an object can be imaged by the system?

In 2013, the European Union launched the Future and Emerging Technology Graphene Flagship program to accelerate research into technologies based on graphene and related materials. Recently, within the framework of this program, the hybrid GQD photodetector arrays fully vertically integrated into a CMOS readout chip have been demonstrated (see Fig. 50). These 388 × 288 pixel cameras are operated in the UV-visible-SWIR range from 300 to 2000 nm. Pixels of the image sensor (see Table 3, first line) are characterized by a high gain of 10^7 and a responsivity above 10^7 A/W. The size of pixels is large (20 μm, what limits spatial resolution) for operation in the visible and SWIR range in comparison with present commercial CMOS images operated in the visible region with a pixel size close to 1 μm [1]. Also, operability of the arrays estimated as 95% is poor [142]. The fixed pattern noise (spatial noise) has a strong influence on the noise equivalent irradiance of the arrays, especially if the array pixels are hybrid (like GQDs). It is well known that nonuniformity of QDs limits performance of QD photodetector arrays [143].

From the above discussion about the present status of single graphene-based detectors, we can conclude that [18]:

- pristine graphene has a broadband absorption and fast response dominated by hot-carriers dynamic; in consequence due to a low absorption coefficient and a fast relaxation time, its responsivity is lower in comparison with detectors existing on global market, especially HgCdTe, InGaAs, and microbolometers,
- improving the responsivity by combining graphene with other materials (hybrid photodetectors) owing to the photogating effect causes the limited linear dynamic range due to the charge relaxation time, leading to drop in sensitivity with incident optical power,
- responsivity of hybrid and chemically function-nalized graphene detectors is comparable and even better in comparison with commercially available detectors, however, considerable drop in operating speed (bandwidth) is observed; generally, their response time (millisecond range and longer) is three order of magnitude longer in comparison with commercial detectors (microsecond range and shorter); above drawbacks limit their practical applications,
- at present stage of technology, the most effective graphene-based photodetectors are THz detectors which use plasma rectification phenomena in FETs; performance of these detectors approximate that of commercial detectors,
- due to the poor graphene-based detector technology, development of arrays is in the infancy stage (especially very low operability and uniformity).

Considering fundamental material properties and seeing on the present stage of graphene technology, it is rather doubtful to predict a stronger position of graphene in the future imaging infrared systems. The assumptions that graphene is always a perfect 2D crystal in isolation from its environment is, in most cases, not valid. There are significant challenges faced by materials scientists to improve graphene growth techniques [18].

Graphene-based detector challenges include limited linear dynamic range of operation, lack of efficient generation, and extraction of photoexcited charges, smearing of photoactive junctions due to hot-carrier effects, large-scale fabrication, and, ultimately, environmental stability of the constituent materials [18].

As is shown in Ref. 144, the ratio of the absorption coefficient to the thermal generation rates, α/G, is the main figure of merit of any IR materials where the thermal generation rate is inversely proportional to the recombination lifetime. Due to ultrahigh mobility, it is suitable for high-speed communications. However, it remains a great challenge to reach high responsivity in

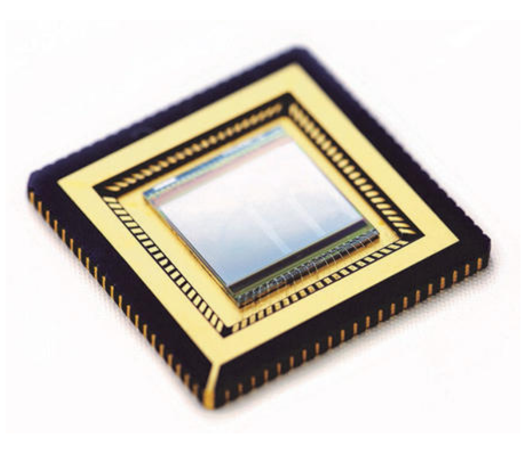
(a)

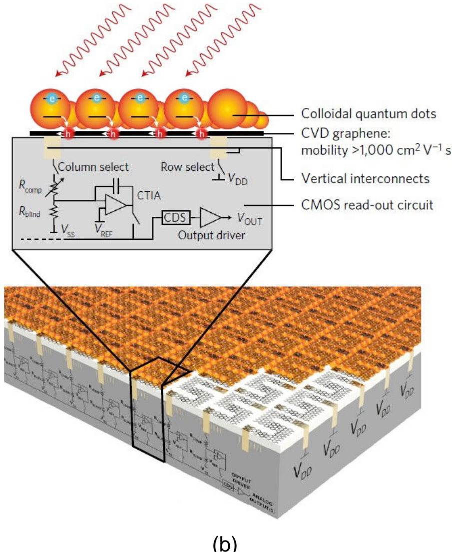

(b)

Fig. 50. Monolithically integrated graphene-quantum dot photodetector array (a) and side view of detector, and the underlying readout circuit (b) [after Ref. 142].

graphene detectors because of a weak optical absorption (only 2.3% in the monolayer graphene sheet) and a short carrier lifetime (< 1 ps). In other words, the applications of graphene-based photodetectors are limited in comparison to traditionally detectors. Various approaches have been proposed to enhance sensitivity by introduction of a bandgap, electron trap layers (quantum dot structures), or nanoribbons. However, these methods degrade the electronic performance including carrier mobility.

4. Related 2D material detectors

Graphene is one of a large number of possible 2D crystals. Discovery of new 2D materials with direct energy gaps in the IR to the visible spectral regions has opened up a new perspective for a photodetector fabrication. There are hundreds of layered materials that retain their stability down to constituent monolayers and whose properties are complementary to those of graphene and are treated in many review papers; see, e.g., Refs. 10, 12, 32, 33, 35, 59, 62, and 110.

4.1. General overview

Similar for graphene-based detectors, radiation detection mechanisms such as photoconductive, photovoltaic, photo-thermoelectric, and FET effects have also been reported in other 2D material photodetectors. For example, Figure 51 shows two types of detectors: $MoSe_2$ photoconductor and bP-based FET. While 2D TMDs are limited to UV-NIR due to their bandgaps, bP can be tuned to below 0.3 eV by doping with As. b-AsP has been demonstrated for light detection from UV to THz.

Despite the very high responsivity reported in hybrid garphene-based phototransistors, their power consumption, electronic readout circuits, and noise are all determined by zero bandgap of graphene which leads to a large dark current. Alternative 2D materials, especially TMDs, have been considered as a potential replacement of graphene for transistor channels. The use of 2D TMDs channels with a bandgap of 1-2 eV is a particular promise offering a lower leakage current during the transistor operation in the depletion mode.

Ultrahigh responsivity and ultrashort time response cannot be obtained at the same time in practice 2D related materials, as with the graphene-based photodetectors. In 2D materials and their hybrid systems, the photogating effect can be realized in two ways as is described in section 3.1.2; by carriers trapping in the localized states or (in hybrid photodetectors) by carriers trapping and transferring one type of carriers to 2D materials.

In layered detectors, the shot noise generated from the dark current is considered as the main factor limiting detectivity. In the case of room temperature photodetectors in which a photogain is observed, thermal noise and generation-recombination (g-r) noise should be considered. For various 2D photodetectors, also the low-frequency noise (1/*f*) should be investigated because it is considered as an important metric for evaluating the performance [18].

Exemplary performance of infrared photodetectors based on 2D materials and their hybrid structures, including photodetectors with a cut-off wavelength above 1 µm, are gathered in Table 6. It was demonstrated also that topological insulators can be promising candidate materials for a broadband photodetection. Metallic surface state can bring a strong optical absorption, what has been demonstrated for a Bi_2Te_3/Si heterojunction. The spectral responsivity of this device covers a broadband response from 370.6 nm to 118 µm [145].

Figure 52 compares the spectral responsivity and detectivity of representative 2D material photodetectors in the SWIR spectral range (with the cut-off wavelength range below 3 µm) with silicon and InGaAs photodiodes operated at room temperature [18]. Generally, the responsivity and detectivity of 2D material photodetectors are lower in comparison with the most popular commercial InGaAs.

4.2. Middle and long wavelength infrared detectors

In the spectral region above 3 µm, among the TMDs such materials as bP, b-AsP alloys, and layered semiconductors with narrow bandgaps and a high carrier mobility are of a great importance for the implementation of high-performance infrared detectors (see Table 6).

4.2.1. Black phosphorus photodetectors

Attention to 2D bP was brought from 2014 as is described in section 2.2.2. b-AsP as a monolayer or a few-layer material has been shown its attractive properties, such as high mobility, anisotropic optical properties, and a highly tuneable thickness-dependent direct bandgap, spanning from 0.3 eV in the bulk case to 1.7 eV of the monolayer case. In this context bP appears as a natural trade-off between graphene and TMDs.

The first paper of great significance which recovered the potency of bP for practical infrared applications was published by Guo *et al.* in 2016 [146]. Authors of this paper

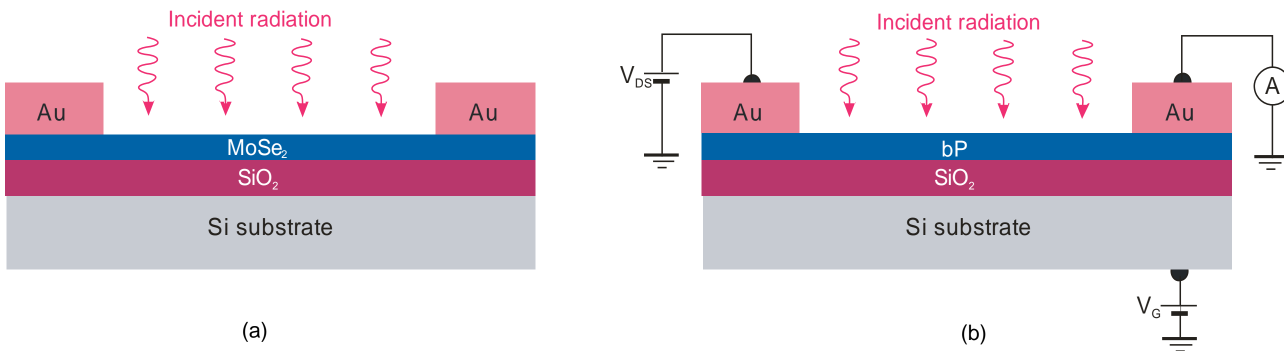

Fig. 51. Cross-section view of 2D material photodetectors: (a) $MoSe_2$ photoconductor and (b) bP-based FET [after Ref. 18].

Table 6
Infrared photoresponsivity of 2D materials at room temperature.

Materials	Wavelength (μm)	Responsivity (A/W)	Bias (V)	Gain (%)	Time	Peak detectivity (Jones)	Ref.
MoS_2	0.5-1.1	0.1	-10	25%	< 15 ms		33
WS_2 (CVD)	0.5-0.9	3.5×10^5	2	1×10^5	23 ms	10^{14}	33
In_2Se_3	0.4-0.94	9.8×10^4	0.05		9 s	3.3×10^{13}	33
GeAs	1.6	6			3 s		33
MoS_2/PbS	0.4-1.5	6×10^5	1		0.35 s	7×10^{14}	33
MoS_2/Si	0.4-1.0	0.9082	-2		56 ns; 825 ns	1.889×10^{13}	33
MoS_2/bP	0.5-1.6	22.3	3	50	15 μs; 70 μs	3.1×10^{13}	33
MoS_2/G/WS_2	0.4-2.4	1×10^4	1	10^6	53.6 μs; 30.3 μs	1×10^{15}	33
bP (gated-photocon.)	3.5	10	0.5	270		6×10^{10}	131
bP/MoS_2 (p-n hetero)	4.3		0.5		~ 1ms	2×10^9	127
bAsP (phototransitor)	2-8	$(30\text{-}10)\times10^{-3}$	0			3×10^8	127
$PtSe_2$ (phototransitor)	0.6-10	4.5			1.1, 1.2 ms	7×10^8	46
$PdSe_2$ (phototransitor)	1-10.6	~ 45	1	10^3-49	74.5, 93.1 ms	1×10^9	129
$PdSe_2$/MoS_2 (p-n hetero)	1-10.6	~ 4	1		65.3, 62.4 μs	8×10^9	129
Gr/Ti_2O_3	10	300	0.1		1.2, 2.6 ms	7×10^8	80
Bi_2Te_3/Si	UV-THz	1	-5		0.1 s	2.5×10^{11} (635 nm)	145

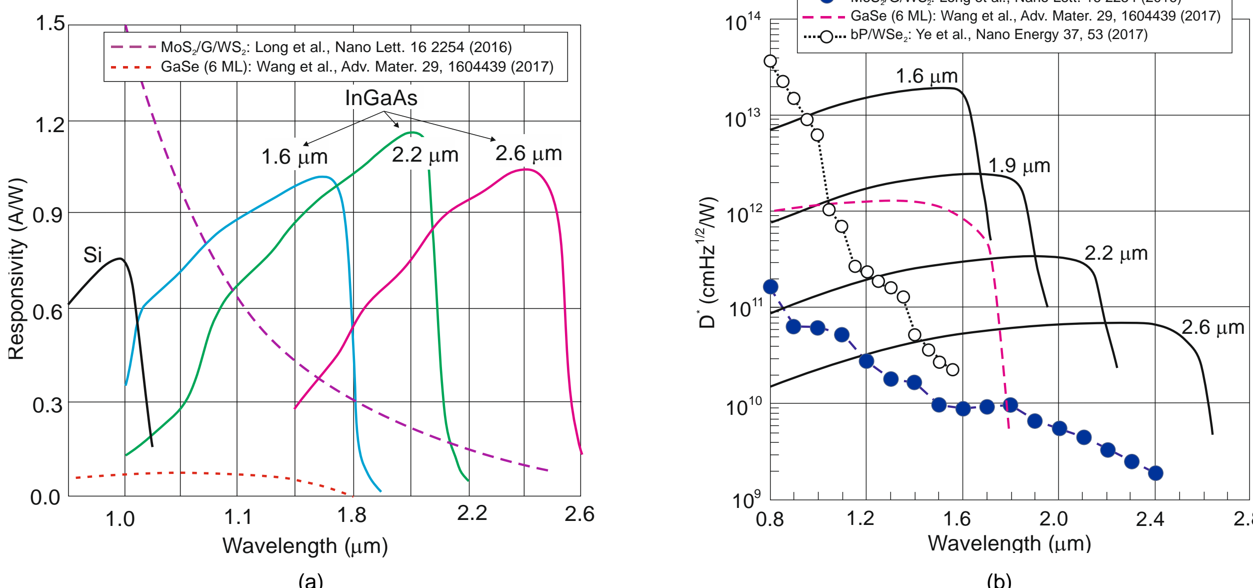

Fig. 52. Comparison of spectral responsivity (a) and detectivity (b) of 2D material photodetectors in the SWIR spectral range with silicon and InGaAs photodiodes operated at room temperature [after Ref. 18].

achieved a bP photoconductor with a room temperature responsivity of 82 A/W at a wavelength of 3.39 μm. This high responsivity is attributed to the photogating effect and the shallow long trap level-induced carrier lifetime. Usually, high gain limits the bandwidth. For a light chopping frequency over 10 kHz, the responsivity value of 60 mA/W results from the intrinsic photovoltaic effect.

Bullock *et al.* [147] have demonstrated 2D bP/MoS_2 MWIR heterojunction photodiodes (see Fig 53) achieving room-temperature external quantum efficiencies of 35% and detectivities as high as 1.1×10^{10} $cmHz^{1/2}/W$ at $\lambda = 3.8$ μm. This value is similar to the current state of-the-art room-temperature photodiodes commercially available (see Fig. 46). Furthermore, by leveraging the anisotropic optical properties of bP, the first bias-selectable polarization-resolved photodetector has been demonstrated.

In the bP/MoS_2 heterojunction photodiode, a thin (~ 10-20 nm) n-type MoS_2 layer acts as an electron contact and

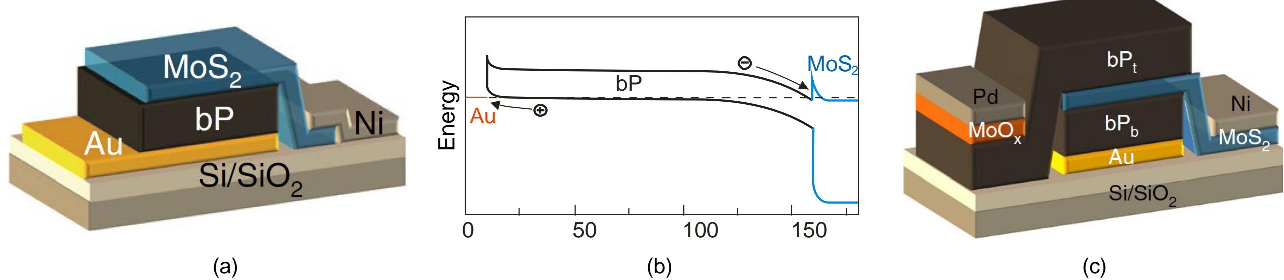

Fig. 53. Two-terminal bP/MoS_2 MWIR heterojunction photodiodes: (a) schematic of a device configuration, (b) energy band diagram of the device (a) under equilibrium, and (c) schematic of polarization-resolved bP/MoS_2 heterojunction photodiode [after Ref. 147].

also constitutes a window for the MWIR radiation. A back reflector Au pad is a contact for holes. As is shown in the band diagram [see Fig. 53(b)], the band offset at the MoS_2 and bP heterojunction allows the flow of electrons to the MoS_2 contact and blocks the flow of holes.

The polarized-resolved device uses two bP/MoS_2 heterojunctions with orthogonal bP crystal orientations separated by a common MoS_2 electron contact. Each bP layer has an isolated hole contact. This configuration is similar to the two-colour back-to-back photodiodes that have been previously demonstrated in two-colour HgCdTe and III-V semiconductor photodiodes [58]. The top MoO_x/Pd stack is an effective hole contact because of its large work function.

By varying the composition of arsenic, x, in the As_xP_{1-x}, the band gap correspondingly changes from 0.3 to 0.15 eV. This change in the energy gap suggests that b-AsP may interact with light whose wavelength is as long as 8.3 µm. Long *et al.* [127] have reported about $bAs_{0.83}P_{0.17}$ long-wavelength IR photodetectors, with a room temperature operation to 8.2 µm. The design of a phototransistor is similar to the one shown in Fig. 51(b). The b-AsP thin film flakes of b-AsP ranging from 5 to 20 nm thick were mechanically exfoliated from bulk b-AsP samples onto a highly doped silicon substrate covered by a 300-nm SiO_2 in a glove box. After device fabrication by a standard electron-beam lithography, metallization, and a lift-off process, the spin-coated thin layer of polymethyl methacrylate (PMMA) was deposited to protect the samples from oxidation in the air.

Figure 54 schematically shows the operation principle of b-AsP devices with a different doping type. If the channel is p-type doped, the electron-hole pair is mainly generated at the reverse-biased b-AsP/drain junction. In the case of a slightly n-type doped channel, the photo-generation takes place at the reverse-biased b-AsP/source junction. Photogenerated electron-hole pairs are separated by the electric field. Due to the opposite junction bias direction, the photocurrent has an opposite polarity at two contacts. Detailed studies of a photoresponse mechanism revealed a more complex phenomenon with contribution of the photogating and PFE effects. The photocurrent is a negative relative to V_{ds} and shows a very weak gate dependence in the highly doped regime with a dominant contribution of PTE and bolometric effects.

Well known strategy to suppress dark current is using heterojunctions; in the considered case using 2D vdW heterojunctions. Integrability is an inherent merit of 2D materials by which different 2D flakes can be sequentially stacked into vdW heterojunctions. Following this idea, Long *et al.* [127] fabricated photodetectors based on a b-AsP/MoS_2 heterostructure with a room-temperature detectivity of about 5×10^9 cmHz$^{1/2}$/W at 4.3 µm. Spectral detectivity curves of two types of $bAs_{0.83}P_{0.17}$ photodetectors (phototransistor and vdW heterojunction) comparable with commercially available ones are compared in Fig. 46. More recently, Tan *et al.* [148] have demonstrated that doping bP with carbon to form a black phosphorus-carbon (bPC) can extend the detectable wavelength to 8 µm and a peak responsivity of 2163 A/W was achieved from a bPC-based phototransistor at 2 µm.

Amani *et al.* [131] studied the response spectrum and responsivity of bP and b-AsP alloys (composition range 0-91% of As) as the active regions of phototransistors.

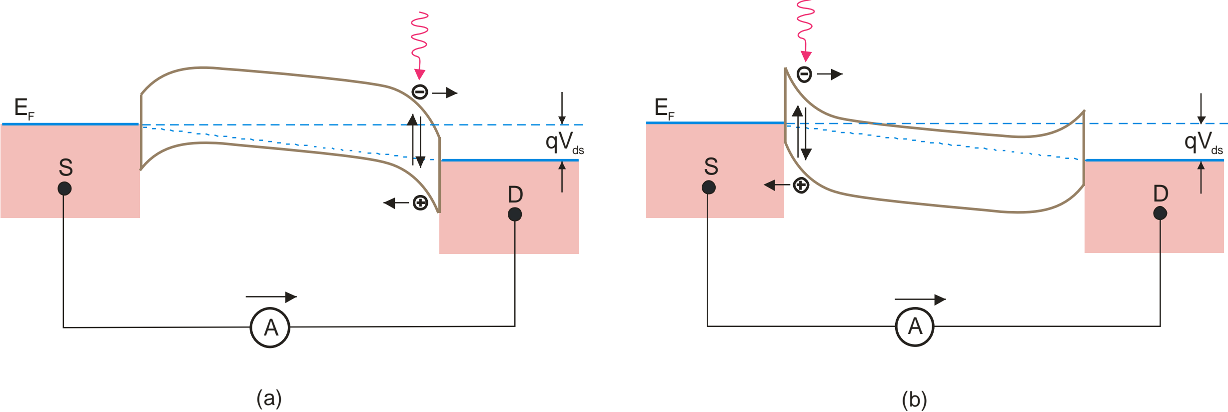

Fig. 54. Schematic diagrams of an energy band structure for an MWIR b-AsP photovoltaic detector at different doping types under the bias voltage V_{ds}: (a) the sample of b-AsP working at the p-type region and (b) the device working at the n-type region. The black horizontal arrows indicate the direction of the photocurrent [after Ref. 127].

Figure 46 shows spectral dependence of detectivity for b-AsP gated photoconductors (phototransistor) with the cut-off wavelength tuned from 3.9 µm to 4.6 µm. It is shown that for optimized devices with a thickness of ~ 28 nm, the peak detectivity is of 6×10^{10} cmHz$^{1/2}$/W for bP and 2.4×10^{10} cmHz$^{1/2}$/W for $bP_{0.91}As_{0.09}$ at room temperature with a bandwidth of 117 kHz [131]. This detectivity is a record achievement for b-AsP 2D material photodetectors in the MWIR spectral range which is almost one order of magnitude greater than commercially available HgCdTe photodiodes.

In Fig. 55 are compared peak detectivity of HgCdTe photodiodes [128] and InAs/GaSb type-II superlattice (T2SL) interband quantum cascade infrared photodetectors (IB QCIP) [149] operating at room temperature with b-AsP and noble metal dichalcogenide photodetectors. We can see that in the MWIR spectral range the performance of b-AsP detectors outperforms commercially available uncooled HgCdTe photodiodes, instead in LWIR the detectivity of noble transition metal dichalcogenide photodetectors is the best. Due to a strong covalent bonding of III-V semiconductors, IB QCIPs can be operated at a temperature up to 400°C, what is not possible to achieve for a HgCdTe counterpart and especially b-AsP due to its fatal problem of a structural instability. Also, response time of HgCdTe IB QCIPs detectors operated at room temperature, typically in the order of nanoseconds, is considerably shorter in comparison with b-AsP photodetectors [18].

4.2.2. *Noble transition metal dichalcogenide photodetectors*

Narrow-bandgap 2D noble metal dichalcogenides could be a novel platform for room temperature LWIR photodetectors. Theoretical simulations predict that group X TMDs (Ni, Pd, Pt) are the promising narrow bandgap semiconductors with ~ 0-0.25 eV [39,46,47,150]. The room-temperature mobility of bulk materials is greater than 1000 cm^2/Vs. For 2D materials, the carrier mobility larger than 200 cm^2/Vs and air-stable properties have been demonstrated in recent years [150,151].

The first few-layered PtS_2 phototransistor on an hBN substrate operating in the visible range was demonstrated in 2017 [152]. A high photoresponsivity up to 1.56×10^3 A/W and an ultrahigh photogain of 2×10^6 were achieved benefiting from the short channel and hole trap states. Yu *et al.* reported an Ar-plasmon-treated bilayer $PtSe_2$ with a responsivity and response time of 4.5 A/W and 1 ms at a wavelength of 10 µm [46]. The detectivity approaches 7×10^8 cm Hz$^{1/2}$/W which is higher than that of commercial bolometers operated in this wavelength range.

bP photodetectors are challenging because of their instability in the air. As an alternative, investigations of air-stable group X TMD materials for long wavelength infrared (LWIR) applications have been just started. New step in their development has been provided by Long *et al.* in the recently published paper [129]. This paper is dedicated to two types of $PdSe_2$ photodetectors based on the phototransistor and its heterostructure.

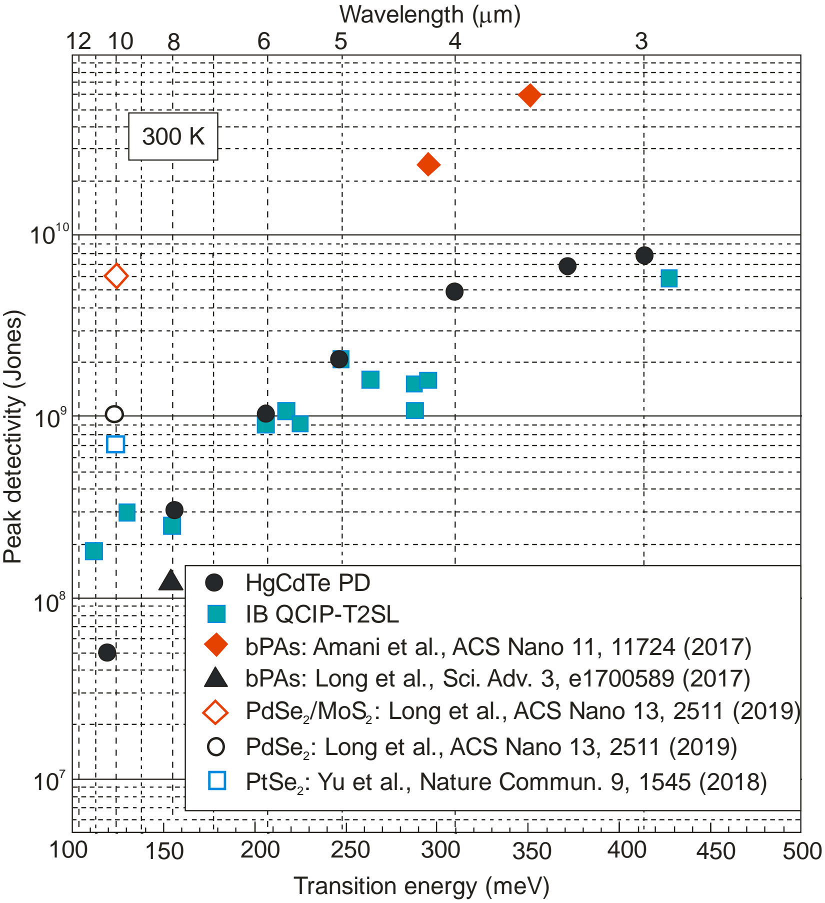

Fig. 55. Peak detectivity comparison between HgCdTe photodiodes, InAs/GaSb type-II superlattice IB QCIPs and representative 2D material photodetectors operated at room temperatures. Experimental data for HgCdTe photodiodes is taken according to VIGO catalogue [128]. Data for cascade infrared detectors are taken from many papers including Ref. 149.

$PdSe_2$ FETs were fabricated by a conventional electron-beam lithography process using flakes with a thickness of 5-20 nm to assure a high carrier mobility and a relatively high absorption. Figure 56 shows the long wavelength infrared photoresponse characteristics of a typical $PdSe_2$ phototransistor at room temperature. The responsivity decreases from 42.1 to 13.8 A/W at V_{ds} = 1 V under a laser illumination of 10.6 µm when the light power is increased from 1.42 to 5.67 nW. The photogating effect plays a crucial role in a high photoconductive gain due to the long lifetime of a combination induced by trap states and a short carrier transit time. As is shown, it decreases from 49 to 16 as the illumination power increases. This effect is especially emphasized, if we compare responsivities of HgCdTe photodiodes, where $g = 1$, with these for $PdSe_2$ phototransistors - see Fig. 56(b). In the last case, the responsivity is about one order of magnitude higher in the wide infrared spectral range. The photoresponse speed, one of the most important figures of merit, is rather slow. The rise/delay time defined as the time required to transition from 10/90% of the stable photocurrent during the illumination on/off cycle, is of 74.5 ms/93.1 ms under 10.6 µm laser illumination. The response time under a shorter light wavelength is much faster, about two orders of magnitude.

To decrease dark current density, usually a heterojunction device is used. The p-n heterojunction could be fabricated by stacking a p-type $PdSe_2$ with other n-type 2D material. Long *et al*. [129] have chosen n-type MoS_2 deposited on p-type $PdSe_2$ to form a vdW heterojunction. A schematic structure of this device is shown in Fig. 57(a). Standard electron-beam evaporation was used for fabricating metals electrodes (5 nm Ti and 50 nm Au).

Figure 57(b) shows a satisfactory device rectification effect of the output curve under dark conditions. The rectification ratio is typically of about 100 at 2 V bias which indicates that a built-in electrical field exists at the interface. This is characterized by a broadband

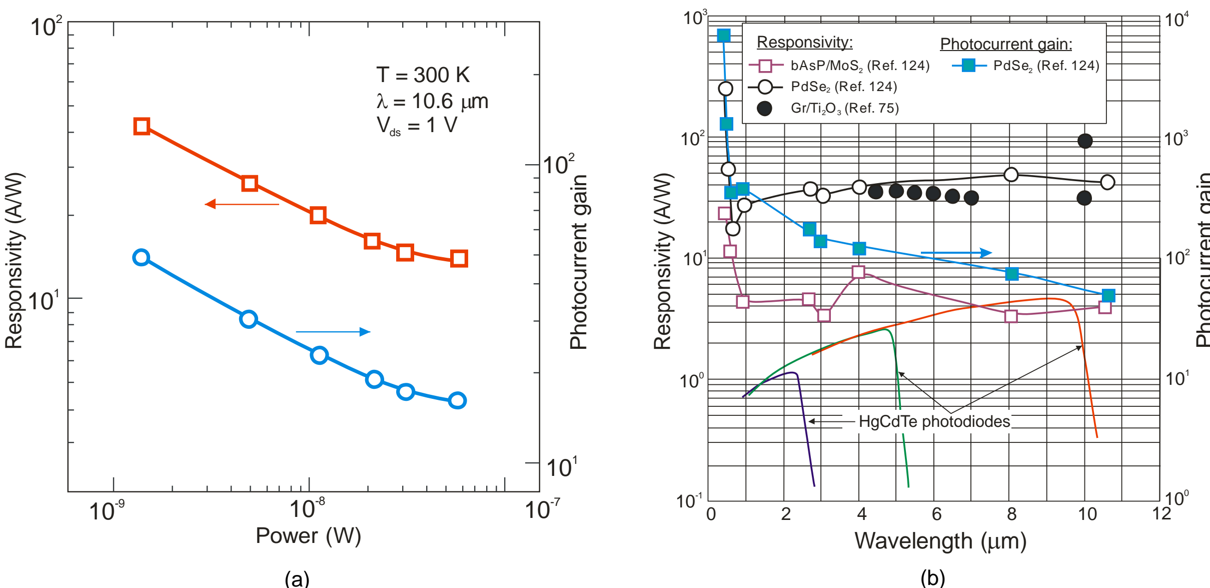

Fig. 56. Long wavelength infrared photoresponse of a typical $PdSe_2$ phototransistor at room temperature: (a) power dependence responsivity and gain at V_{ds} = 1 V, (b) responsivity and photocurrent gain as a function of a wavelength at 1 V bias voltage [after Ref. 129].

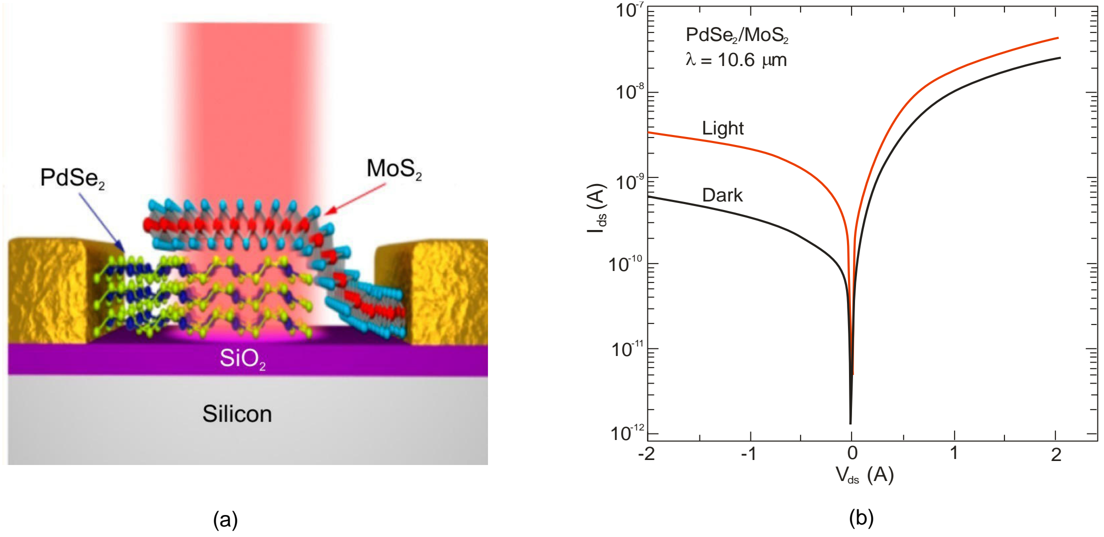

Fig. 57. $PdSe_2/MoS_2$ heterostructure device: (a) schematic structure of the heterojunction, (b) $I_{ds}(V_{ds})$ dark and illumination characteristics at room temperature [after Ref. 129].

photoresponse from 450 nm to 10.6 μm what is shown in Fig. 56(b). In the spectral range between 1 and 10.6 μm, the responsivity becomes stable at ~ 4 A/W.

The current noise of the $PdSe_2/MoS_2$ heterostructure is a significantly depressed relative to that of the $PdSe_2$ FET. At the low-frequency range, 1/*f* noise dominates the noise current contribution. It is well known that the low frequency flicker noise originates from the fluctuation of carriers being trapped and de-trapped by defects and disorder and exists widely in 2D materials [153]. If the frequency increases beyond 1 kHz, the noise current of the $PdSe_2/MoS_2$ heterostructure decreases to the Johnson noise level, while for the $PdSe_2$ FET devices, the current noise is 3 orders of magnitude higher than the Johnson noise level. This result indicates that the built-in electric field at the heterojunction effectively depresses the noise level and is highly desired. In consequence, in spite of a higher responsivity of $PdSe_2$ FET in comparison with the heterostructure [see Fig. 56(b)], the detectivity of the $PdSe_2/MoS_2$ heterojunction is higher - 8×10^9 cmHz$^{1/2}$/W at $\lambda = 10.6$ μm and $T = 300$ K - see Figs. 46 and 55. This is a record achievement because this value of detectivity is even more than one order of magnitude larger than that of commercial HgCdTe photodiodes.

4.3. Terahertz detectors

Diverse optoelectronic properties of 2D materials cover the wide range of the electromagnetic spectrum. Recently, efforts have increased in developing a proof-of-concept, also THz photodetectors. bP with a finite and direct bandgap in both bulk ($E_g \approx 0.35$ eV) and monolayer ($E_g \approx 2$ eV) phase, considerably high mobility (>1000 cm^2/Vs), makes it a good trade-off between graphene and TMDs. Furthermore, the achievable superb an on-off transistor ratio of above 10^5, makes bP a suitable candidate for detection of the THz-frequency light.

Vitti *et al*. first demonstrated the bP THz photodetectors operated at room temperature in 2015 [115]. They exploited the integration of a mechanically SiO_2-encapsulated bP flake in an antenna-coupled top-gate FET, as is shown in Fig. 58. A standard adhesive tape technique was used to transfer flake on a 300-nm thick SiO_2 layer on the top of a 300-μm intrinsic silicon wafer. The selected bP flakes with a thickness of about 10 nm coincide with the out-of-plane screening length and correspond to ≈16 layers of phosphorene. This choice ensures an ideal trade-off condition between high mobility and large carrier density tunability.

THz FET detectors have been fabricated by exploiting a combination of electron beam lithography and metal evaporation. The source (S) and gate (G) electrodes were patterned in the shape of two halves of a planar bow-tie antenna having a total length $2L = 500$ μm and a flare angle of 90°, in resonance with a 0.3-THz radiation. Figure 59 shows the device layout.

The photodetection mechanism in bP-based THz FETs was identified as a result of three mechanisms including

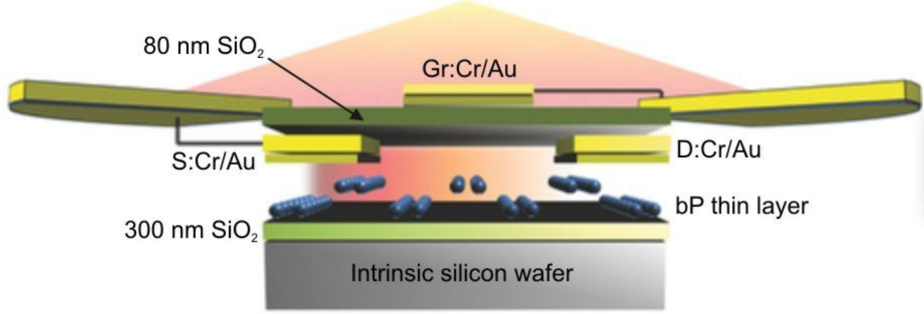

Fig. 58. Vertical sketch of the bP-FET structure [after Ref. 115].

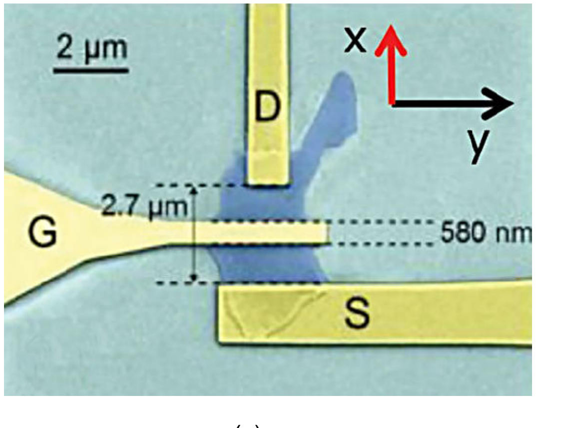

(a)

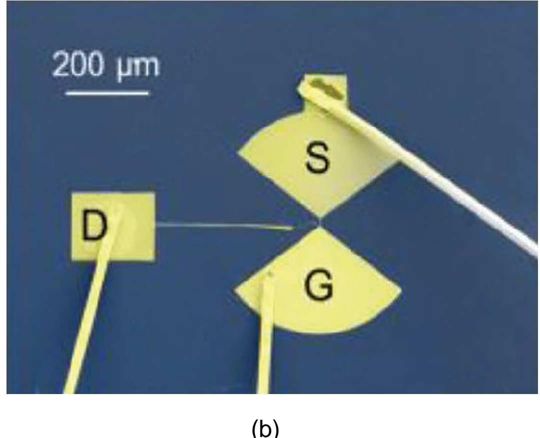

(b)

Fig. 59. Fabrication of the bP-FET structure: (a) false colours SEM image of the device [the channel length (L_c) is of 2.7 μm and the gate length (L_g) is of 530 nm], (b) S and G electrodes are designed to form a 500-μm, 90° flare angle, planar bow-tie, antenna; D electrode is connected to a rectangular bonding pad [after Ref. 115].

photothermoelectric, bolometric and plasma-wave rectification effects [115], and the anisotropy of bP [111]. For example, Figure 60 shows the extrapolated *NEP* curves for above three mechanisms which minimum reaches 7 nW/Hz$^{1/2}$, 10 nW/Hz$^{1/2}$, and 45 nW/Hz$^{1/2}$ for the bP-bolometer, plasma-wave and thermoelectric detector, respectively. The responsivity value of ~5-8 A/W at about 0.3 THz allows to use a bP FET device in application for a real-time pharmaceutical and quality control imaging [111].

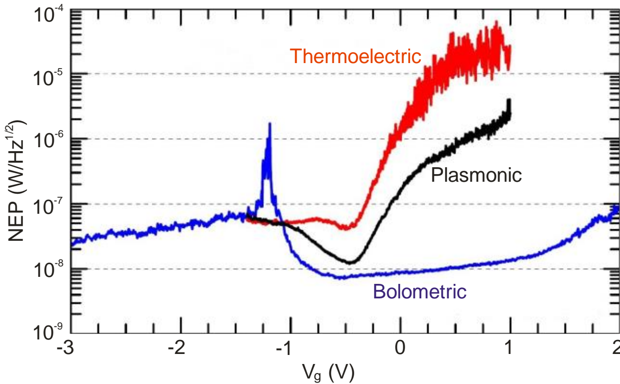

Fig. 60. Noise equivalent power as a function of gate voltage (V_g) for plasma-wave sample (0.29 THz), thermoelectric sample (0.32 THz), and bolometric sample detectors [after Ref. 111].

To prevent fast degradation of the exfoliated bP flake to ambient temperature, Viti *et al*. embedded a bP flake within a natural semiconductor heterostructure formed by multilayered h-BN crystals to devise hBN/bP/hBN heterostucture THz FET detectors shown in Fig. 61. The heterostructure was fabricated as previously (see Fig. 58) over a high resistivity silicon substrate covered with a SiO_2 cap layer. A 40-nm thick hBN flake with lateral dimensions of 20 × 20 μm^2 was put on the SiO_2/Si substrate to facilitate subsequent alignment step - transferring a bP flake onto the lower hBN layer. Before the deposition of the hBN top layer, the source (S) and drain (D) contacts were defined through a combination of electron beam lithography and metal deposition on the bP flake.

The FET hBN/bP/hBN heterostucture operated at 295 GHz is characterized by the minimum *NEP* of 100 pW/Hz$^{1/2}$ and the maximum R_v = 38 V/W at 4 K, whereas at room temperature ~10 nW/Hz$^{1/2}$ and ~2 V/W, respectively. hBN as an atomic dielectric constitutes a good encapsulating material for bP. In addition, hBN is a valuable gate dielectric which, in turn, allows the high gate-to-channel capacitance for tuning the device transport and optical properties. Viti *et al*. [154,155] have reviewed a recent research on bP detectors operating in the wider spectral range from 0.26 THz to 3.4 THz with emphasis on the future challenges in fabrication of stable and reliable optical and electronic technologies.

Recently, it was demonstrated that also topological insulators can be promising candidate materials for a broadband photodetection including THz range. Topological insulators (TIs) represent a novel quantum phase of matter, characterized by a semiconducting bulk and topologically protected surface states with a spin and momentum helical locking and the Dirac-like band structure [156,157]. 2D TIs are associated with gapless edge states and 3D insulators with gapless topological surface states (TSS) [158].

Intriguing properties of TIs result from:

- gapless of TSS what enables carrier generation by light absorption over a very wide energy spectrum including the THz range,
- optoelectronic properties which can be engineered by the material stoichiometry [159],
- high TSS mobility, even higher than graphene due to the topological protection that prevents backscattering effects [160], and
- 2D TSS electron gas of 3D TIs supports a collective excitation (Dirac plasmons) in the THz range [161].

Most of the published papers concern visible and short wavelength infrared TIs photodetectors [162]. The promising application of THz plasmonics with TIs is related to the rectification of THz radiation via excitation of plasma waves in the active channel of antenna-coupled FETs.

The first demonstration of THz detection mediated by TSS in top-gated nanometer FETs exploiting thin $Bi_2Te_{3-x}Se_x$ flakes was demonstrated by Viti *et al*. in 2016 [163] (Fig. 62). Flakes having total length of <2 μm have been selected as active nonlinear elements of FETs, in order to reduce both the parasitic capacitance and the resistances in the ungated transistor regions. By engineering the $Bi_2Te_{3-x}Se_x$ stoichiometry and mediating the RT THz

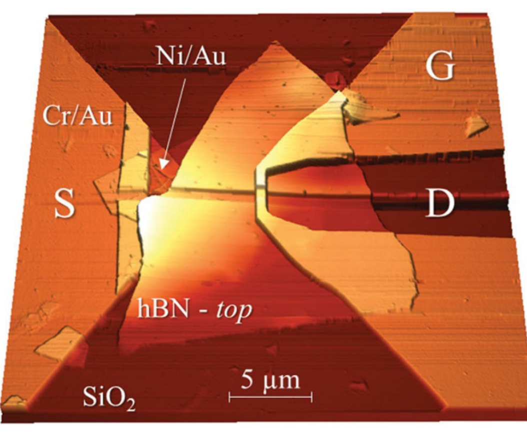

(a)

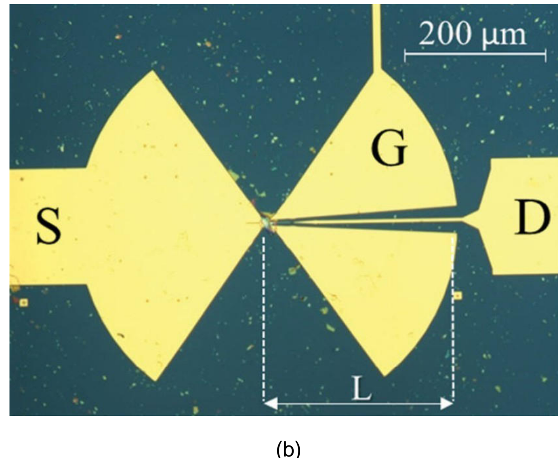

(b)

Fig. 61. hBN/bP/hBN heterostucture THz FET detectors: (a) AFM tomographic image of the top-gate FET, (b) optical microscopy image of the fabricated device. The bow arm length is L = 250 μm (after Ref. 154).

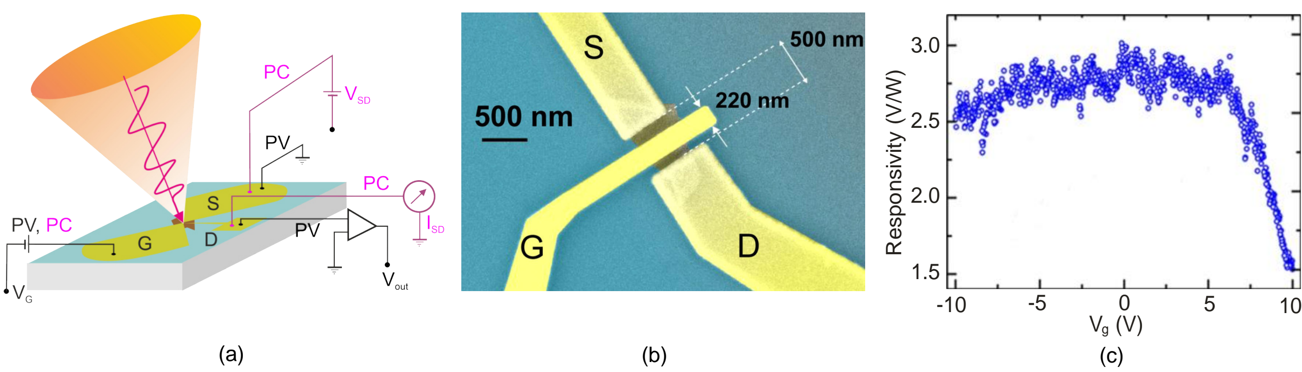

Fig. 62. Top-gated nanometer FET exploiting thin $Bi_2Te_{3-x}Se_x$ flake: (a) schematics of the THz detection principle, where photovoltage and photocurrent modes are depicted in black and purple, respectively; (b) false colours SEM image of the top-gated FET; S, G, and D stand for source, gate, and drain, respectively; and (c) experimental responsivity measured at room-temperature at a fixed frequency ν = 292.7 GHz while sweeping the gate bias V_g in the range (−10 V, + 10 V) [after Ref. 163].

detection with overdamped plasma-wave oscillations, the maximum responsivity of 3.0 V/W and the minimum *NEP* of ~10 nW/Hz$^{1/2}$ has been achieved for a 292.7 GHz impinging radiation frequency. Using this detector, the 400 × 700 pixel image of a target object was acquired with a time constant of 20 ms. This experiment gives a realistic impact on the exploitation of TSS for a large-area, fast THz imaging.

Also, another structure of TI THz photodetectors has been proposed. Yao *et al.* [145] proposed a Bi_2Te_3-Si heterojunction detector schematically shown in Fig. 63(a). The Bi_2Te_3 film, 300 μm in diameter and 100 nm in thickness, was grown onto the Si wafer by a pulsed laser deposition. Pt and Ag electrode contacts were then deposited on the top surface of the Bi_2Te_3 and bottom surface of Si, respectively. The device demonstrated photoresponse at room-temperature in the range from ultraviolet (370.6 nm) to terahertz (118 μm).

An innovative strategy for a direct detection of THz photons at room temperature based on a subwavelength metal-Bi_2Se_3-metal structure has been proposed in Ref. 164 [see Fig. 63(b)]. In this device the contact metal converts incident radiation into a localized surface-plasmon field which drives back and forth the TSS. The measured room-temperature responsivity of a device working in the self-powered and bias modes at 0.3 THz was of 75 and 475 A/W, respectively. *NEP* value of 3.6 × 10^{-13} W/Hz$^{1/2}$ and detectivity of 2.17 × 10^{11} cmHz$^{1/2}$/W have been achieved for a device working under a bias current of 50 mV. These results are crucial in fruition of TIs in the field of THz imaging applications.

4.4. 2D material detector performance - the present status

Development of pristine 2D material high sensitivity photodetectors is determined by two major challenges: low optical absorption in thin active region (~100–200 nm) and short photocarrier lifetime. Similar to graphene-based detectors, the remaining 2D photodetectors are limited by a trade-off between high responsivity, ultrafast response time, and broadband operation. Photodetectors based on 2D materials display a large variation in their current responsivity and response time [29-31] - about 9 orders of magnitudes as is shown in Fig. 64. The current studies are mostly limited to exfoliated materials from bulk layered crystals, with very limited yields, reproducibility and scalability. In consequence, the divergence in responsivity values is large. Moreover, a strong influence on relation between current responsivity and response time has the photogating effect what is shown in Fig. 64(b).

To enhance the infrared absorption, multiple layers instead of the single layer are selected. High photogain is often realized by using 2D material as the fast transfer

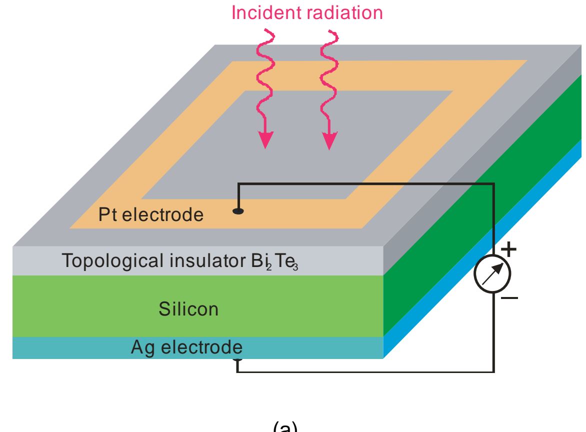

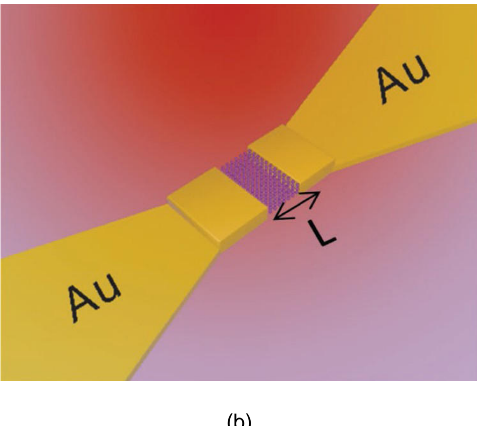

Fig. 63. Structures of THz photodetectors with topological insulators: (a) Bi_2Te_3-Si heterojunction in a two pole structure (the forward bias is defined as applying a positive bias on the Bi_2Te_3 side) [after Ref. 145], (b) metal-Bi_2Se_3-metal structure (the spacing distance *L* between the two gold contacts is much shorter than the wavelength radiation) [after Ref. 164].

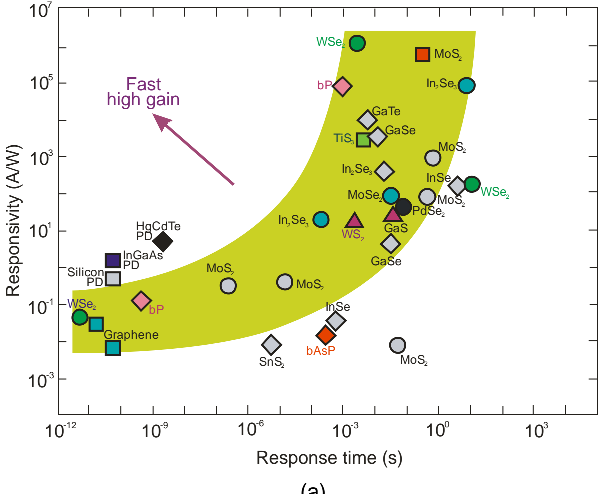

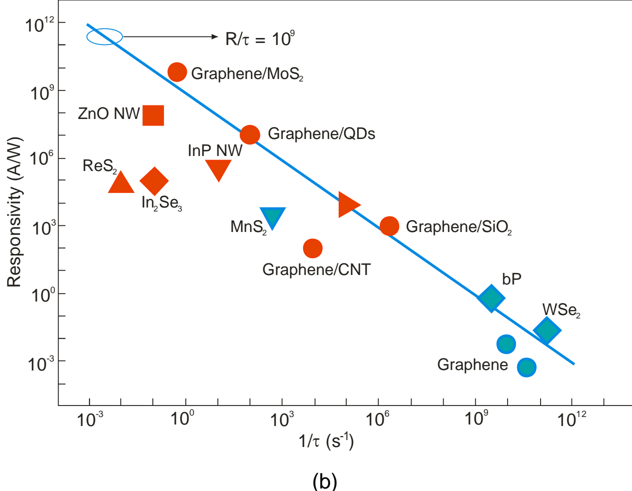

Fig. 64. Room-temperature current responsivity against response time for 2D material photodetectors: (a) in comparison with commercial silicon, InGaAs and HgCdTe photodiodes (many data are taken from Ref. 29), and (b) for part low-dimensional photodetectors (after Ref. 61); the blue line represents a typical magnitude order of gain-bandwidth product for traditional high-performance thin-film photodetectors, red symbol indicates that this is a photogaiting enhanced photodetector.

channel for charge carriers. However, as is mentioned in section 3, their general drawback is a very slow response time attributed to traps and enhanced capacitance (up to 10^4 ms). The response time at room temperature is typically longer than ~0.1 ms, what indicates a considerably longer response time in comparison with commercial silicon, InGaAs, and HgCdTe photodiodes; for HOT photodiodes it is typically between 1 and 10 ns. The up-left blank panel of Fig. 64(a) indicates the lack of photodetectors with both ultrahigh responsivity and ultrafast response speed. This observation is also supported by Fig. 64(b). It is also well known that the high gain induced by a long carrier lifetime can also cause both large generation-recombination noise and slow speed which is adverse to improve the device detectivity. In detector focal plane arrays, the suitable response time depends on pixel number, signal readout mode, driving integrated circuit design rules, and others.

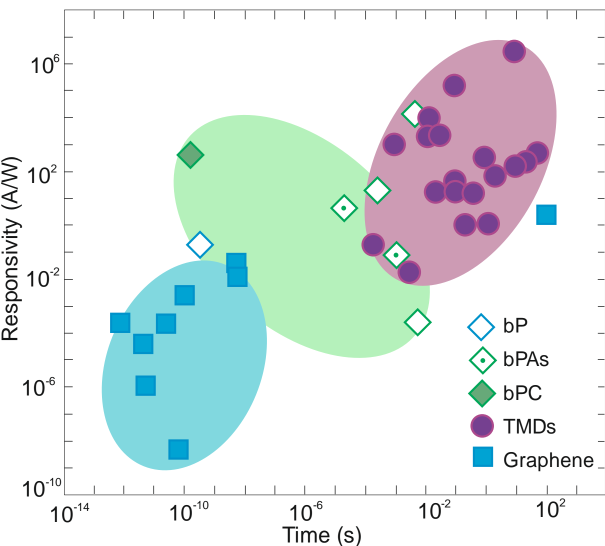

Fig. 65. Summary of the responsivity and response time of photodetectors based on different groups of 2D materials - graphene-based, black phosphorus (bP) and transition metal dichalcogenides (TMDs) (after Ref. 32)

The photoresponsivity and response time of different 2D material photodetectors are summerized in Fig. 65. It is shown that bP falls into a region between graphene and TMDs. However, degradation in air and other environments is an unresolved issue that may limit bP future applications [165]. bP degrades rapidly under room conditions, affecting its structure and properties. In particular the role of different ambient species has remained controversial. A considerably better stability is observed for noble transition metal dichalcogenides with a record room-temperature detectivity measured for a $PdSe_2/MoS_2$ heterostructure, of about 10^{10} Jones, in a long wavelength infrared range [129].

Another look on the 2D material gives the experimentally measured relation between detectivity and response time shown in Fig. 66 for photodetectors operated mainly in the visible and SWIR spectral regions [166]. The large variation in responsivity and response time (Fig. 64) influences about 10 orders of magnitude change in the D^*f product - between 10^7 and 10^{17} Jones·Hz.

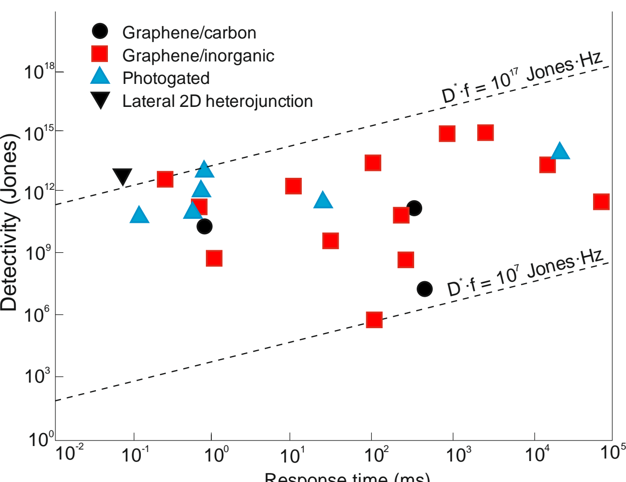

Fig. 66. The state-of-the-art graphene heterojunction devices (after Ref. 166).

Although a photodetection platform based on 2D materials has demonstrated a variety of potential applications, outstanding challenges remain to be implemented in order to exploit distinct advantages of these new materials. Prospects for commercialization will not just depend on the detector performance, but on distinct advantages in the ability for fabrication of large scale high quality 2D materials at a low cost. The final goal is to establish a large scale integration of 2D crystals with existing photonic and electronic platforms, such as CMOS technologies [18].

Most of 2D material photodetectors obtaining a high-performance are based on thin layers or heterostructures. Such devices are achieved by mechanical exfoliation which is not a repeatable process. For this reason, there is still a significant need for a 2D material technology improvement in order to obtain well-developed industrially applicable devices. One of the critically important issues is the stability and quality of 2D materials. Although many efforts have been devoted to synthesizing large-size single-crystal 2D materials, it is still hard to obtain single-crystals larger than millimetre size and grain size and sample size of TMDs are even smaller. Using a CVD grown technique, relatively large size samples can be obtained, but they have defects and contaminations which can cause sample degradation with time and, in consequence, make not stable devices [167].

Generally, TMD layered semiconducting material photodetectors operate at the visible and near-infrared regions and generally their high sensitivity does not coincide with the fast response time. In comparison with a response time in the nanosecond range of HgCdTe photodiodes and T2SL IB QCIPs operated at room temperature, the response time of TMD is typically in the millisecond range. This indicates that 2D infrared photodetectors operated at room temperature are not ready for real applications. b-AsP alloys have emerged as candidate 2D materials for detection of a long wavelength infrared radiation with performance comparable to commercial HgCdTe photodiodes. However, instability of the surface due to chemical degradation in ambient conditions remains a major impediment to its prospective applications [18]. More promising are stable noble TMD photodetectors like a $PdSe_2/MoS_2$ heterojunction with a record detectivity in the LWIR range at room temperature. However, their practical application lies in a perfect material synthesis and processing. To achieve it, 2D material photodetectors have a long way to go.

5. Conclusions

There are many critical challenges for future civilian and military infrared and terahertz detector applications. The main efforts are directed to decrease infrared imaging systems size, weight, and power consumption (SWaP) by increasing the detector arrays operating temperature. Nowadays, HgCdTe is the most widely used variable gap semiconductor for IR photodetectors, including uncooled operation, and stands reference for alternative technologies. However, in spite of a sixty year development history of the HgCdTe ternary alloy system, its ultimate HOT performance limit has not been achieved.

At present, the Rule 07 metric is not a proper approach for prediction of the HgCdTe detector and system performance, and also as a reference benchmark for alternative technologies (often used especially for T2SLs and CQD). It is shown [136], that for a sufficiently long SRH carrier lifetime in HgCdTe ternary alloy, what is experimentally supported by Teledyne at doping level below 5×10^{13} cm^{-3}, the internal P-i-N HgCdTe photodiode current is suppressed and the detector performance is limited by the background radiation. HgCdTe photodiodes operated in the longer wavelength infrared range (above 3 μm) guarantee achieving more than one order of magnitude higher detectivity (above 10^{10} Jones) in comparison with the value predicted by Rule 07. This new benchmark, Law 19, corresponds exactly to the detector background limited performance curve for room temperature. In this context our paper evaluates new class of emerging 2D material technologies for HOT infrared photodetectors.

The future applications of imaging infrared systems require [58]:

- higher pixel sensitivity,
- further increases in pixel count to above 10^8 pixels (mosaicking may be used) with a pixel size decreasing to about 5 μm for both cooled and uncooled LWIR applications,
- cost reduction in imaging array systems through the use of integration of detectors and signal processing functions (with much more on-chip signal processing) and less cooling sensor technology,
- improvement in the functionality of imaging arrays through development of multispectral sensors.

Small-pitch IR FPAs will require the development of larger effective ROIC well capacities per unit area, possibly faster optics than *f*/1, and improved hybridization technologies [58] dominated currently in IR arrays fabrication. Leveraging deeply scaled CMOS process technology enables designers to miniaturize pixel pitch and/or increase on-chip processing capability depending on application-specific needs. Array sizes will continue to increase but perhaps at a rate that falls below the Moore's Law curve. An increase in array size is already technically feasible. However, the market forces that have demanded larger arrays are not as strong now that the megapixel barrier has been broken [1].

At present, the performance of single room-temperature 2D material photodetectors operated in the infrared and terahertz spectral ranges is comparable to that of standard commercial photodetectors (InGaAs and HgCdTe). b-AsP alloys and noble TMD photodetectors have emerged as candidates for detection of a long wavelength infrared radiation with higher detectivities in comparison with commercial HgCdTe photodiodes. However, black phosphorus instability remains a major impediment to its prospective applications. More promising are stable noble TMD photodetectors like a $PdSe_2/MoS_2$ heterojunction with record detectivity in the LWIR range at room temperature. However, their practical application lies in a perfect material synthesis and processing. Due to the mature HgCdTe technology, it is rather difficult to compete 2D material with HgCdTe photodiodes.

First 2D material based imaging sensors operated in the visible and short wavelength infrared region have been demonstrated [32]. A dual band vertical GaSe/GaSb hetero-

structure linear array (16 × 1) was fabricated by a MBE growth technique in 2017 [168]. Also, small 388 × 288 20-µm pixel GQDs based CMOS integrated sensor has been later demonstrated [142]. Graphene is particularly attractive due to its compatibility with silicon and monolithic integration with CMOS integrated circuit. In a way, graphene has been a victim of its own success, getting people overly excited about it and producing unrealistic expectations. Development of photodetectors toward high performance, high integration, and large focal plane arrays is particularly critical for practical applications of 2D photodetectors in industrialization. It will take several decades of research, development and most importantly billions of dollars of investment at the national and international level to become the ultimate benchmark for standard electronic materials and devices.

Next, we follow after Ref. 169 in order to compare different detector technologies existed on global market with emerging 2D photodetectors. Table 7 provides a snapshot of the current state of development of LWIR detectors fabricated from different material systems. Note that TRL means technology readiness level. The highest level of TRL (ideal maturity) achieves the value of 10. The highest level of maturity (TRL = 9) is credited to HgCdTe photodiodes and microbolometers. A little less, TRL = 8, for QWPs. The $A^{III}B^{V}$ T2SL structures have great potential for the LWIR spectral range application with performance comparable to HgCdTe for the same cut-off wavelength. Strong progress toward mature superlattice and barrier detector technologies, including their commercialization, has been observed in the last decade. 2D material detector technology is at a very early stage of development (TRL = 1-2).

Table 7
Comparison of LWIR existing state-of-the-art device systems for LWIR detectors
Note: TRL - technology readiness level [after Ref. 170 and 171].

	Bolometer	**HgCdTe**	**QWIP**	**Type-II SLs**	**2D materials**
Maturity level	TRL 9	TRL 9	TRL 9	TRL 6-7	TRL 1-2
Status	Material of choice for application requiring medium to low performance	Material of choice for application requiring high performance	Commercial	Research and development	Research
Operating temp.	Un-cooled	Cooled	Cooled	Cooled	Un-cooled
Manufacturability	Excellent	Poor	Excellent	Very good	Very poor
Cost	Low	High	Medium	Medium	?
Prospect for large format	Excellent	Very good	Excellent	Excellent	?
Availability of large substrate	Excellent	Poor	Excellent	Very good	Very good
Military system examples	Weapon sight, night vision goggles, missile seekers, small UAV sensors, unattended ground sensors	Missile intercept, tactical ground and air born imaging, hyper spectral, missile seeker, missile tracking, space based sensing	Being evaluated for some military applications and astronomy sensing	Being developed in university and evaluated industry research environment	Military wearable devices
Limitations	Low sensitivity and long-time constants	Performance susceptible to manufacturing variations. Difficult to extend to >14-µm cut-off	Narrow bandwith and low sensitivity	Requires a significant investment and fundamental material breakthrough to mature	Very limited yields, reproducibility and scalability; requires radical breakthrough to mature technology
Advantages	Low cost and requires no active cooling, leverages standard Si manufacturing equipment	Near theoretical performance, will remain material of choice for minimum of the next several years	Low cost applications. Leverages commercial manufacturing processes. Very uniform material	Theoretically better then HgCdTe, leverages commercial III-V fabrication techniques	Performance of single devices comparable with standard devices

Authors' statement

For research articles with several authors, a short paragraph specifying their individual contributions must be provided. The following statements should be used: research concept and design, A.R.; collection and/or assembly of data, A.R. and M.K.; data analysis and interpretation, A.R., M.K. and P.M.; writing the article, A.R.; critical revision of the article, M.K. and P.M.; final approval of article, P.M.". Authorship must be limited to those who have contributed substantially to the work reported.

Acknowledgements

This work was supported by the funds granted to the Faculty of Advanced Technologies and Chemistry, Military University of Technology, within the subsidy for maintaining research potential in 2020, grant no. UGB763.

References

[1] Rogalski, A. Graphene-based materials in the infrared and terahertz detector families: a tutorial. *Adv. Opt. Photonics* **11**, 314 (2019).

[2] Iwert, O. & Delabrea, B. The challenge of highly curved monolithic imaging detectors. *Proc. SPIE* **7742**, 774227–1–9 (2010).

[3] Jeong, K.-H. Kim, J. & Lee, L. P. Biologically inspired artificial compound eyes. *Science (80-.).* **312**, 557–561 (2006).

[4] Song, Y. M., Xie, Y., Malyarchuk, V., Xiao, J., Jung, I., Choi, K.-J., Liu, Z., Park, H., Lu, C., Kim, R. H., Li, R., Crozier, K. B., Huang, Y. & Rogers, J. A. Digital cameras with designs inspired by the arthropod eye. *Nature* **497**, 95–99 (2013).

[5] Tang, X., Ackerman, M. M. & Guyot-Sionnest, P. Colloidal quantum dots based infrared electronic eyes for multispectral imaging. *Proc. SPIE* **11088**, 1108803–1–7 (2019).

[6] Lu, Q., Liu, W. & Wang, X. 2-D material-based photodetectors on flexible substrates. in *Inorganic Flexible Optoelectronics: Materials and Applications* (eds. Ma, Z. & Liu, D.) 117–142 (Wiley-VCH Verlag, 2019).

[7] *International Roadmap for Devices and Systems™. 2018 Update. More Moore*. https://irds.ieee.org/images/files/pdf/2018/2018IRDS_MM.pdf

[8] Briggs, N., Subramanian, S., Lin, Z., Li, X., Zhang, X., Zhang, K., Xia, K., Geohegan, D., Wallace, R., Chen, L.- Q., Terrones, M., Ebrahimi, A., Das, S., Redwing, J., Hinkle, C., Momeni, K., van Duin, A., Crespi, V., Kar, S. & Robinson, J. A. A roadmap for electronic grade 2D materials. *2D Mater*. **6**, 022001 (2019).

[9] Bonaccorso, F., Sun, Z., Hasan, T. & Ferrari, A. C. Graphene photonics and optoelectronics. *Nat. Photonics* **4**, 611–622 (2010).

[10] Li, X., Tao, L., Chen, Z., Fang, H., Li, X., Wang, X., Xu, J.-B. & Zhu, H. Graphene and related two-dimensional materials: Structure-property relationships for electronics and optoelectronics. *Appl. Phys. Rev.* **4**, 021306–1–31 (2017).

[11] Xia, F., Mueller, T., Lin, Y. M., Valdes-Garcia, A. & Avouris, P. Ultrafast graphene photodetector. *Nat. Nanotechnol.* **4**, 839–843 (2009).

[12] Wang, G., Zhang, Y., You, C., Liu, B., Yang, Y., Li, H., Cui, A., Liu, D. & Yan, H. Two dimensional materials based photodetectors. *Infrared Phys. Technol.* **88**, 149–173 (2018).

[13] Bae, S., Kim, H., Lee, Y., Xu, X., Park, J.-S., Zheng, Y., Balakrishnan, J., Lei, T., Kim, H. R., Song, Y. I., Kim, Y.- J., Kim, K. S., Özyilmaz, B., Ahn, J.- H., Hong, B. H. & Iijima, S. Roll-to-roll production of 30-inch graphene films for transparent electrodes. *Nat. Nanotechnol.* **4**, 574–578 (2010).

[14] Akinwande, D., Petrone, N. & Hone, J. Two-dimensional flexible nanoelectronics. *Nat. Commun.* **5**, 5678 (2014).

[15] Liu, M., Yin, X., Ulin-Avila, E., Geng, B., Zentgraf, T., Ju, L., Wang, F. & Zhang, X. A graphene-based broadband optical modulator. *Nature* **474**, 64–67 (2011).

[16] Grigorenko, A. N., Polini, M. & Novoselov, K. S. Graphene plasmonics. *Nat. Photonics* **6**, 749–758 (2012).

[17] Sun, Z., Hasan, T., Torrisi, F., Popa, D., Privitera, G., Wang, F., Bonaccorso, F., Basko, D. M. & Ferrari, A. C. Graphene mode-locked ultrafast laser. *ACS Nano* **4**, 803–810 (2010).

[18] Rogalski, A. Kopytko, M. & Martyniuk. P. Two dimensional infrared and terahertz detectors: Outlook and status. *Appl. Phys. Rev.* **6**, 021316 (2019).

[19] Rogalski, A., *2D Materials for Infrared and Terahertz Detectors*. (CRC Press, Boca Raton, 2020).

[20] Novoselov, K. S., Geim, A. K., Morozov, S. V., Jiang, D., Zhang, Y., Dubonos, S. V., Grigorieva, I. V. & Firsov, A. A. Electric field effect in atomically thin carbon films. *Science* **306**, 666–669 (2004).

[21] Novoselov, K. S., Geim, A. K., Morozov, S. V., Jiang, D., Katsnelson, M. I., Grigorieva, I. V., Dubonos, S. V. & Firsov, A. A. Two-dimensional gas of massless Dirac fermions in graphene. *Nature* **438**, 197–200 (2005).

[22] Geim A. K. & Novoselov, K. S. The rise of graphene. *Nat. Mater*. **6**, 183–191 (2007).

[23] Xia, F., Yan, H. & Avouris, P. The interaction of light and graphene: Basic, devices, and applications. *Proc. IEEE* **101**, 1717–1731 (2013).

[24] Chen, J.- H., Jang, C., Xiao, S., Ishigami, M. & Fuhrer, M. S. Intrinsic and extrinsic performance limits of graphene devices on SiO_2. *Nat. Nanotechnol.* **3**, 206–209 (2008).

[25] Nair, R. R., Blake, P., Grigorenko, A. N., Novoselov, K. S., Booth, T. J., Stauber, T. Peres, N. M. R. & Geim, A. K. Fine structure constant defines visual transparency of graphene. *Science* **320**, 1308 (2008).

[26] Low T. & Avouris, P. Graphene plasmonic for terahertz to mid-infrared applications. *ACS Nano* **8**(2), 1086–1001, 2014.

[27] Nicolosi, V., Chhowalla, M., Kanatzidis, M. G., Strano, M. S. & Coleman, J. N. Liquid exfoliation of layered materials. *Science* **340**, 1226419 (2013).

[28] Zhang, B., Liu, J., Wang, C., Yang, K., Lee, C., Zhang, H. & He J. Recent progress in 2D material-based saturable absorbers for all solid-state pulsed bulk lasers. *Laser Photonics Rev.* **14**, 1900240 (2020).

[29] Wang, J., Fang, H., Wang, X., Chen, X., Lu, W. & Hu, W. Recent progress on localized field enhanced two-dimensional material photodetectors from ultraviolet-visible to infrared. *Small* **13**, 1700894 (2017).

[30] Wang, X., Sun, Y. & Liu, K. Chemical and structural stability of 2D layered materials. *2D Mater.* **6**, 042001 (2019).

[31] Buscema, M., Islan, J. O., Groenendijk, D. J., Blanter, S. I., Steele, G. A., van der Zant, H. S. J. & Castellanos-Gomez, A. Photocurrent generation with two-dimensional van der Waals semiconductor. *Chem. Soc. Rev.* **44**, 3691–3718 (2015).

[32] Long, M., Wang, P., Fang, H. & Hu, W. Progress, challenges, and opportunities for 2D material based photodetectors. *Adv. Funct. Mater*. **29**, 1803807 (2018).

[33] Wang, F., Wang, Z., Yin, L., Cheng, R., Wang, J., Wen, Y., Shifa, T. A., Wang, F., Zhang, Y., Zhan, X. & He, J. 2D library beyond graphene and transition metal dichalcogenides: a focus on photodetection. *Chem. Soc. Rev.* **47**, 6296–6341 (2018).

[34] Liu, T., Tong, L., Huang, X. & Ye, L. Room-temperature infrared photodetectors with hybrid structure based on two-dimensional materials. *Chin. Phys. B* **28**, 017302–1–19 (2019).

[35] Cheng, J., Wang, C., Zou, X. & Liao, L. Recent advances in optoelectronic devices based on 2D materials and their heterostructures. *Adv. Opt. Mater*. **7**, 1800441 (2019).

[36] Britnell, L., Ribeiro, R. M., Eckmann, A., Jalil, R., Belle, B. D., Mishchenko, A., Kim, Y.- J., Gorbachev, R. V., Georgiou, T., Morozov, S. V., Grigorenko, A. N., Geim, A. K., Casiraghi, C., Castro Neto, A. H. & Novoselov, K. S. Strong light-matter interactions in heterostructures of atomically thin films. *Science* **340**, 1311–1313 (2013).

[37] Dai, Z., Liu, L. & Zhang, Z. Strain engineering of 2D materials: Issues and opportunities at the interface. *Adv. Mater.* **31**, 1805417 (2019).

[38] Manzeli, S., Ovchinnikov, D., Pasquier, D., Yazyev, O. V. & Kis, A. 2D transition metal dichalcogenides. *Nat. Rev. Mater.* **2**, 1–15 (2017).

[39] Pi, L., Li, L., Liu, K., Zhang, Q., Li, H. & Zhai, T. Recent progress on 2D noble-transition-metal dichalcogenides. *Adv. Funct. Mater.* **29**, 1904932 (2019).

[40] Yang, Z., Dou J. & Wang, M. Graphene, transition metal dichalcogenides, and perovskite photodetectors. in *Two-dimensional Materials for Photodetector* (Intech, 2018).

[41] Mark K. F. & Shan, J. Photonics and optoelectronics of 2D semiconductor transition metal dichalcogenides. *Nat. Photonics* **10**, 216–226 (2016).

[42] Wang, P., Bao, Q. & Hu, W. Infrared photodetectors. in *2D Materials for Photonic and Optoelectronic Applications* (eds. Bao, Q. & Hoh, H. Y.) 105–115 (Elsevier, Amsterdam, 2020).

[43] Zhang, W., Huang, Z., Zhang, W. & Li, Y. Two-dimensional semiconductors with possible high room temperature mobility. *Nano Res.* **7**, 1731–1737 (2014).

[44] Zhao, Y., Qiao, J., Yu, Z., Yu, P., Xu, K., Lau, S. P., Zhou, W., Liu, Z., Wang, X., Ji, W.& Chai, Y. High-electron-mobility and air-stable 2D layered $PtSe_2$ FETs. *Adv. Mater.* **29**, 1604230 (2017).

[45] Habib, M. R., Chen, W., Yin, W.- Y., Su, H. & Xu, M. Simulation of transition metal dichalcogenides, in *Two Dimensional Transition Metal Dichalcogenides. Synthesis, Properties, and Applications* (eds. Arul, N. S. & Nithya, V. D.) 135–172 (Springer, Singapore, 2019).

[46] Yu, X., Yu, P., Wu, D., Singh, B., Zeng, Q., Lin, H., Zhou, W., Lin, J., Suenaga, K., Liu, Z. & Wang, Q. J. Atomically thin noble metal dichalcogenide: a broadband mid-infrared semiconductor. *Nat. Commun.* **9**, 1545 (2018).

[47] Zeng, L.- H., Wu, D., Lin, S.- H., Xie, C., Yuan, H.- Y, Lu, W., Lau, S. P., Chai, Y., Luo, L.- B., Li, Z.- J. & Tsang, Y. H. Controlled synthesis of 2D palladium diselenide for sensitive photodetector applications. *Adv. Funct. Mater.* **29**, 1806878 (2019).

[48] Bridgman, P. W. Two new modifications of phosphorus. *J. Am. Chem. Soc.* **36**, 1344–1363 (1914).

[49] Li, L., Yu, Y., Ye, G. J., Ge, Q., Ou, X., Wu, H., Feng, D., Chen, X. H. & Zhang, Y. Black phosphorus field-effect transistors. *Nat. Nanotechnol.* **9**, 372–377 (2014).

[50] Ling, X., Wang, H., Huang, S., Xia, F. & Dresselhaus, M. S. The renaissance of black phosphorus. *PNAS* **112**, 4523–4530 (2015).

[51] Akahama, Y., Endo, S. & Narita, S. Electrical properties of black phosphorus single crystals. *J. Phys. Soc. Jpn*. **52**, 2148–2155 (1983).

[52] Tran, V., Soklaski, R., Liang, Y. & Yang, L. Layer-controlled band gap and anisotropic excitons in few-layer black phosphorus. *Phys. Rev. B* **89**, 235319 (2014).

[53] Das, S., Zhang, W., Demarteau, M., Hoffmann, A., Dubey, M. & Roelofs, A, Tunable transport gap in phosphorene. *Nano Lett*. **14**, 5733–5739 (2014).

[54] Liu, B., Köpf, M., Abbas, A. N., Wang, X., Guo, Q., Jia, Y., Xia, F., Weihrich, R., Bachhuber, F., Pielnhofer, F., Wang, H., Dhall, R., Cronin, S. B., Ge, M., Fang, X., Nilges, T. & Zhou, C. Black arsenic–phosphorus: layered anisotropic infrared semiconductors with highly tunable compositions and properties. *Adv. Mater*. **27**, 4423–4429 (2015).

[55] Wood, J. D., Wells, S. A., Jariwala, D., Chen, K. S., Cho, E., Sangwan, V. K, Liu, X., Lauhon, L. J., Marks, T. J. & Hersam, M. C. Effective passivation of exfoliated black phosphorus transistors against ambient degradation. *Nano Lett.* **14**, 6964–6970 (2014).

[56] Island, J. O., Steele, G. A., van der Zant, H. S. J. & Castellanos-Gomez, A. Environmental instability of few-layer black phosphorus. *2D Mater.* **2**, 011002 (2015).

[57] Razeghi, M. & Rogalski, A. Photoresistors. in *Wiley Encyclopedia of Electrical and Electronics Engineering* (ed Webster, J. G.) Vol. 16, 377–387 (Wiley, 1999).

[58] Rogalski, A. *Infrared and Terahertz Detectors*, third edition. (CRC Press, Boca Raton, 2019).

[59] Konstantatos, G., Badioli, M., Gaudreau, L., Osmond, J., Bernechea, M., Garcia de Arquer, F. P., Gatti, F. & Koppens, F. H. L. Hybrid graphene-quantum dot phototransistors with ultrahigh gain. *Nat. Nanotechnol.* **7**, 363–368 (2012).

[60] Koppens, F. H. L., Mueller, T., Avouris, P., Ferrari, A. C., Vitiello M. S. & Polini, M. Photodetectors based on graphene, other two-dimensional materials and hybrid systems. *Nat. Nanotechnol.* **9**, 780–793 (2014).

[61] Fang H. & Hu, W. Photogating in low dimensional photodetectors. *Adv. Sci*. **4**, 1700323 (2017).

[62] Wang, P., Xia, H., Li, Q., Wang, F., Zhang, L., Li, T., Martyniuk, P., Rogalski, A. & Hu, W. Sensing infrared photons at room temperature: from bulk materials to atomic layers. *Small* **46**, 1904396 (2019).

[63] Mott N. & Jones, H. *The Theory of the Properties of Metals and Alloys.* (The Clarendon Press, 1936).

[64] Nourbakhsh, A., Yu, L., Lin, Y., Hempel, M., Shiue, R.- J., Englund, D. & Palacios, T. Heterogeneous integration of 2D materials and devices on a Si platfor. in *Beyond-CMOS Technologies for Next Generation Computer Design* (eds. Topaloglu R. O. & Wong, H.- S. P.) 43–84 (Springer, 2019).

[65] Du, X., Prober, D. E., Vora, H. & Mckitterick, Ch. B. Graphene-based bolometers. *Graphene & 2D Mater*. **1**, 1–22 (2014).

[66] Pop, E., Varshney, V. & Roy, A. K. Thermal properties of graphene: Fundamentals and applications. *MRS Bulletin* **37**, 1273–1281 (2012).

[67] Rogalski, A. & Sizov, F. Terahertz detectors and focal plane arrays. *Opto−Electron. Rev.* **19**, 346‑404 (2011).

[68] Dyakonov M.& Shur, M. S. Shallow water analogy for a ballistic field effect transistor: new mechanism of plasma wave generation by the dc current. *Phys. Rev. Lett*. **71**, 2465–2468 (1993).

[69] Dyakonov M. & Shur, M. Plasma wave electronics: Novel terahertz devices using two dimensional electron fluid. *IEEE Trans. Electron Devices* **43**, 1640–1646 (1996).

[70] Shur M. & Ryzhii, V. Plasma wave electronics. *Int. J. High Speed Electr. Syst*. **13**, 575–600 (2003).

[71] Wang, H.- X., Wang, Q., Zhou, K.- G. & Zhang, H.- L. Graphene in light: Design, synthesis and applications of photo-active graphene and graphene-like materials. *Small* **9**(8), 1266–1283 (2013).

[72] Houssa, M., Dimoulas, A. & Molle, A. *2D Materials for Nanoelectronics*. (CRC Press, Boca Raton, 2016)

[73] Konstantatos, G. Current status and technological prospect of photodetectors based on two-dimensional materials. *Nat. Commun.* **9**, 52661–3 (2018).

[74] Avouris, P., Heinz, T. F. & Low, T. *2D Materials: Properties and Devices.* (Cambridge University Press, Cambridge, 2017).

[75] Zhang, Y., Liu, T., Meng, B., Li, X., Liang, G., Hu, X. & Wang, Q. J. Broadband high photoresponse from pure monolayer graphene photodetector. *Nat. Commun.* **4**, 1811 (2013).

[76] Chronopoulos, D., Bakandritsos, A., Pykal, M., Zboril, R. & Otyepka, M. Chemistry, properties, and applications of fluorographene. *Appl. Mater. Today* **9**, 60–70 (2017).

[77] Sun, Z., Liu, Z., Li, J., Tai, G., Lau, S.- P. & Yan, F. Infrared photodetectors based on CVD-grown graphene and PbS quantum dots with ultrahigh responsivity. *Adv. Mater*. **24**, 5878–5883 (2012).

[78] Guo, W., Xu, S., Wu, Z., Wang, N., Loy, M. M. T. & Du, S. Oxygen-assisted charge transfer between ZnO quantum dots and graphene. *Small* **9**, 3031–3036 (2013).

[79] Nikitskiy, I., Goossens, S., Kufer, D., Lasanta, T., Navickaite, G., Koppens, F. H. & Konstantatos, G. Integrating an electrically active colloidal quantum dot photodiode with a graphene phototransistor. *Nat. Commun*. **7**, 11954 (2016).

[80] Yu, X., Li, Y., Hu, X., Zhang, D., Tao, Y., Liu, Z., He, Y., Haque, M. A., Liu, Z., Wu, T. & Wang, Q. J. Narrow bandgap oxide nanoparticles coupled with graphene for high performance mid-infrared photodetection. *Nat. Commun.* **9**, 4299 (2018).

[81] Du, S., Lu, W., Ali, A., Zhao, P., Shehzad, K., Guo, H., Ma, L., Liu, X., Pi, X., Wang, P., Fang, H., Xu, Z., Gao, C., Dan, Y., Tan, P., Wang, H., Lin, C.-T., Yang, J., Dong, S., Cheng, Z., Li, E., Yin, W., Luo, J., Yu, B., Hasan, T., Xu, Y., Hu, W. & Duan, X. A broadband fluorographene photodetector. *Adv. Mater*. **29**, 1700463 (2017).

[82] Ryzhii, V., Otsuji, T., Ryzhii, M. & Shur, M. S. Double graphene-layer plasma resonances terahertz detector. *J. Phys. D: Appl. Phys*. **45**, 302001 (6pp) (2012).

[83] Liu, C. H., Chang, Y. C., Norris, T. B. & Zhong, Z. H. Graphene photodetectors with ultra-broadband and high responsivity at room temperature. *Nat. Nanotechnol*. **9**, 273–278 (2014).

[84] Gan, X., Shiue, R.-J., Yuanda, G., Meric, I., Heinz, T. F., Shepard, K., Hone, J., Assefa S. & Englund, D. Chip-integrated ultrafast

graphene photodetector with high responsivity. *Nat. Photonics* **7**, 883–887 (2013).

[85] Pospischil, A., Humer, M., Furchi, M. M., Bachmann, D., Guider, R., Fromherz, T. & Mueller, T. CMOS-compatible graphene photodetector covering all optical communication bands. *Nat. Photonics* **7**, 892–896 (2013).

[86] Wang, X. M., Cheng, Z. Z., Xu, K., Tsang, H. K. & Xu, J. B. High-responsivity graphene/silicon-heterostructure waveguide photodetectors. *Nat. Photonics* **7**, 888–891 (2013).

[87] Schall, D., Neumaier, D., Mohsin, M., Chmielak, B., Bolten, J., Porschatis, C., Prinzen, A., Matheisen, C., Kuebart, W., Junginger, B., Templ, W., Giesecke, A. L. & Kurz, H. 50 GBit/s photodetectors based on wafer-scale graphene for integrated silicon photonic communication systems. *ACS Photonics* **1**, 781–784 (2014).

[88] Echtermeyer, T. J., Britnell, L., Jasnos, P. K., Lombardo, A., Gorbachev, R. V., Grigorenko, A. N., Geim, A. K., Ferrari, A. C. & Novoselov, K. S. Strong plasmonic enhancement of photovoltage in graphene. *Nat. Commun*. **2**, 458 (2011).

[89] Liu, Y., Cheng, R., Liao, L., Zhou, H., Bai, J., Liu, G., Liu, L., Huang, Y. & Duan, X. Plasmon resonance enhanced multicolour photodetection by graphene. *Nat. Commun*. **2**, 579 (2011).

[90] Bandurin, D. A., Svintsov, D., Gayduchenko, I., Xu, S. G., Principi, A., Moskotin, M., Tretyakov, I., Yagodkin, D., Zhukov, S., Taniguchi, T., Watanabe, K., Grigorieva, I. V., Polini, M., Goltsman, G. N., Geim, A. K. & Fedorov, G. Resonant terahertz detection using graphene plasmons. *Nat. Commun*. **9**, 5392–1–8 (2018).

[91] Engel, M., Steiner, M., Lombardo, A., Ferrari, A. C., v. Löhneysen, H., Avouris, P. & Krupke, R. Light-matter interaction in a microcavity-controlled graphene transistor. *Nat. Commun*. **3**, 906 (2012).

[92] Gan, X., Mak, K. F., Gao, Y., You, Y., Hatami, F., Hone, J., Heinz, T. F. & Englund, D. Strong enhancement of light-matter interaction in graphene coupled to a photonic crystal nanocavity. *Nano Lett*. **12**, 5626–5631 (2012).

[93] Furchi, M., Urich, A., Pospischil, A., Lilley, G., Unterrainer, K., Detz, H., Klang, P., Andrews, A. M., Schrenk, W., Strasser, G. & Mueller, T. Microcavity-integrated graphene photodetector. *Nano Lett*. **12**, 2773–2777 (2012).

[94] Freitag, M., Low, T., Zhu, W., Yan, H., Xia, F. & Avouris, P. Photocurrent in graphene harnessed by tunable intrinsic plasmons. *Nat. Commun*. **4**, 1951 (2013).

[95] Ogawa, S., Shimatani, M., Fukushima, S., Okuda, S. & Matsumoto, K. Graphene on metal-insulator-metal-based plasmonic metamaterials at infrared wavelengths. *Opt. Express* **26**(5), 5665–5674 (2018).

[96] Shiue, R.- J., Gan, X., Gao, Y., Li, L., Yao, X., Szep, A., Walker Jr., D., Hone, J. & Eglund, D. Enhanced photodetection in graphene-integrated photonic crystal cavity. *Appl Phys. Lett*. **103**, 241109 (2013).

[97] Fang, Z., Liu, Z., Wang, Y., Ajayan, P. M., Nordlander, P. & Halas, N. J. Graphene–antenna sandwich photodetector. *Nano Lett*. **12**, 3808–3813 (2012).

[98] Yao, Y., Shankar, R., Rauter, P., Song, Y., Kong, J., Loncar, M. & Capasso, F. High-responsivity mid-infrared graphene detectors with antenna enhanced photocarrier generation and collection. *Nano Lett*. **14**, 3749–3754 (2014).

[99] Chakraborty, C., Beams, R., Goodfellow, K. M., Wicks, G. W., Novotny, L. & Vamivakas, A. N. Optical antenna enhanced graphene photodetector. *Appl. Phys. Lett*. **105**, 241114 (2014).

[100] Echtermeyer, T. J., Milana, S., Sassi, U., Eiden, A., Wu, M., Lidorikis, E. & Ferrari, A. C. Surface plasmon polariton graphene photodetectors. *Nano Lett*. **16**, 8–20 (2015).

[101] Liu, T., Tong, L., Huang, X. & Ye, L. Room-temperature infrared photodetectors with hybrid structure based on two-dimensional materials. *Chin. Phys. B* **28**, 017302–1–19 (2019).

[102] Chen, Z., Li, X., Wang, J., Tao, L., Long, M., Liang, S.-J., Ang, L. K., Shu, C., Tsang, H. K. & Xu, J.-B. Synergistic effects of plasmonics and electron trapping in graphene short-wave infrared photodetectors with ultrahigh responsivity. *ACS Nano* **11**, 430–437 (2017).

[103] Cakmakyapan, S., Lu, P. K., Navabi, A. & Jarrahi, M. Gold-patched graphene nano-stripes for high-responsivity and ultrafast photodetection from the visible to infrared regime. *Light Sci. Appl.* **7**, 20 (2018).

[104] Hsu, A. L., Herring, P. K., Gabor, N. M., Ha, S., Shin, Y. C., Song, Y., Chin, M., Dubey, M., Chandrakasan, A. P., Kong, J., Jarillo-Herrero, P. & Palacios, T. Graphene-based thermopile for thermal imaging applications. *Nano Lett*. **15**, 7211–7216 (2015).

[105] Yan, J., Kim, M.- H., Elle, J. A., Sushkov, A. B., Jenkins, G. S., Milchberg, H. M., Fuhrer, M. S. & Drew, H. D. Dual-gated bilayer graphene hot electron bolometer. *Nat Nanotechnol*. **7**(7), 472–478, 2012.

[106] Sassi, U., Parret, R., Nanot, S., Bruna, M., Borini, S., De Fazio, D., Zhao, Z., Lidorikis, E., Koppens, F. H. L., Ferrar, A.,C. & Colli, A. Graphene-based mid-infrared room-temperature pyroelectric bolometers with ultrahigh temperature coefficient of resistance. *Nat. Commun.* **80**, 1431 (2017).

[107] El Fatimy, A., Myers-Ward, R. L., Boyd, A. K., Daniels, K. M., Gaskill, D. K. & Barbara, P. Epitaxial graphene quantum dots for high-performance THz bolometers. *Nat. Nanotechnol.* **11**, 335–338 (2016).

[108] El Fatimy, A., Nath, A., Kong, B. D., Boyd, A. K., Myers-Ward, R. L., Daniels, K. M., Jadidi, M. M., Murphy, T. E., Gaskill, D. K. & Barbara, P. Ultra-broadband photodetectors based on epitaxial graphene quantum dots. *Nanophotonics* **7**(4), 735–740 (2018).

[109] Blaikie, A., Miller, D. & Alemán, B. J. A fast and sensitive room-temperature graphene nanomechanical bolometer. *Nat. Commun.* **10**:4726 (2019).

[110] Wang, Y., Wu, W. & Zhao, Z. Recent progress and remaining challenges of 2D material-based terahertz detectors. *Infrared Phys. Technol.* **102**, 103024 (2019).

[111] Viti, L., Hu, J., Coquillat, D., Politano, A., Knap, W. & Vitiello, M. S. Efficient terahertz detection in black-phosphorus nano-transistors with selective and controllable plasma-wave, bolometric and thermoelectric response. *Sci. Rep*. **6**:20474 (2016).

[112] Miao, W., Gao, H., Wang, Z., Zhang, W., Ren, Y., Zhou, K. M., Shi, S. C., Yu, C., He, Z. Z., Liu, Q. B. & Feng, Z. H. A graphene-based terahertz hot electron bolometer with Johnson noise readout. *J. Low Temp. Phys*. **193**(3–4), 387–392 (2018).

[113] Cai, X., Sushkov, A. B., Suess, R. J., Jadidi, M. M., Jenkins, G. S., Nyakiti, L. O., Myers-Ward, R. L., Li, S., Yan, J., Gaskill, D. K., Murphy, T. E., Drew, H. D. & Fuhrer, M. S. Sensitive room-temperature terahertz detection via the photothermoelectric effect in graphene. *Nat. Nanotechnol*. **9**(10) 814–819 (2014).

[114] Tong, J., Muthee, M., Chen, S. Y., Yngvesson, S. K. & Yan, J. Antenna enhanced graphene THz emitter and detector. *Nano Lett*. **15**(8), 5295–5301 (2015).

[115] Viti, L., Hu, J., Coquillat, D., Knap, W., Tredicucci, A., Politano, A. & Vitiello, M. S. Black phosphorus terahertz photodetectors. *Adv. Mater*. **27**, 5567–5572 (2015).

[116] Vicarelli, L., Vitiello, M. S., Coquillat, D., Lombardo, A., Ferrari, A. C., Knap, W., Polini, M., Pellegrini, V. & Tredicucci, A. Graphene field-effect transistors as roomtemperature terahertz detectors. *Nat. Mater.* **11**(10), 865–871 (2012).

[117] Zak, A., Andersson, M. A., Bauer, M., Matukas, J., Lisauskas, A., Roskos, H. G. & Stake, J. Antenna-integrated 0.6 THz FET direct detectors based on CVD graphene. *Nano Lett*. **14**(10), 5834–5838 (2014).

[118] Spirito, D., Coquillat, D., De Bonis, S. L., Lombardo, A., Bruna, M., Ferrari, A. C., Pellegrini, V., Tredicucci, A., Knap, W. & Vitiello, M. S. High performance bilayer graphene terahertz detectors. *Appl. Phys. Lett*. **104**(6), 061111 (2014).

[119] Qin, H., Sun, J., Liang, S., Li, X., Yang, X., He, Z., Yu, C. & Feng, Z. Room-temperature, low-impedance and high-sensitivity terahertz direct detector based on bilayer graphene field-effect transistor. *Carbon* **116**, 760–765 (2017).

[120] Bianco, F., Perenzoni, D., Convertino, D., De Bonis, S. L., Spirito, D., Perenzoni, M., Coletti, C., Vitiello, M. S. & Tredicucci, A. Terahertz detection by epitaxial-graphene field-effect-transistors on silicon carbide", *Appl. Phys. Lett*. **10**(13), 131104 (2015).

[121] Bandurin, D. A., Gayduchenko, I., Cao, Y., Moskotin, M., Principi, A., Grigorieva, I. V., Goltsman, G., Fedorov, G. & Svintsov, D. Dual origin of room temperature sub-terahertz photoresponse in graphene field effect transistors. *Appl. Phys. Lett*. **112**(14), 141101 (2018).

[122] Wang, L., Liu, C., Chen, X., Zhou, J., Hu, W., Wang, X., Li, J., Tang, W., Yu, A., Wang, S.- W. & Lu, W. Toward sensitive room-temperature broadband detection from infrared to terahertz with antenna-integrated black phosphorus photoconductor. *Adv. Funct. Mater*. **27**(7), 1604414 (2017).

[123] Liu, C., Wang, L., Chen, X., Zhou, J., Hu, W., Wang, X., Li, J., Huang, Z., Zhou, W., Tang, W., Xu, G., Wang, S.-W. & Lu, W. Room-temperature photoconduction assisted by hot-carriers in graphene for sub-terahertz detection", *Carbon* **130**, 233–240 (2018).

[124] Yadav, D., Tombet, S. B., Watanabe, T., Arnold, S., Ryzhii, V. & Otsuji, T. Terahertz wave generation and detection in double-graphene layered van der Waals heterostructures. *2D Mater*. **3**(4), 045009 (2016).

[125] Liu, C., Wang, L., Chen, X., Politano, A., Wei, D., Chen, G., Tang, W., Lu, W. & Tredicucci, A. Room-temperature high-gain long-wavelength photodetector via optical-electrical controlling of hot carriers in graphene. *Adv. Optical Mater.* 1800836 (2018).

[126] Currie, M. *Applications of graphene to photonics*. (NRL/MR/5650-14-9550, 2014).

[127] Long, M., Gao, A., Wang, P., Xia, H., Ott, C., Pan, C., Fu, Y., Liu, E., Chen, X., Lu, W., Nilges, T., Xu, J., Wang, X., Hu, W. & Miao, F. Room temperature high-detectivity mid-infrared photodetectors based on black arsenic phosphorus. *Sci. Adv.* **3**, e1700589 (2017).

[128] Vigo System Catalog. https://vigo.com.pl/wp-content/uploads/2017/06/VIGO-Catalogue.pdf

[129] Long, M., Wang, Y., Wang, P., Zhou, X., Xia, H., Luo, C., Huang, S., Zhang, G., Yan, H., Fan, Z., Wu, X., Chen, X., Lu, W. & Hu, W. Palladium diselenide long-wavelength infrared photodetector with high sensitivity and stability. *ACS Nano* **13**, 2511–2519 (2019).

[130] Ye, L., Wang, P., Luo, W., Gong, F., Liao, L., Liu, T., Tong, L., Zang, J., Xu, J. & Hu, W. Highly polarization sensitive infrared photodetector based on black phosphorus-on-WSe_2 photogate vertical heterostructure. *Nano Energy* **37**, 53–60 (2017)

[131] Amani, M., Regan, E., Bullock, J., Ahn, G. H. & Javey, A. Mid-wave infrared photoconductors based on black phosphorus-arsenic alloys. *ACS Nano* **11**, 11724–11731 (2017).

[132] HOT MCT Detectors, http://www.teledynejudson.com/

[133] Guyot-Sionnest, P., Ackerman, M. M. & Tang, X. Colloidal quantum dots for infrared detection beyond silicon. *J. Chem. Phys.* **151**, 060901 (2019).

[134] Konstantatos, G. & Sargent, E. H. Solution-processed quantum dot photodetectors. *Proc. IEEE* **97**, 1666–1683 (2009).

[135] Tennant, W. E., Lee, D., Zandian, M., Piquette, E. & Carmody, M. MBE HgCdTe technology: A very general solution to IR detection, descibrd by 'Rule 07', a very convenient heuristic. *J. Electron. Mater.* **37**, 1406–1410 (2008).

[136] Rogalski, A., Kopytko, M. and Martyniuk, P. Trends in performance limits of the HOT infrared photodetectors. *to be published*.

[137] Lee, D., Dreiske, P., Ellsworth, J., Cottier, R., Chen, A., Tallarico, S., Barr, H., Tcheou, H., Yulius, A., Carmody, M., Piquette, E., Zandian, M. & Dougla, S. Performance of MWIR and LWIR fully-depleted HgCdTe FPAs. (Extended Abstracts. The 2019 U.S. Workshop on the Physics and Chemistry of II-VI Materials, 189–190, 2019).

[138] Lee, A. W. M., Williams, B. S., Kumar, S., Hu, Q. & Reno, J. L. Real-time imaging using a 4.3-THz quantum cascade laser and a 320×240 microbolometer focal-plane array. *IEEE Photonics Technol. Lett.* **18**, 1415–1417 (2006).

[139] Oda, N. Uncooled bolometer-type terahertz focal-plane array and camera for real-time imaging. *C. R. Physique* **11**, 496–509 (2010).

[140] Bolduc, M., Terroux, M,. Tremblay, B., Marchese, L., Savard, E., Doucet, M., Oulachgar, H., Alain, C., Jerominek, H. & Bergeron, A. Noise-equivalent power characterization of an uncooled microbolometer-based THz imaging camera. *Proc. SPIE* **8023**, 80230C-1-10 (2011).

[141] Nguyen, D.- T., Simoens, F., Ouvrier-Buffet, J.- L., Meilhan, J. & Coutaz, J.- L. Broadband THz uncooled antenna-coupled microbolometer array—electromagnetic design, simulations and measurements. *IEEE Trans. Terahertz Sci. Technol.* **2,** 299–305 (2012).

[142] Goossens, S., Navickaite, G., Monasterio, C., Gupta, S., Piqueras, J. J., Pérez, R., Burwell, G., Nikitskiy, I., Lasanta, T., Galán, T., Puma, E., Centeno, A., Pesquera, A., Zurutuza, A., Konstantatos, G. & Koppens, F. Broadband image sensor array based on graphene–CMOS integration. *Nat. Photonics* **11**, 366–371 (2017).

[143] Phillips, J. Evaluation of the fundamental properties of quantum dot infrared detectors. *J. Appl. Phys.* **91**, 4590–4594 (2002).

[144] Piotrowski J. & Rogalski, A. Comment on "Temperature limits on infrared detectivities of $InAs/In_xGa_{1-x}Sb$ superlattices and bulk $Hg_{1-x}Cd_xTe$. *J. Appl. Phys.* **80**, 2542–2544 (1996).

[145] Yao, J., Shao, J., Wang, Y., Zhao, Z. & Yang, G. Ultra-broadband and high response of the Bi_2Te_3–Si heterojunction and its application as a photodetector at room temperature in harsh working environments. *Nanoscale* **7**, 12535–12541 (2015).

[146] Guo, Q., Pospischil, A., Bhuiyan, M., Jiang, H., Tian, H., Farmer, D., Deng, B., Li, C., Han, S.- J., Wang, H., Xia, Q., Ma, T.- P., Mueller, T. & Xia F. Black phosphorus mid-infrared photodetectors with high gain. *Nano Lett*. **16**, 4648–4655 (2016).

[147] Bullock, J., Amani, M., Cho, J., Chen, Y.- Z., Ahn, G. H., Adinolfi, V., Shrestha, V. R., Gao, Y., Crozier, K. B., Chueh Y.- L. & Javey, A. Polarization-resolved black phosphorus/molybdenum disulfide mid-wave infrared photodiodes with high detectivity at room temperature. *Nat. Photonics* **12**, 601–607 (2018).

[148] Tan, W. C., Huang, L., Ng, R. J., Wang, L., Hasan, D. M. N., Duffin, T. J., Kumar, K. S., Nijhuis, C. A., Lee, C. & Ang, K.-W. A black phosphorus carbide infrared phototransistor. *Adv. Mater*. **30**, 1705039 (2018).

[149] Rogalski, A., Martyniuk, P. & Kopytko, M. Type-II superlattice photodetectors versus HgCdTe photodiodes. *Prog. Quantum Electron*. **68**, 100228 (2019).

[150] Oyedele, A. D., Yang, S., Liang, L., Puretzky, A. A., Wang, K., Zhang, J., Yu, P., Pudasaini, P. R., Ghosh, A. W., Liu, Z., Rouleau, C. M., Sumpter, B. G., Chisholm, M. F., Zhou, W., Rack, P. D., Geohegan, D. B. & Xiao, K."$PdSe_2$: Pentagonal two-dimensional layers with high air stability for electronics", *J. Am. Chem. Soc*. **139**, 14090–14097 (2017).

[151] Mak, C. H., Lin, S., Rogée L. & Lau, S. P. Photoresponse of wafer-scale palladium diselenide films prepared by selenization method. J. *Phys. D: Appl. Phys.* **53** 065102(2020).

[152] Li, L., Wang, W., Chai, Y., Li, H., Tian, M. & Zhai, T. Few-layered PtS_2 phototransistor on h-BN with high gain. *Adv. Funct. Mater*. **27**, 1701011 (2017).

[153] Balandin, A. A. Low-frequency 1/f noise in graphene devices. *Nat. Nanotechnol*. **8**, 549–555 (2013).

[154] Viti, L., Hu, J., Coquillat, D,. Politano, A., Consejo, C., Knap, W. & Vitiello, M. S. Heterostructured hBN-BP-hBN nanodetectors at terahertz frequencies. *Adv. Mater*. **28**, 7390–7396 (2016).

[155] Viti, L., Politano, A. & Vitiello, M. S. Black phosphorus nanodevices at terahertz frequencies: Photodetectors and future challenges. *APL Materials* **5**, 035602 (2017).

[156] Hasan, M. Z. & Kane, C. L. Colloquium: Topological insulators. *Rev. Mod. Phys.* **82**, 3045–3067 (2010).

[157] Qi, X.- L. & Zhang, S.-C. Topological insulators and superconductors. *Rev. Mod. Phys.* **83**, 1057–1110 (2011)

[158] Ando, Y. Topological insulator materials. *J. Phys. Soc. Jpn*. **82**, 102001 (2013).

[159] Zhang, H., Liu, C.- X., Qi, X.- L., Dai, X., Fang, Z. & Zhang, S.- C. Topological insulators in Bi_2Se_3, Bi_2Te_3 and Sb_2Te_3 with a single Dirac cone on the surface. *Nat. Phys*. **5**, 438–442 (2009).

[160] Fu, L., Kane, C. L. & Mele, E. J. Topological insulators in three dimensions. *Phys. Rev. Lett*. **98**, 106803 (2007).

[161] Di Pietro, P., Ortolani, M., Limaj, O., Di Gaspare, A., Giliberti, V., Giorgianni, F., Brahlek, M., Bansal, N., Koirala, N., Oh, S., Calvani, P. & Lupi, S. Observation of Dirac plasmons in a topological insulator. *Nat. Nanotechnol*. **8**, 556–560 (2013).

[162] Tian, W., Yu, W., Shi, J. & Wang, Y. The property, preparation and application of topological insulators: A review. *Materials* **10**, 814 (2017).

[163] Viti, L., Coquillat, D., Politano, A., Kokh, K. A., Aliev, Z. S., Babanly, M. B., Tereshchenko, O. E., Knap, W., Chulkov, E. V. & Vitiello, M. S. Plasma-wave terahertz detection mediated by topological insulators surface states. *Nano Lett*. **16**, 80–87 (2016).

[164] Tang, W., Politano, A., Guo, C., Guo, W., Liu, C., Wang, L., Chen, X. & Lu, W. Ultrasensitive room-temperature terahertz direct detection based on a bismuth selenide topological insulator. *Adv. Funct. Mater.* **28**, 1801786 (2018).

[165] Kuriakose, S., Ahmed, T., Balendhran, S., Bansal, V., Sriram, S., Bhaskaran, M. & Walia, S. Black phosphorus: ambient degradation and strategies for protection. *2D Mater.* 5(3), 032001, 1–10 (2018).

[166] Chen, D.- R., Hofmann, M., Yao, H.- M., Chiu, S.- K., Chen, S.- H., Luo, Y.- R., Hsu, C.- C. & Hsieh, Y.- P. Lateral two-dimensional material heterojunction photodetectors with ultrahigh speed and detectivity. *ACS Appl. Mater. Interfaces* **11**, 6384–6388 (2019).

[167] Wang, M. & Yang E.-H. THz applications of 2D materials: Graphene and beyond. *Nano-Struct. Nano-Objects* **15**, 107–113 (2018).

[168] Wang, P., Liu, S., Luo, W., Fang, H., Gong, F., Guo, N., Chen, Z.-G., Zou, J., Huang, Y., Zhou, X., Wang, J., Chen, X., Lu, W., Xiu, F. & Hu, W. Arrayed van der Waals broadband detectors for dual-band detection. *Adv. Mater*. **29**, 1604439 (2017).

[169] *Seeing Photons: Progress and Limits of Visible and Infared Sensor Arrays*, Committee on Developments in Detector Technologies; National Research Council, 2010, http://www.nap.edu/catalog/12896.html

[170] Rogalski, A. History of infrared detectors. *Opto-Electron*. *Rev*. **20**, 279–308 (2012).

[171] Rogalski, A. Progress in focal plane array technologies. *Prog*. *Quantum Electron*. **36**, 342–473 (2012).